Freestanding 2D Materials and their Applications

From Lab to Fab

Cartamil Bueno, Santiago

DOI
10.4233/uuid:44e23602-611f-4d43-81b4-f468c80749e0

Publication date
2017

Document Version
Final published version

Citation (APA)
Cartamil Bueno, S. (2017). *Freestanding 2D Materials and their Applications: From Lab to Fab*. [Dissertation (TU Delft), Delft University of Technology]. https://doi.org/10.4233/uuid:44e23602-611f-4d43-81b4-f468c80749e0

Important note
To cite this publication, please use the final published version (if applicable).
Please check the document version above.

FREESTANDING 2D MATERIALS AND THEIR APPLICATIONS

FROM LAB TO FAB

FREESTANDING 2D MATERIALS AND THEIR APPLICATIONS

FROM LAB TO FAB

Proefschrift

ter verkrijging van de graad van doctor
aan de Technische Universiteit Delft,
op gezag van de Rector Magnificus prof. ir. K.C.A.M. Luyben,
voorzitter van het College voor Promoties,
in het openbaar te verdedigen op maandag 18 december 2017 om 15:00 uur

door

Santiago José CARTAMIL BUENO

Master of Science in Nanotechnology and Materials Science
Universitat Autònoma de Barcelona (UAB), Spain
geboren te Melilla, Spanje

This dissertation has been approved by the promotors

Prof. dr. P. G. Steeneken and
Prof. dr. ir. H. S. J. van der Zant

Composition of the doctoral committee:

Rector Magnificus,	voorzitter
Prof. dr. P. G. Steeneken,	Technische Universiteit Delft
Prof. dr. ir. H. S. J. van der Zant,	Technische Universiteit Delft
Dr. S. Houri,	NTT Basic Research Laboratories
Independent members:	
Prof. dr.-Ing. M. C. Lemme,	RWTH Aachen University
Prof. dr. S. Hofmann,	University of Cambridge
Prof. dr. J. S. Bunch,	Boston University
Prof. dr. G. C. A. M. Janssen,	Technische Universiteit Delft
Prof. dr. Y. M. Blanter,	Technische Universiteit Delft, reserve

Keywords: Graphene, 2D materials, membranes, mechanical resonators, mechanical pixels, atomic force microscopy (AFM), laser interferometry, colorimetry, sensing applications, Graphene Interferometric Modulator Display (GIMOD)

Printed by: Gildeprint - Enschede

Front & Back: Graphene mechanical pixels showing Newton's rings (front) upon illumination originated from the torch of Prometheus (*Prometheus Bringing Fire To Mankind*, by Heinrich von Fuger *circa* 1817, back).

Casimir PhD series, Delft-Leiden 2017-44

ISBN 978-90-8593-328-1

An electronic version of this dissertation is available at
`http://repository.tudelft.nl/`.

To the visionaries and dream figthers of the past
who where labeled as crazy and burned
unfairly without acknowledgement.
Your sacrifice is my scale armor.

To those who care about people, trust in humanity and fight for a better world.

Santiago

CONTENTS

SUMMARY

This thesis synthesizes the results of my work, in cooperation with other local and international researchers, on the understanding of mechanical devices made out of freestanding graphene and other 2D materials, and some of the potential applications of these nanomembranes. Its structure follows a dual story with two interspersed themes. On one hand, it is a chronological guide of techniques that were tested or developed, and at the same time it is an exploration of different materials for particular applications. Therefore, the thesis is divided in application parts comprising chapters discussing techniques and findings related to the given material.

After a historical introduction on materials, *Chapter 1* uses the mineral called *graphite* to guide us through the annals of scientific progress to arrive to the definition of nanotechnology and the understanding of what layered materials are. From there, a leap to present times transports us to the current understanding of *graphene* and other *2D materials*, followed by their use in micro-/nano-electromechanical systems (M/NEMS).

Application 1: $TaSe_2$ for write-once-read-many (WORM) memory devices contains *Chapter 2*. In this chapter, we introduce the laser interferometry setup to study the dependence of the mechanical resonance frequency on the thickness of tantalum diselenide ($TaSe_2$) drumheads. We observe a continuous transition from plate to membrane behavior when reducing the thickness from 100 nm to 6 nm, and we prove the large effect of stress on the resonance frequency of 2D materials by laser-oxidation of the thin membranes. This selective laser-oxidation is comparable to the laser-recording of CD-R and DVD-R optical disks, and therefore each of these $TaSe_2$ NEMS could be a bit of a write-once-read-many (WORM) memory unit.

Application 2: CVD graphene and h-BN for optomechanic sensing spins around the use of NEMS membranes made out of two prominent materials made by chemical vapor deposition: double-layer graphene and single-layer hexagonal boron nitride.

In *Chapter 3* we perform a small statistical analysis on the fundamental resonance frequency of CVD DLG drumheads to find its theoretical dependence with the device diameter by means of laser interferometry. Variations of the mechanical resonance are attributed to differences in tension of the membranes, which are compared to values obtained by nanoindentation with an atomic force microscope. The cleanliness of the drums is discussed together with the pressure-induced destruction of the larger devices. Furthermore, the invasive nature of the laser technique due to the heat impact on the measurements is exposed by providing evidence for softening or tensioning of the membranes and their photothermal self-oscillation at higher laser powers. This allow us to present a new theory that explains the heating effects from the laser on the resonance frequency and quality factor of these membranes by a model based on thermally-induced variation of the sidewall length.

Chapter 4 explores the use of single-layer h-BN. We fabricate drums of 5 μm in diameter, extract their mechanical properties with the laser and atomic force microscope techniques, and study their behavior when cooling them to cryogenic temperatures (3 K). The process is repeated after a series of cleaning steps to demonstrate a route for reducing the contamination in this type of fragile structures while exploiting the inorganic nature of this material. We also propose a model that describes an adhesion-mediated influence of temperature on the mechanics of certain 2D materials.

Application 3: CVD graphene for pressure sensing describes the colorimetry technique and the uses we have given to the color-changing of double-layer graphene drumheads.

In *Chapter 5*, we analyze several samples with single- and double-layer graphene drumheads of different diameters and cavity depths in a very large scale fashion. With the colorimetry technique, we obtained the statistical probabilities of a given device geometry to survive a pressure difference of 1 atm. We found that the device yield follows a trend ruled by a scaling parameter, which indicates that the main failure mode is due to contact between membrane and cavity bottom, and that the survival probability improves considerably when using two instead of one graphene layers. Moreover, we extracted the adhesion energy of the double-layer graphene by studying membranes stuck to the bottom of their cavities.

Chapter 6 explains how to use the technique to extract the pressure-induced deflection of the membranes as a function of time, and shows how this can be used to measure their gas permeability. The observation of Newton's rings enabled their exploitation for exploring the large deflection regime of these membranes where the device stiffness is dominated by the Young's modulus. A study of the pressure decay in the small deflection regime allowed us to measure the permeance of a membrane, and we found that gas molecules escape from these devices faster than when they have to enter sealed cavities under vacuum.

Killer application: CVD graphene for interferometry modulation displays (IMOD) introduces the main innovation in this dissertation: Graphene IMODs. *Chapter 7* combines the colorimetry technique with electrostatical actuation to study the dynamical movement of double-layer graphene membranes stroboscopically. The tension of the membranes was extracted non-invasively while vibrating them at frequencies up to 2 kHz without observing mechanical delays nor gas damping, hence proving the suitability of this type of mechanical pixels for applications requiring high refresh rates. The demonstration of GIMOD technology in the Mobile World Congress 2017 in Barcelona served as a test to validate the usefulness of such kind of displays, which was well-received by industry.

Future Applications (*Chapter 8*) concludes the thesis with some promising uses of 2D materials in the coming years. A continuation of the study on large populations of graphene NEMS will give predictions of the actual applications of those devices for pressure and gas sensing with less speculation. Statistics on the permeability of CVD graphene with different layers could reveal the feasibility of hermetic sensors or molecular sieves. Moreover, their optical properties should be improved to make the GIMOD technology competitive. These enhanced optical properties could also be used in other technologies that require weightless and robust materials with high optical reflectivity such as light sails and other space applications.

SAMENVATTING

Dit proefschrift vat de resultaten van mijn werk, in samenwerking met andere lokale en internationale onderzoekers samen, over het begrijpen van mechanische apparaten uit vrijstaande grafeen en andere 2D-materialen, en enkele mogelijke toepassingen van deze nanomembranen. De structuur volgt een dubbel verhaal met twee afgewisselde thema's. Enerzijds is het een chronologische gids van technieken die getest of ontwikkeld zijn, en tegelijkertijd is het een verkenning van verschillende materialen voor specifieke applicaties. Daarom is het proefschrift opgedeeld op basis van toepassingen, welke hoofdstukken bevatten over technieken en over bevindingen die verband houden met het gegeven materiaal.

Na een historische introductie over materialen, gebruikt *Chapter 1* het mineraal genaamd *graphite* om ons door de annalen van wetenschappelijke vooruitgang te begeleiden, om te komen tot de definitie van nanotechnologie en het begrip van wat gelaagde materialen zijn. Van daaruit vervoert een sprong naar de huidige tijd ons naar het huidige begrip van *grafeen* en andere *2D materialen*, gevolgd door hun gebruik in micro-/nanoelektromechanische systemen (M/NEMS).

Application 1: $TaSe_2$ for write-once-read-many (WORM) memory devices bevat *Chapter 2*. In dit hoofdstuk introduceren we de laserinterferometrie opstelling, om de afhankelijkheid van de mechanische resonantie frequentie op de dikte van tantaaldiselenide ($TaSe_2$) trommelvellen te bestuderen. We zien een continue overgang van plaat- naar membraangedrag bij het verminderen van de dikte van 100 nm tot 6 nm, en we bewijzen het grote effect van stress op de resonantie frequentie van 2D materialen door laser-oxidatie van de dunne membranen. Deze selectieve laseroxidatie is vergelijkbaar met de laseropname van CD-R en DVD-R optische schijven en daarom zou elk van deze $TaSE_2$ NEMS een bit van een WORM-geheugeneenheid (write-once-read-many, eens-schrijven-veel-uitlezen) kunnen zijn.

Application 2: CVD graphene and h-BN for optomechanic sensing draait om het gebruik van NEMS membranen gemaakt van twee prominente materialen, gemaakt door chemische dampafzetting: dubbellaags grafeen en enkellaags hexagonaal boornitride.

In *Chapter 3* voeren we een kleine statistische analyse uit op de fundamentele resonantiefrequentie van CVD DLG trommelvellen om zijn theoretische afhankelijkheid te vinden met de diameter van het apparaat door middel van laserinterferometrie. Variaties van de mechanische resonantie worden toegeschreven aan het verschil in spanning van de membranen, die worden vergeleken met de waarden die worden verkregen door nanoindentaties met een atoomkrachtmicroscoop. De zuiverheid van de drums wordt besproken samen met de drukgeïnduceerde vernietiging van de grotere apparaten. Bovendien wordt de invasieve aard van de lasertechniek als gevolg van het warmte-effect op de metingen blootgelegd door bewijs te leveren van het ontspannen en aanspannen van de membranen en hun fotothermische zelfoscillatie bij hogere laservermogens. Hierdoor kunnen we een nieuwe theorie

presenteren die de verwarmingseffecten van de laser op de resonantiefrequentie en kwaliteitsfactor van deze membranen verklaart als functie van thermisch geïnduceerde variatie van de zijwandlengte.

Chapter 4 verkent het gebruik van enkelvoudig h-BN. We vervaardigen trommels van 5 μm in diameter, ontraadselen hun mechanische eigenschappen met de laser- en atoomkrachtmicroscooptechnieken en bestuderen hun gedrag wanneer ze afkoelen op cryogene temperaturen (3 K). Het proces wordt herhaald na een reeks reinigingsstappen om een route te demonstreren die de vervuiling in dit soort fragiele structuren te vermindert, waarbij de anorganische aard van dit materiaal wordt benut. Wij stellen ook een model voor waarin de invloed van temperatuur op de mechanica van bepaalde 2D-materialen op basis van hechting wordt beschreven.

Application 3: CVD graphene for pressure sensing beschrijft de colorimetrietechniek en de toepassingen die we hebben gegeven aan de kleurveranderingen van dubbellaags grafeen trommelvellen.

In *Chapter 5* analyseren we verscheidene monsters met enkel- en dubbellaagse grafeentrommelvellen met verschillende diameters en holtedieptes op zeer grote schaal. Met de colorimetrietechniek hebben we de statistische waarschijnlijkheden verkregen dat een gegeven vorm van het apparaat een drukverschil van 1 atm overleeft. We hebben geconstateerd dat de opbrengst van het aantal apparaten een trend volgt die door een schaalparameter wordt bepaald en dat de overlevingswaarschijnlijkheid aanzienlijk verbetert bij gebruik van twee in plaats van één grafeenlaag. Bovendien hebben we de hechtingsenergie van de dubbellaagsgrafeen ontraadseld door membranen die contact maken met de bodem van hun holtes te bestuderen aan de onderkant van hun holtes te bestuderen.

Chapter 6 legt uit hoe de techniek gebruikt kan worden om de drukgeïnduceerde buiging van de membranen als een functie van de tijd te bepalen en dus hun gasdoorlaatbaarheid te meten. De observatie van de ringen van Newton maakte het mogelijk om het gebied van grote buiging van deze membranen die door de Young's modulus wordt gedomineerd, te onderzoeken. Een blik op het drukverval in het gebied met een kleine buiging liet ons de doorlatendheid van een membraan meten en we vonden dat gasmoleculen sneller uit deze apparaten ontsnapten dan ze gesloten vacuüm holtes in gaan.

Killer application: CVD graphene for interferometry modulation displays (IMOD) introduceert de hoofdinnovatie in dit proefschrift: Grafeen IMODs. *Chapter 7* combineert de colorimetrie techniek met elektrostatische actuatie om de dynamische beweging van dubbellaagse grafeenmembranen stroboscopisch te bestuderen. De spanning van de membranen werd niet-invasief bepaald, terwijl we ze met frequenties tot 2 kHz lieten trillen zonder mechanische vertragingen of gasdemping waar te nemen, waardoor de geschiktheid van dit type mechanische pixels voor toepassingen die hoge verversingssnelheden vereisen, bewezen is. De demonstratie van GIMOD-technologie in het Mobile World Congress 2017 in Barcelona diende als een test om het nut van dergelijke displays te valideren, waarbij het een succesvol onthaal in de industrie heeft gehad.

Future Applications (*Chapter 8*) sluit het proefschrift af met een aantal veelbelovende toepassingen van 2D-materialen voor de komende jaren. Een voortzetting van de studie

over grote populaties van grafenen NEMS zal een niet-speculatieve voorspelling geven van de werkelijke toepassingen van dergelijke apparaten voor druk- en gaswaarneming. Statistieken over de doorlaatbaarheid van CVD-grafeen met verschillende lagen kunnen de haalbaarheid van hermetische sensoren of moleculaire zeven onthullen. Bovendien moeten hun optische eigenschappen worden verbeterd om de GIMOD-technologie competitief te maken. Dit kan ook worden gebruikt in andere technologieën die gewichtloze en robuuste materialen vereisen met hoge optische reflectiviteit, zoals lichtzeilen en andere ruimtevaart toepassingen.

PREFACE

HUMANITY AND TECHNOLOGY

WE, humans, are characterized by our stubborn survival skills –that allowed us to evolve to what we are now– and overcoming the limits of our abilities with the help of faith: either by believing in institutions, leaders or abstract entities that somehow tell you how to proceed (top-down approach); by believing in egoistic dreams or ambitions (individual approach); or by believing in common values shared in the group or society one belongs to (bottom-up approach).

Most of major endeavors, especially the geographical ones, were driven by the pursuit of finding more or better resources that could help the individual or its group to survive or compete with rival individuals or groups. Examples of this could be:

- the discovery of the Americas when looking for alternative routes to trade spices in the 1500s;
- the sperm whale hunting to provide waxy liquid for lighting the cities in the 1800s;
- the wars to guarantee gas and oil to power machines and factories that started in 1900 and prevail to nowadays;
- and even the new era of space colonization to obtain materials from the Moon's crust that would enable self-sustained settlements in our satellite, among others.

They all have in common –beside the massacre of humans and other animals– the development of a new technology, which typically replaces an established one (also causing social revolts due to the destruction of related jobs).

However, technology and resource pursuit are not sufficient to make humans to stand up, take risks and discover new things. It is the irrational curiosity meeting our imagination which makes us feel attracted to the unknown and inhibits our logical brain that prevents us from losing time, making a mistake or simply dying. A great example is the control of *fire*. Surely our ancestors grew scared of fire and avoiding it had some 'logical' explanation to their uneducated minds, similarly to what a baby would experience nowadays unless he is taught on how to handle it. But at some point in time, someone had the curiosity of grabbing a tree branch and controlling the power of fire. Possibly it also happened by accident, and by a sudden need to survive under an extreme situation that suppressed the fear of fire established by the group. But they had a will, a desire to live, fire in their eyes and heart.

Where would we be if fear of failure/death and dogmatic 'logic' could not be fought with the irrational curiosity of the human being? Animals have also curiosity, but they lack of means to developing complex tools and transferring and storing the individual knowledge for the present and future societies (collective learning). And yet, they survive, if we humans –the other animals with better knowledge– want.

Where would we be if those ancestors had managed to keep the fire or its technological applications for themselves? Progress might be better in our modern times, yet we live in a society where materialism and individualism are promoted by elites, supported by mass media, normalized through global networks, and embraced by average people. A vast majority of 'developed world' humans that, in their mistakenly belief of belonging to a safe and secured 'medium class', have been dispossessed of the only thing that makes them different from the animals whose meat they can buy in the supermarket: having a collective will.

An ardent will to positively contribute to society, to change it or influence it at least, even if that society initially overlooks, ignores, depreciates or is afraid of our social demands and its consequences to the world timings and long term schedules. Humans are useful to the world system as we are still its workforce, and we accept this cheap deal as exchange of being entertained provided we can have food to survive. In the meantime, elites work on making their businesses more profitable by increasing the efficiency of people's jobs, which it is well known to go through involving less humans in the manufacturing processes and substituting them with machines.

And Science is not an exemption. With the introduction of marketing strategies in the 1930s, knowledge started to become compromised. Despite the strong resistance of the scientific community to this business of selling empty words and partial truths that only confuse and manipulate the population and prevents a real progress, it succumbed to the modern fashion of treating knowledge as a yet another product to be sold. Possibly machines using artificial intelligence will sooner than later match our exploring and researching skills and even take over this unique advantage that humans hold in the world we know[1]. But once curiosity is compromised, they will not need to share their knowledge with us and we will be sentenced to race ostracism like the rest of animals. At the end, this is what humans have done to other beings, and these machines are created after human models and to follow human patterns... and this is only accounting for the human vision of the situation (which may be incomplete if machines develop a different machine vision) and for a human survival to the global warming.

New scientists should become aware at least, and maybe comply temporally if afraid of *truly* compromising their individual survival, but never give up for some coins or fame. Humanity needs new and independent thinkers, call it scientists, philosophers, writers or preachers. Real leaders that actively look for routes to change this destructive path and free us from this blinding jail that will surely terminate us as an intellectual race and be degraded to consumable animals. Normal people that overcome again the fear of fire.

[1] *Postmodern Prometheus*, by H. Hirsh in Science 357, 6350, 460-460 (2017)

ON THE COVER

The front cover displays the artistic impression of a graphene pixel showing Newton's rings. As discussed in Chapter 7, this occurs when the device is illuminated with white light under certain interference conditions. This pixel could be that of a graphene interferometric modulation display (GIMOD), a reflective-type screen that outperforms any other display technology when the environment is well illuminated, but requires of an external light source in darkness. For the case in this cover, I have chosen the most common and popular type of light source that every human desires in darkness during power cuts: fire. And who better to carry the fire than Titan Prometheus with the original Olympic flame?

The back cover illustrates part of the masterpiece entitled *Prometheus Bringing Fire To Mankind* by Heinrich von Fuger (*circa* 1817). The painting shows Prometheus running away from the gods in Mount Olympus after grabbing the original fire with a torch. Previously, the gods had feared the potential of humans and decided to steal their fire to keep them blind in darkness. Prometheus, in a titanic act of justice and with an altruistic and kindhearted attitude, decided to risk his neutrality to return the fire to humankind.

Titan Prometheus took the fire from the gods after they attacked humankind in a totalitarian behavior for their own interest of retaining power on themselves and to prevent the power distribution by sharing it with common humans. As a result, humans could continue to progress although Prometheus was punished by the gods. He was isolated from other beings and chained to a rock, and the gods made an eagle to eat his liver daily during day time (he healed overnight). This punishment lasted for a millennium, until semi-human Hercules killed the eagle and freed Prometheus from his fate.

The importance of fire in human development is unquestionable. Not only it protected us from the wildness and gave us warmth in the past, but helped us to forge weapons and tools that boosted technology and progress. Before the electric lighting, it was used to illuminate our houses and cities, and today enlightens us from a candle in romantic moments.

Many institutions and companies carry Prometheus' flame in their logos or corporate designs and, in a similar fashion to the Olympic committee, some people belonging to them seem to have forgotten what that fire stands for. Nowadays, one can light up his/her own torch since Mount Olympus does not belong to gods, but it is rather under human jurisdiction. And, as everyone knows, one should not play with fire because it can spread quickly in forests when too many trees are dead.

In a broader and more metaphorical view, we could see a compromised Science in need of a fire that returns the warmth and light that it used to provide. The Dark Enlightening episode of Science we are witnessing is no more than a result of the usual reactionary movement of some "leaders" that believe in gods (or believe themselves to be gods) and their opportunistic, casting henchmen. They are easy to spot as they favor individualism to promote the competition in a no-guaranteed-rights scheme, but they get angry if the same rules are applied back against them. Also, dark-enlighteners ignore problems as long as these do not concern their own power. They tend to evaluate everything after a simple "What do I win?" test, and they ask "What do you want/win?" because they do not understand common causes and altruist behavior. This type of misunderstandings brings them out of their

comfort zone, which they handle by displaying their wrath with authoritarian speech, acts and decisions.

On the bright side, nanotechnology is possibly bringing a kind of romantic approach to Science again, where the multidisciplinary and open-minded dialog is a must to proceed (and succeed). Similar to the birth of classical Romanticism (Age of Reflection) in the 1800s (originated as an alternative to the progressive Enlightenment movement), nanotechnology –and the 2D materials field in particular– is developing as a comprehensive branch of Science that substitutes the previous branching of scientific specializations. For instance, it has embedded the romantic anti-reductionism that seeks the value of the whole against the individual contribution of the parts. As a 2D example, dark-enlightening researchers cannot understand that graphene MEMS require a multiphysics approach since a complete Comsol simulation would still miss its atomic reality and hence the effect of ripples and wrinkles on its mechanical, electrical, optical and thermal properties. On the contrary, a neo-romantic researcher would use his/her creativity, genius, intuition and experience, which requires an undisturbed, unforced contemplation and the understanding of oneself in the context of the measurement, to propose an out-of-the-box idea that flows freely in search of an empirical proof.

I wonder if we could include this scientific mindset as part of a new movement called *Enlightening Romanticism* or simply *Neoromanticism*. In contrast to dark-enlightenment science, where nature has been objectified and knowledge is commercialized, Neoromantic Science refuses individualism, fake collaborations and for-profit research, and bets on trust-based cooperation of humans. I wish that this self-reflection finds a strong reaction in other researchers that may want to light up their torches with mine as I must proceed into the Age of Imagination.

Santiago José Cartamil Bueno
Bremen, 5 November 2017

1

INTRODUCTION

When the prison doors are opened, the real dragon will fly out.

Hồ Chí Minh

I have fire in the heart.

Santiago, Delft 2013

Parts of this chapter have been published in a) npj 2D Materials and Applications **1**, 16 (2017) by S.J. Cartamil-Bueno, M. Cavalieri, R. Hwang, S. Houri, S. Hofmann, and H.S.J. van der Zant; b) Nano Letters **16**, 6792–6796 (2016) by S.J. Cartamil-Bueno, P.G. Steeneken, A. Centeno, A. Zurutuza, H.S.J. van der Zant, and S. Houri; and c) Nanoscale **9**, 7559-7564 (2017) by S.J. Cartamil-Bueno, A. Centeno, A. Zurutuza, P.G. Steeneken, H.S.J. van der Zant, and S. Houri.

1.1. MATERIALS LEAD TECHNOLOGY

Solid is one of the fundamental states of matter. Solid materials are usually made out of atoms bonded to each other and arranged with a certain order (crystallinity). The physical properties of a solid, including mechanical and electrical ones, depend largely on the chemistry of the elements that compose it, although it is hard to understand them by only looking at the periodic table (Figure 1.1).

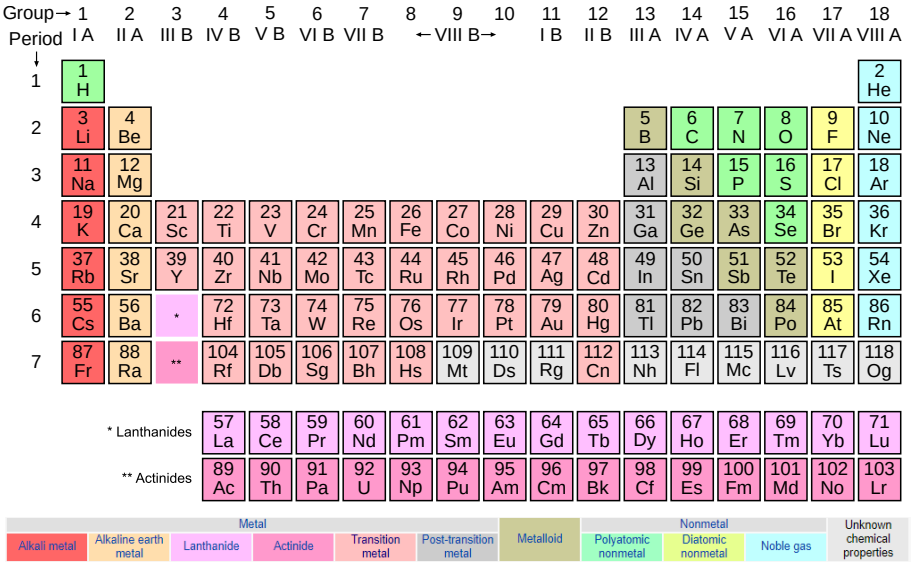

Figure 1.1: Periodic table of elements. Adapted from Wikimedia Commons [1].

A quick Wikipedia research [2, 3, 4] reveals this fact: humans largely progressed when a material was controlled and applied[1] to make artifacts (*arte factum* in Latin, meaning "thing made by skill"). An artifact or device is an object made or given shape by a human or machine, such as a tool or a work of art, and very often its increased usefulness when compared to the established counterparts gave technological advantage to the civilization that dominated it. Nowadays, we divide the Pre-history into three periods: the Stone Age (until 8700/2000 bc), characterized by the use of stone and ceramics to fabricate tools or weapons; the Bronze Age (3300 bc-600 bc), when the forging and later smelting[2] of copper and alloying with tin and other metals was invented; and the Iron/Steel Age (1200 bc-1 bc/600 ac), known for the domination of iron and its carbon-mixed alloy, both produced and traded alongside glass.

[1] *applicare* in latin, meaning "attach to, join, connect;" figuratively, "devote (oneself) to, give attention," from ad- "to" + plicare "fold". http://www.dictionary.com/browse/apply

[2] Smelting consisted on the production of a base metal from its ore by oxidation and melting of the material with fire.

The Classical Antiquity (1st to 5th century) witnessed the alchemical beginnings of chemistry, the tensioning of materials in mechanisms to construct Seven Wonders, and the invention of watermills and windwheels for unattended propulsion and movement beyond human forces. The great advances in technology and engineering during this period were followed by the Middle Ages or Medieval Period (5th century-14th century), although that time is remembered as Dark Age due to the knowledge stigmatization by dogmas that slowed its spread and hence the technological progress. A funny fact is that a metal smith, Johannes G. zur Laden zum Gutenberg, invented the printing press in the 15th century, and that same type of mechanical movable machine helped to spread the knowledge in metallurgy with two important and systematic books: *De La Pirotechnia* ("On the Techniques with Fire", by Vannoccio Biringuccio in 1540) and *De Re Metallica* ("On the Nature of Metals", by Georgius Agricola in 1556).

The Printing Revolution opened the Modern Era of human history with many philosophical movements and cultural changes being interspersed with the Scientific Revolution and the Industrial Revolutions. By mid-20th century we had developed the machine manufacture and communication systems, constructed railroad networks, optimized steam-powered machines, invented the electrical power and its use in factories for line production of tools and other machines, and learned to use fossil fuels. The first mechanical computers were invented in the 19th century to overcome the mathematical calculation ability of humans, and the need of faster and more powerful machines resulted in the creation of electrical computers. They were the cause of the Digital Revolution that started our current Age of Information and, one more time, materials led technology being semiconductors (and suitable insulators) the key players in electronics as transistor materials [5]: germanium (1947), silicon (1954), gallium arsenide (1966), silicon-germanium alloy (1989), and silicon carbide (1997).

In the search of more efficient electronics, we have managed to reduce the size of materials beyond what a microscope can see. When the dimension of a material falls into the realm of nanotechnology (<100 nm) we say that it "loses" that dimension as the properties differ from its bulk counterpart. But can we bring solid matter to its ultimate atomic limit and still call it a solid?

1.2. LAYERED MATERIALS

Layered materials have been used for half a millennium due to their unique properties, although no one really knew why they were so special until beginnings of the 20th century.

In the 1500s, a large deposit of graphite was found in Borrowdale parish, (Cumbria, England) by German immigrants. At the beginning, this layered material was known as black lead, molybdaena or plumbago confusingly alongside other ores (galena and molybdenite) [6]. The early uses of graphite were rural, to mark sheep [7, 8], although soon the Crown realized the great refractory material graphite was, thus becoming a key resource for molding lead or iron at high temperatures to make rounder and more aerodynamic cannon balls [9]. Despite of the royal appropriation under military pretexts, the application of graphite for drawing spread quickly all over the world, and by the next century artists were

making plumbago drawings with sticks cut from natural graphite wrapped in sheepskin (see Figure 1.2). In 1560, an Italian couple came up with a way of enclosing a thin bar of graphite in between two carven wooden sticks, and Swiss Conrad Gessner first reported it in 1656. This invention is considered the beginning of modern carpentry pencils [7].

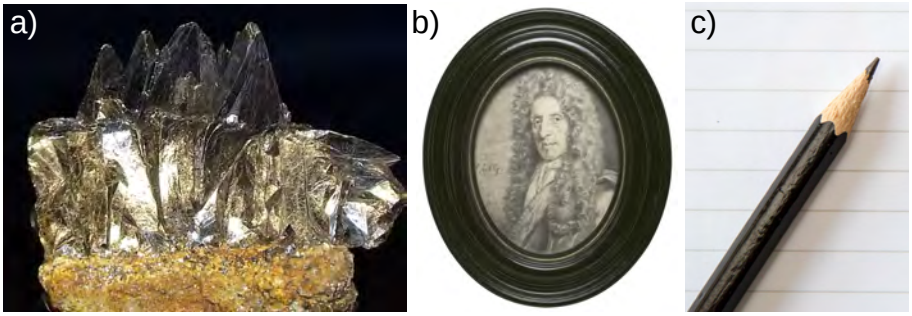

Figure 1.2: Different forms of graphite in nature: a) graphite ore, b) *John Locke* plumbago drawing of the namesake philosopher by Sylvester Brounower in *circa* 1685 (©National Portrait Gallery, London), and c) pencil with a graphite load. a) adapted from Wikimedia Commons [10]; c) adapted from "Paper And A Pencil" [11].

The scientific revolution started around that time with the publication of Nicolaus Copernicus' work *De Revolutionibus Orbium Coelestium* ("On the Revolutions of the Heavenly Spheres", 1543). By the time philosopher John Locke was leading the Age of Enlightenment (1620s-1789), scientists were developing the empiricism and scientific method, signatures of modern Science [12]. The observation of natural phenomena only or mainly through our senses (empirical evidence) started to substitute the dogmatic reasoning/thinking of the Scholasticism based on the Aristotelian tradition, and the test studies that created experience (*εμπειρία* -empeiria- in Greek, *experientia* in Latin) became the target of scientists with the consequent knowledge transfer to the scientific community.

One of the first experiments on graphite was done by chemist Carl W. Scheele in 1778. He analyzed the composition of graphite and those "similar" minerals and concluded that they were actually different materials despite their shared shiny blackness: graphite (carbon, C), galena (lead sulfite, PbS) and molybdenite (molybdnenum disulfide, MoS_2) [13]. Few years later, geologist Abraham G. Werner gave its name to graphite, formed with the Greek word for writing or drawing "graphein" plus the mineral suffixe "-ite" [14]. In 1859 chemist Benjamin C. Brodie distinguished between layered graphite and amorphous carbon [15, 16], and its structure was studied in 1910s alongside other materials by diffraction [17, 18], being ultimately described by John D. Bernal, Odd Hassel and Heinrich Mack in 1924 [19, 20].

Amorphous carbon, diamonds and graphite are made out of carbon, although they have different properties and only the latter is purely layered as shown in Figure 1.3a-c. They are carbon allotropes (together with more recent fullerenes and carbon nanotubes), that is, structures of carbon atoms arranged in different forms. Carbon is the element with atomic number 6 in the periodic table (hence with an electronic configuration of $1s^2 2s^2 2p^2$), and

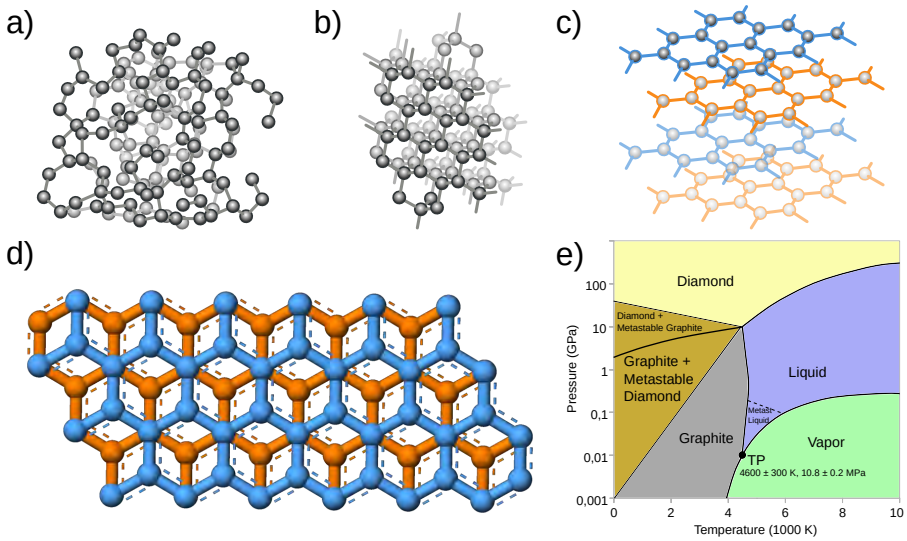

Figure 1.3: Structure of carbon allotropes: a) amorphous carbon, b) cubic carbon (diamond), and c) hexagonal carbon (graphite). d) Top view of graphite layers forming an AB or Bernal stack. e) Phase diagram of carbon. Adapted from Wikimedia Commons [21, 22, 23].

it has an atomic mass number of 12: ${}^{12}_{6}\mathrm{C}$. When two carbon atoms interact, they can share some of their electrons in different ways: sp_2 and sp_3 hybridizations are the most common ones. The final configuration depends on the temperature and pressure at which the material is set, as it can be extracted from the phase diagram of carbon (Figure 1.3e).

In an sp_2 bonding configuration, pairs of electrons are shared between the atoms forming σ (sp_2: one s-orbital and two p-orbitals, p_x and p_y) and π (one p-orbital, p_z) covalent bonds, and the carbon atoms are arranged in a planar hexagonal crystal structure we call *graphene* (h-C) (see Figure 1.4). The covalent bonds between carbon atoms in graphene are very strong, and the (weaker) π bonds prevent other atoms binding to the planar structure, forcing them to form another *layer* by themselves that "sits" on top of the previous one with weak van der Waals forces, and so creating a graphite crystal. This piling up of layers was found to happen with the carbon atoms of a graphene sheet placed on the center of the hexagons in the underlying layer, which is called an AB or Bernal stacking [20] (displayed in Figure 1.3d).

In an sp_3 bonding configuration, pairs of electrons are shared between the atoms forming only σ (sp_3: one s-orbital and three p-orbitals) covalent bonds, and the carbon atoms are forced to arrange themselves in a tetrahedral cubic crystal structure we call diamond (c-C). When the material contains micrometer-size parts of both types of crystals, graphite and diamond, in a carbon matrix we say it is polycrystalline amorphous carbon (a-C), and that is what we sometimes call coal (typically mixed with other elements).

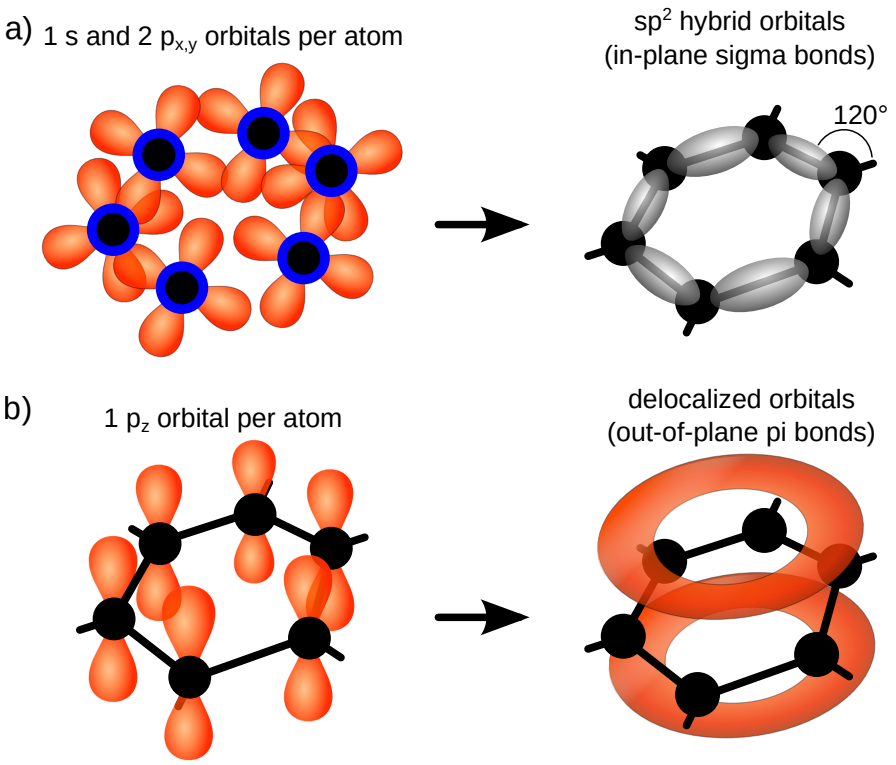

Figure 1.4: The atomic configuration of graphene consists of a) σ covalent bonds (sp_2: one s-orbital and two p-orbitals) with 120◦ angles between them, and b) π covalent bonds formed by the partial and lateral overlap of the p_z-orbitals perpendicular to the sp_2-hybrid orbitals. Adapted from Wikimedia Commons [24, 25].

Many other materials were studied in parallel to graphite, although there is one to mention for its similarities (yet underrated recognition): boron nitride. Boron nitride is a compound of boron ($^{11}_{5}$B) and nitrogen ($^{14}_{7}$N) that, despite the recent discovery of its natural occurrence in 2009 [26], is known since 1842 when William H. Balmain synthesized it for the first time [27]. Powders of amorphous boron nitride (a-BN) can be produced from boric acid or boron trioxide –obtained from borate minerals (borax or sassolite)– in an atmosphere of nitrogen, and a further heating process crystallizes the material into hexagonal boron nitride (h-BN)[28]. The crystalline structure of h-BN resembles that of graphite, having its softness when ground reported in 1850 [29]. It was found to be also a great refractive material like graphite [30], although its white color gives it away. All together made this material win the pseudonym of "white graphite". The creation of cubic boron nitride (c-BN) in 1957 by chemist Robert H. Wentorf [31] was a milestone and this "white diamond" was commercialized under the name borazon. All these allotropes can be seen in Figure 1.5 together with the phase diagram of boron nitride.

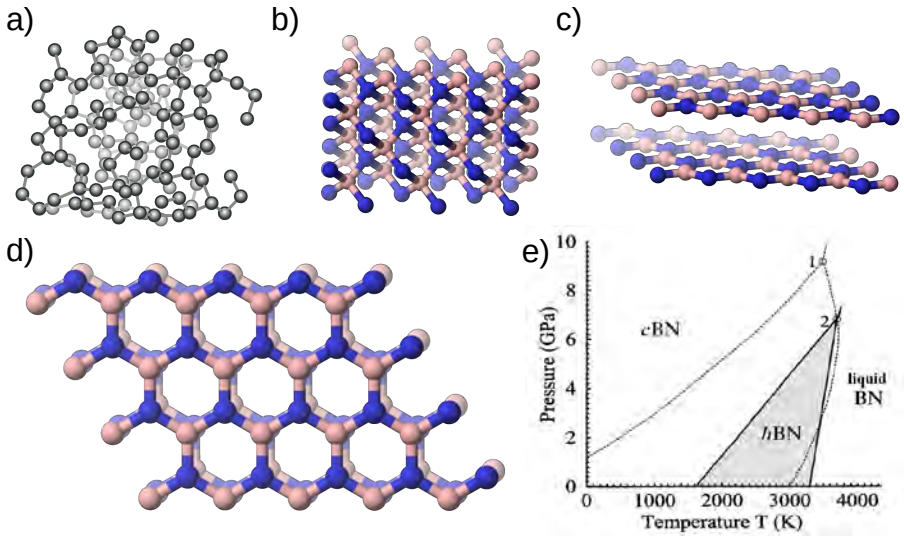

Figure 1.5: Boron nitride allotropes: a) amorphous boron nitride, b) cubic boron nitride (c-BN), and c) hexagonal boron nitride (h-BN). d) Similarly to graphene, single-layer h-BN has a sp_2 configuration with σ and π covalent bonds, although they are slightly ionic in-plane and out-of-plane. e) Phase diagram of boron nitride (adapted from reference [32]). a-d) adapted from Wikimedia Commons [21, 33, 34, 35].

The structure of h-BN was studied and determined during the golden age of crystallography [28, 36, 37]. Equivalent to graphite, this compound crystal has an sp_2 bonding configuration between the B and N atoms, also resulting in σ and π covalent bonds and a planar hexagonal crystal structure (single-layer h-BN). However, the bonds are slightly ionic (both in plane and between layers) and the h-BN sheets attach to each other in an AA'-stacking with the B sitting on top of N, and *viceversa*.

Graphite and h-BN are a single-element and a compound layered materials, respectively, but there are many other ones. For instance, transition metal dichalcogenides (TMDs) such as MoS_2 and $TaSe_2$ combine sets of a transition metal atom (M=Mo,W,Ta) and two chalcogen atoms (X=S,Se,Te) to also form a hexagonal arrangement (h-MX_2) as displayed in Figure 1.6. Layered materials share many properties such as high thermal conductivity along the layers (basal plane) but not between layers (edge/normal plane). However, the main difference appears in the electrical properties: graphite is a conductor (semi-metal), while h-BN is a wide-bandgap insulator (4-6 eV) and TMDs are usually semiconductors (Figure 1.6).

The differences between graphite and molybdenite (MoS_2) went unnoticed for long time as, at the end, they were used for the same applications: drawing and lubricating (graphite and molybdenum were also used for high-temperature molding). Despite that many experiments led to their differentiation, it took centuries of scientific research (until nowadays) to be able to explain what makes them special: their structure made out of almost-floating layers held by van der Waals forces.

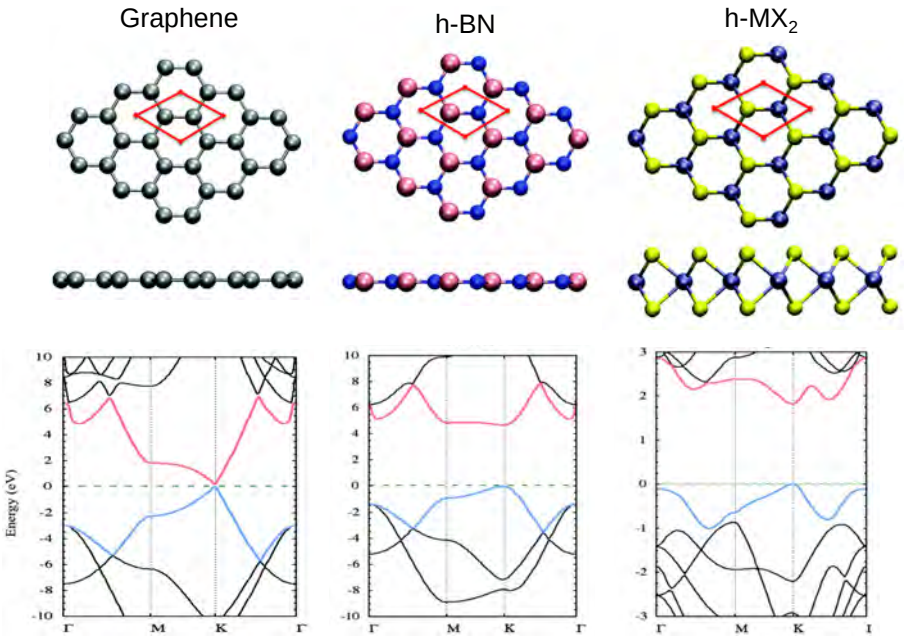

Figure 1.6: Structure of graphite, h-BN and h-MX_2 (such as MoS_2 or $TaSe_2$). The panels below show the theoretical band structures of their single layer counterparts (MoS_2 in the case of h-MX_2). Blue and red lines correspond to the valence and conduction bands, respectively. Figure adapted from reference [38].

The drawing property originates from their easy peeling or exfoliation of layers when rubbed against a harder material. The same applies for their application as lubricant additives when dispersed in a liquid solution. Graphite, MoS_2 and h-BN can be placed as interfacing filling in lubricant oil, grease, water or solvents between two solids such as machine engines to reduce their friction: the energy that would be converted in heat is instead used in displacing the layers with respect to each other or simply separating them. The weak "coupling" between layers of these materials also causes the bad heat transmission across the layer planes. In the case of graphite and h-BN, this thermal isolation allows -together with their chemical instability and high melting points- the confinement of other materials at very high temperatures as for melting the aforementioned British cannonballs.

In the present, we have learned to isolate and identify single layers of these crystals and, given their confinement in one of the dimensions, we call these allotropes *two-dimensional (2D) materials* [38, 39]. Their properties can be different than their bulk counterparts or simply remain the same despite their one-atom thickness, hence bringing the functionality of matter to the ultimate limit. We can also combine different types to fabricate materials *à la carte*, and these artificial stacks are known as *van der Waals heterostructures* [40, 41].

1.2.1. GRAPHENE

Graphene is a single layer of graphite [42, 43, 44]. It is composed by carbon atoms arranged in a honeycomb or hexagonal configuration (two atoms per parallelogram primitive cell) composed of two triangular sublattices. Since its isolation in 2004 by peeling graphene layers from bulk graphite (micromechanical cleavage or Scotch tape technique) [45], the unique properties of this first 2D material have been studied exhaustively. Graphene has excellent electrical properties [46, 47], with electron mobilities up to 200000 $cm^2 \cdot V^{-1} \cdot s^{-1}$ if defect-free and without substrate effects (limited by phonons at room temperature) [48, 49]. Phonons –collective vibrations of atoms in the lattice– travel efficiently hence resulting in a large thermal conductivity of 5300 $W \cdot m^{-1} \cdot K^{-1}$ [50]. The hexagonal disposition of carbon atoms caused by their covalent sp^2 bonding gives graphene a large fracture strength (130 GPa) and stiffness (Young's modulus of 1 TPa) [51]. And despite the apparent space in the center of the hexagons, their energy barrier prevents even the smallest gas molecule, helium, to cross a graphene membrane, hence granting its impermeability property [52].

As a result of these properties, many applications arise: faster transistors [53] and very-dissipative interconnects (for thermal management) [54], precise magnetic field detectors [55], outperforming micro/nano electromechanical systems (M/NEMS) [56], mechanically- enhanced and electrically-enabled composites[57], sensitive pressure and gas devices [58, 59], water and toxic compound filtration membranes [60], etc. With all its properties, graphene is expected to reach the markets [61, 62, 63]. A promising means for industrial scale production of graphene and other 2D materials is the use of the chemical vapor deposition (CVD) technique on catalytic foils such as copper [64, 65], nickel [66] or germanium [67].

1.2.2. SINGLE-LAYER H-BN

Hexagonal boron nitride (h-BN), also known as 'white graphite', is a layered material consisting of partially-ionic sp^2-bonded boron and nitrogen atoms in a honeycomb arrangement with a van der Waals and slightly ionic AA' stacking [68, 69]. h-BN is a III-V indirect wide-bandgap semiconductor (5-6 eV) [70] that has proven to be the complement insulating material for graphene electronics [71]. The larger chemical and thermal stability of bulk h-BN compared to graphite has enabled applications in harsh environments such as deep ultraviolet photodetectors for space research [72, 73] and high-performance lubricants [74].

Among all the 2D materials, few studies on single-layer h-BN exist to date [75, 76] despite the early attempts to exfoliate it [77] and the well-developed synthesis techniques [78, 79, 80, 81, 82, 83, 84]. The reason for its difficult exfoliation to a monolayer thickness is unclear, possibly being its AA' stacking, its slightly-ionic bonds or atomic flatness that causes adhesion between h-BN layers and other surfaces stronger than other 2D materials [85, 86, 87, 88]. Moreover, h-BN surfaces are hydrophilic in nature, but after being exposed to air they get covered by an hydrophobic layer of hydrocarbons as reported in h-BN nanotubes [89] and graphene [90]. Understanding the adhesion, friction and other properties of single-layer h-BN can pave the way to promising applications such as deep ultraviolet single photon emitters [91, 92], ultrathin piezotronics [93, 94], and to exploit its natural hyperbolic optical dispersion properties [95] and proton conduction [96].

1.3. 2D MEMS

Of all 2D materials studied at present, graphene is the strongest and best electrical conductor [97, 98]. Freestanding graphene promises to be the ultimate material for micro-/nano-electromechanical systems (M/NEMS), showing potential as RF oscillators [99, 100], pressure sensors [58, 59], and electromechanical switches [101].

Suspending graphene membranes on circular cavities or trenches eliminates the negative impact of the substrate on its electrical conductivity [97, 98, 102, 103, 104], which even allows the graphene to emit light in the visible spectrum [78], and enables electro- or opto-mechanical actuation for mass, force and position sensing [62]. However, fabrication of freestanding membranes requires a complicated transfer process that impacts device performance negatively [105] and results in a low device yield [106]. Moreover, these movable devices are fragile and tend to break or collapse during fabrication or measurement [107].

Single-layer graphene (SLG) drums have been extensively studied, showing unique mechanical properties [51, 102, 108, 109, 110]. Many groups have demonstrated the scalability of CVD SLG drums and analyzed the statistical variation of their mechanical properties by measuring several drums with laser interferometry [105, 111], Raman spectroscopy [106, 112, 113], and atomic force microscopy [114, 115]. However, any attempt to commercialize graphene mechanical sensors is ineffective unless a characterization technique that is parallel, contactless, and affordable at the same time becomes available. Furthermore, CVD SLG usually contains gas permeable lattice defects and nanoscale pores due to its growth on imperfect substrates [116], which blocks its application in gas pressure sensing devices that require impermeable membranes. A possible route to overcome this difficulty is to stack several CVD layers to reduce the probability of having nanopores from different layers aligned on the same spot [117].

1.4. THESIS STRUCTURE

The structure of this thesis follows a dual story with two interspersed themes. On one hand, it is a chronological guide of techniques that were tested or developed, and at the same time it is an exploration of different materials for particular applications. Therefore, the thesis is divided in application parts comprising chapters discussing techniques and findings related to the given material:

- **Application 1: $TaSe_2$ for write-once-read-many (WORM) memory devices** contains *Chapter 2: High-Q mechanical resonators by laser-oxidation of $TaSe_2$*. In this chapter, we introduce the laser interferometry setup to study the dependence of the mechanical resonance frequency on the thickness of tantalum diselenide ($TaSe_2$) drumheads. We observe a continuous transition from plate to membrane behavior when reducing the thickness from 100 nm to 6 nm, and we prove the large effect of stress on the resonance frequency of 2D materials by laser-oxidation of the thin membranes. This selective laser-oxidation is comparable to the laser-recording of CD-R and DVD-R optical disks, and therefore each of these $TaSe_2$ NEMS could be a bit of a write-once-read-many (WORM) memory unit.

- **Application 2: CVD graphene and h-BN for optomechanic sensing** spins around the use of NEMS membranes made out of two prominent materials made by chemical vapor deposition: double-layer graphene and single-layer hexagonal boron nitride. Mechanical sensors to study quantum phenomena and light-matter interactions have been proposed and demonstrated with graphene, although h-BN might be more suitable for those applications due to its lower optical absorption.
  In *Chapter 3: Laser-induced tensioning of CVD double-layer graphene drumhead resonators* we perform a small statistical analysis on the fundamental resonance frequency of CVD DLG drumheads to find its theoretical dependence with the device diameter by means of laser interferometry. Variations of the mechanical resonance are attributed to difference in tension of the membranes, which are compared to values obtained by nanoindentations with an atomic force microscope. The cleanliness of the drums is discussed together with the pressure-induced destruction of the larger devices. Furthermore, the invasive nature of the laser technique due to the heat impact on the measurements is exposed by providing evidence of softening and tensioning of the membranes and their photothermal self-oscillation at higher laser powers. This allow us to present a new theory that explains the heating effects from the laser to the resonance frequency and quality factor of these membranes as a function of thermally-induced variation of the sidewall length.
  Chapter 4: Mechanical characterization and cleaning of CVD SL h-BN resonators explores the use of a known material whose single-layer counterpart remained to be mechanically characterized until now and it has been marginalized in solo applications. In this chapter, we fabricate drums of 5 μm in diameter, extract their mechanical properties with the laser and atomic force microscope techniques, and study their behavior when cooling them to cryogenic temperatures (3 K). The process is repeated after a series of cleaning steps to demonstrate a route for reducing the contamination in this type of fragile structures while exploiting the inorganic nature of this material. We also propose a model that describes an adhesion-mediated influence of temperature on the mechanics of certain 2D materials, which should be taken into consideration when trying to answer subtler scientific questions.

- **Application 3: CVD graphene for pressure sensing** describes the colorimetry technique and the uses we have given to the color-changing of double-layer graphene drumheads. The need of a non-invasive technique that enables an industrial characterization of arrays of devices, together with the large absorption of light of two layers of graphene, resulted in the creation of a new and scalable way of testing membranes suspended on cavities. The 2-atom-thick material happened to become a platform in itself to observe and measure the behavior of these ultrathin membranes with only a common optical microscope.
  In *Chapter 5: Massive characterization of graphene mechanical devices using a colorimetry technique*, we analyze several samples with single- and double-layer graphene drumheads of different diameters and cavity depths in a very large scale fashion. With the colorimetry technique, we obtained the statistical probabilities of a given device

geometry to survive a pressure difference of 1 atm. We found that the device yield follows a trend ruled by a scaling parameter, and that the survival probability improves considerably when using two instead of one material layers. Moreover, we extracted the adhesion energy of the double-layer graphene by studying membranes stuck to the bottom of their cavities. This work paves the way for the scaling-up of 2D mechanical pressure sensors.
Chapter 6: Colorimetry technique for scalable characterization of suspended graphene brings the technique to another level where we can extract the pressure-induced deflection of the membranes as a function of time, and therefore measure their gas permeability. The observation of Newton's rings enabled their exploitation for exploring the large deflection regime of these membranes dominated by the Young's modulus. A look into the pressure decay in the small deflection regime allowed us to measure the permeance of a membrane, and we found that gas molecules escape from these devices faster than when they have to enter in sealed cavities under vacuum. These findings point to a research direction that will explain the leaking mechanisms of these supposedly-impermeable membranes to move towards the realization of hermetic gas and pressure sensors.

- **Killer application: CVD graphene for interferometry modulation displays (IMOD)** introduces the main innovation in this dissertation: Graphene Interferometry MOdulation Displays (GIMODs). *Chapter 7: Graphene Interferometry MOdulation Display* combines the colorimetry technique with electrostatical actuation to study the dynamical movement of double-layer graphene membranes stroboscopically. The tension of the membranes was extracted non-invasively while vibrating them at frequencies up to 2 kHz without observing mechanical delays nor gas damping, hence proving the suitability of this type of mechanical pixels for applications requiring high refresh rates. The demonstration of GIMOD technology in the Mobile World Congress 2017 in Barcelona served as a test to validate the usefulness of such kind of displays, having a successful welcoming among the industry.

- **Future Applications** (Chapter 8) concludes the thesis with some promising uses of 2D materials in the coming years. A continuation of the study on large populations of graphene NEMS will give a non-speculative prediction of the actual applications of those devices for pressure and gas sensing. Statistics on the permeability of CVD graphene with different layers could reveal the feasibility of hermetic sensors or molecular sieves. Moreover, their optical properties should be improved to make the GIMOD technology competitive. This could also be used in other technologies that require weightless and robust materials with high optical reflectivity such as light sails and other space applications.

Application 1: $TaSe_2$ for write-once-read-many (WORM) memory devices

2

HIGH-Q MECHANICAL RESONATORS BY LASER-OXIDATION OF $TaSe_2$

¿Cuántos, en la vida, huyen de otros porque no se ven a sí mismos?
("How many [people], in life, run away from others
because they do not reflect on themselves?")

The Life of Lazarillo de Tormes and of His Fortunes and Adversities, Anonymous

You are the owner of your Future.

Santiago, Copenhagen 2008

Controlling the strain in 2D materials is an interesting avenue to tailor the mechanical properties of nano-electromechanical systems. Here we demonstrate a technique to fabricate ultrathin tantalum oxide mechanical resonators with large stress by laser-oxidation of drumhead resonators made out of tantalum diselenide ($TaSe_2$), a layered 2D material belonging to the metal dichalcogenides. Prior to the study of their mechanical properties with a laser interferometer, we checked the oxidation and crystallinity of the freely-suspended tantalum oxide in a high-resolution electron microscope. We show that the stress of tantalum oxide resonators increases by 140 MPa (with respect to pristine $TaSe_2$ resonators) which causes an enhancement of quality factor (14 times larger) and resonance frequency (9 times larger) of these resonators.

Parts of this chapter have been published in Nano Research **8**, 2842–2849 (2015) by S.J. Cartamil-Bueno, P.G. Steeneken, F.D. Tichelaar, E. Navarro-Moratalla, W.J. Venstra, R. van Leeuwen, E. Coronado, H.S.J. van der Zant, G.A. Steele, and A. Castellanos-Gomez.

2.1. INTRODUCTION

2D layered materials are attractive for high-frequency nanomechanical systems, which can be used in sensing applications. The reduced thickness and small mass of these materials enable high resonance frequencies f_0 and fast response times, whereas their low flexural rigidity increases the responsivity and allows size reduction. For low-noise operation of nano-mechanical systems it is desirable to achieve high quality factors Q at high frequencies. In conventional nanomechanical systems, based on silicon nitride (Si_3N_4) beams, it has been shown that both f_0 and Q can be enhanced by increasing the stress in the beam [118, 119]. For this purpose, several methods have been proposed to tune the stress in nanomechanical systems based on 2D materials using temperature, mechanical actuators and gas pressure [120, 121, 122, 123]. For permanent stress modification in polycrystalline graphene, a method for direct bonding between graphene platelets has been proposed [123]. Since the mechanical properties of suspended crystalline 2D materials attract much attention for sensing applications, it is of scientific and technological interest to develop methods for local stress engineering in single-crystalline 2D materials. In this work we report a method that permanently modifies the stress in suspended single-crystalline 2D materials. We use a focused laser to locally increase the temperature of tantalum diselenide ($TaSe_2$) drumhead resonators until they undergo an oxidation process which results in a drastic increase in the pre-stress of the selected 2D resonators. We investigate the effect of this increased pre-stress on the Q factor and resonance frequency, and find a large enhancement for both of them in thin resonators (<20 nm thick). It thereby provides a route towards higher f-Q products in layered material resonators. The stress and thickness dependence of the Q factor are observed to be governed by the same model that was proposed to describe the Q factor of stressed Si_3N_4 beams [118, 119, 124].

2.2. FABRICATION AND SETUP

TaSe2 crystals are synthesized from the elemental components in a two-step process. Polycrystalline $TaSe_2$ is obtained by ceramic combination of stoichiometric ratios of Ta and Se. Ta powder, 99.99% trace metals basis and Se powder, -100 mesh, 99.99% trace metals basis are used. Powdered starting materials are intimately mixed, placed inside an evacuated quartz ampoule and reacted at 900°C for 9 days. The resulting free-flowing glittery grey microcrystals are then transformed into large single-crystals using the chemical vapor transport (CVT) methodology. For that purpose, 1 g of $TaSe_2$ polycrystalline material together with 275 mg of I_2 are loaded into a 500 mm long quartz ampoule (OD: 18 mm, wall-thickness: 1.5 mm). The mixture is placed at one end of the ampoule which is exhaustively evacuated and flame-sealed. The quartz tube is finally placed inside a three-zone split muffle where a gradient of 25°C is established between the leftmost load (725°C) and central growth (700°C) zones. A gradient of 25°C is also set between the rightmost and central regions. The temperature gradient is maintained constant during 15 days and the muffle is eventually switched off and left to cool down to ambient conditions. Millimeter-size $TaSe_2$ crystals are recovered from the ampoule's central zone, exhaustively rinsed with di-

ethyl ether and stored under a N_2 atmosphere.

Freely suspended $TaSe_2$ layers are fabricated by mechanical exfoliation of the synthetic $TaSe_2$ crystals onto a substrate with microcavities. The substrate is fabricated from Si wafers with 285 nm of thermally grown SiO_2, and contains circular cavities of that depth and a diameter of 3.2 μm. The SiO_2 thickness of 285 nm is ideal as the optical contrast of the thinner flakes is enhanced. As recently demonstrated for MoS_2 flakes [125], the all-dry transfer technique based on elastomeric stamps was employed. $TaSe_2$ flakes are deposited on an elastomeric stamp (GelFilm by GelPak) by mechanical exfoliation of synthetic $TaSe_2$ with blue Nitto tape (Nitto Denko Co., SPV 224P)[126]. Flakes of different thicknesses are identified on the surface of the viscoelastic stamp by transmission mode optical microscopy, and the stamp containing the chosen $TaSe_2$ flake/s is mounted in a micromanipulator facing the patterned substrate. The stamp is brought into contact with the patterned substrate by lowering the manipulator to lastly be peeled-off very slowly using the micromanipulator.

The resulting resonators are inspected with an optical microscope (Olympus BX 51 supplemented with a Canon EOS 600D camera) as shown in Figure 2.1.

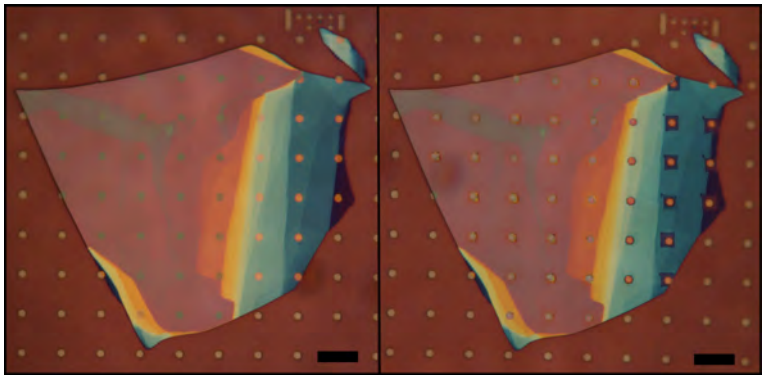

Figure 2.1: Optical images of the $TaSe_2$ flake on a Si substrate with circular cavities before (left) and after (right) oxidation. Scale bars are 15 μm.

2.2.1. LASER-OXIDATION OF $TaSe_2$

A Renishaw in via system is used to scan a focused laser spot (λ = 514 nm) over the $TaSe_2$ flakes, resulting in square-shaped oxidized regions, as displayed in the right panel of Figure 2.1. The oxidation of material is found to occur at a power of 25 mW for 0.1-0.2 s of exposure time. The scanning step in the irradiation process is 300 nm.

2.2.2. LASER INTERFEROMETRY

The frequency response of the resonators is measured using an optical interferometer described in Figure 2.2 [108, 127]. We analyze the fundamental mode, which is easily identified as it shows the lowest frequency and highest intensity among all the mechanical resonance

peaks in the spectrum (Figures 2.3 and 2.4).

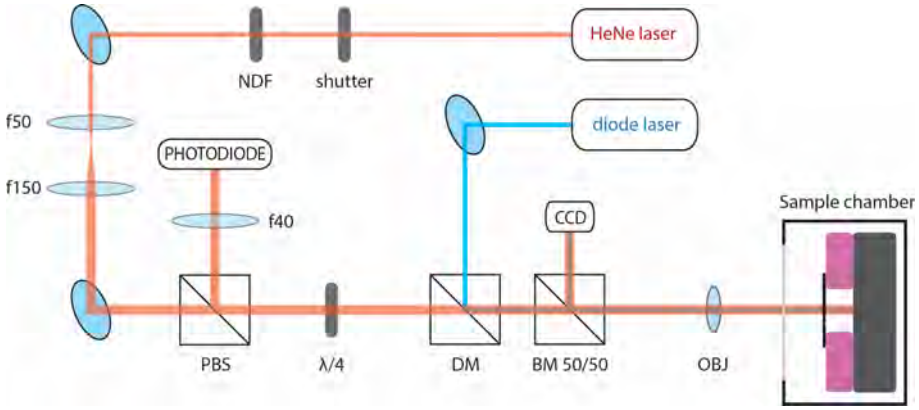

Figure 2.2: Optical interferometer setup to measure the motion of 2D resonators. Abbreviations: NDF - neutral density filter, PBS - polarizing beam splitter, DM - dichroic mirror, BM - 50/50 beamsplitter, CCD - camera, OBJ - 50× objective lens. The diode laser and photodiode are connected to a vector network analyzer (not shown). The laser spot on the device is diffraction-limited (about 450-700 μm in diameter).

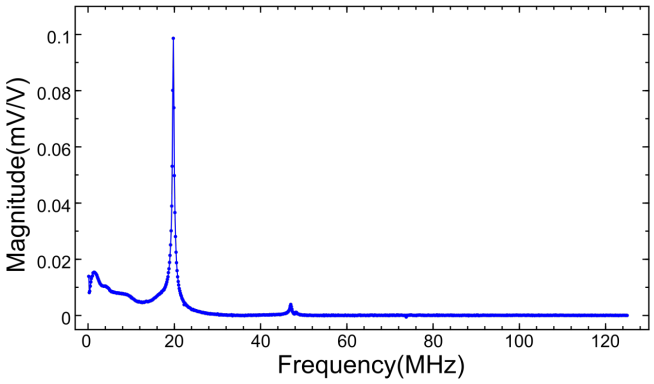

Figure 2.3: Mechanical frequency response spectrum of a $TaSe_2$ drumhead resonator of 3.2 μm diameter.

The suspended material is photothermally actuated with an intensity modulated blue diode laser (Thorlabs LP405-SF10, $\lambda = 405$ nm) at a power of 260 μW, while a second constant-power linearly-polarized Helium-Neon laser ($\lambda = 632.8$ nm) at 4 mW is used as optical probe for the detection. The measurements are carried out in vacuum ($\sim 10^{-5}$ mbar) at room temperature. The power from the He-Ne laser is adjusted with a neutral density filter, and a beam expander enlarges the beam diameter by a factor of three to match the aperture of the objective lens. The beam passes a polarized beam splitter and a quarter wave plate, and is combined with a blue laser, which is intensity-modulated by a vector network analyzer

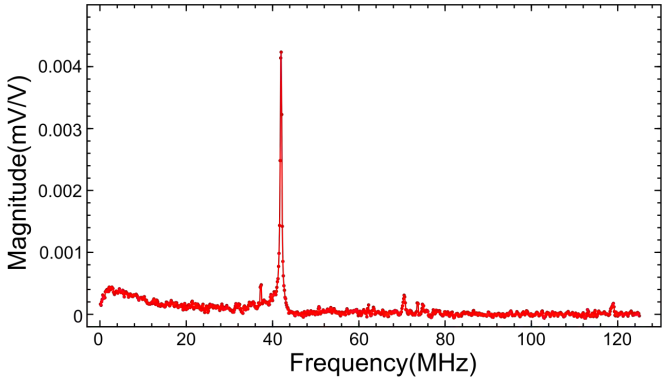

Figure 2.4: Frequency spectrum of a laser-oxidized $TaSe_2$ drumhead resonator of 3.2 μm diameter.

(from a typical optical modulation depth of 4 μW as measured at the diode laser output, up to 137 μW for the oxidized drums) for high frequency photothermal excitation. The combined red and blue light is focused on the suspended drumhead with a microscope objective lens (Leica 50×, NA=0.6). The reflected light goes back through the objective lens, and part of it is sent to a CCD camera (due to the beam splitter 50/50) which is used for visual inspection and alignment. The reflected blue beam is taken out of the main path by the dichroic mirror. The reflected red light is phase-shifted again and directed towards a high speed photo-detector (NewFocus 1601) as explained above. The detector output is connected to the input port of a network analyzer (Rohde & Schwartz, ZVB4).

As the suspended material is very thin, most of the light is transmitted through the flake and reflected at the bottom of the cavity. However, a small part of the light is reflected at the material surface, and it interferes with the reflected light from the cavity with a difference in phase that depends on the deflection of the resonator (length of the cavity), and which changes with time as the resonator moves. The modulation of the reflected signal is maximum when the drumhead is actuated at its resonance frequency.

2.3. MATERIAL CHARACTERIZATION OF $TaSe_2$ BEFORE/ AFTER LASER-OXIDATION

2.3.1. CRYSTALLINITY AND STOICHIOMETRY BY TEM

A high-resolution transmission electron microscope (TEM, Tecnai F20ST/STEM 200 kV) with Elemental Dispersive X-ray (EDX) detector is used for atomic resolution imaging and analysis of the elemental composition. Mechanically exfoliated $TaSe_2$ flakes are deposited onto a 200 nm Si_3N_4 membrane with holes (2.5 μm in diameter), using a dry transfer technique [125]. A focused green laser is scanned over part of the flakes to induce the local laser-oxidation in a confocal microscope system operated in air. Figure 2.5a shows a transmission mode optical image of the partially oxidized 50 nm thick $TaSe_2$ flake. The regions

labeled with "1", "2" and "3" in Figure 2.5a correspond to the pristine flake, laser-exposed flake and bare Si_3N_4 membrane, respectively. A dramatic difference in the optical properties is observed between pristine and laser-exposed areas of the flake even though the change in thickness of the laser-irradiated flakes was small (~3 nm), as found from atomic force microscopy (AFM). The optical transmittance of the suspended flake increases from 0.4 to 0.9 by the laser exposure, indicative of a reduced absorption coefficient of the material as expected for tantalum oxide.

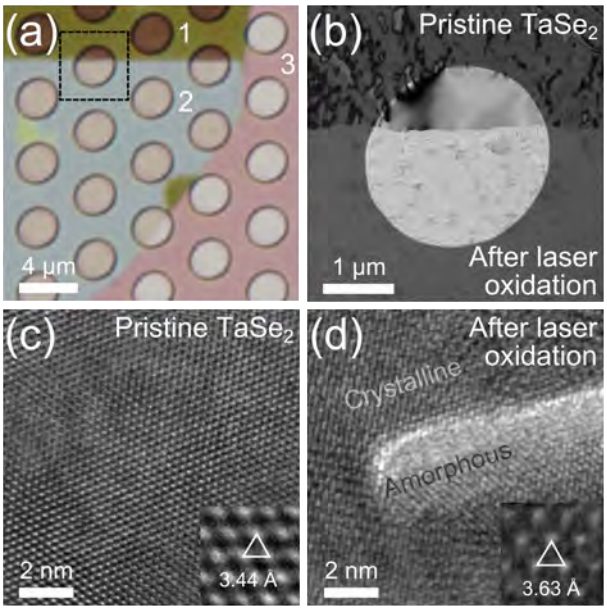

Figure 2.5: Characterization of a $TaSe_2$ flake before and after laser-oxidation. (a) Transmission optical image showing pristine (1) and laser-oxidized (2) regions of the $TaSe_2$ flake on a silicon nitride membrane TEM grid (3) with circular holes. (b) Bright field TEM image of the partially oxidized suspended flake indicated by the dashed box in (a). (c) HRTEM image of suspended pristine $TaSe_2$. The interatomic distance (3.44 Å) corresponds to the Ta-Ta distance in the {1100} plane of 2H-$TaSe_2$ [128]. (d) HRTEM image of a laser-oxidized region showing coexisting amorphous and crystalline phases. The interatomic distance in the hexagonal crystal plane has increased to 3.63 Å

To investigate the changes in chemical composition caused by laser-irradiation of $TaSe_2$ we carried out EDX measurements on freely suspended areas of the material. Composition analysis shows an approximate ratio of Ta/Se/O = 1.0/2.3/0.4 in the pristine flake. The presence of oxygen in EDX is attributed to surface oxidation of the $TaSe_2$ under atmospheric condition [128]. Interestingly, after laser exposure the composition of the flake is Ta/Se/O = 1.0/0.0/3.8, which indicates that the laser-irradiation procedure in air oxidizes the flake, removing the selenium atoms and replacing them by oxygen. Thus, laser exposure converts the $TaSe_2$ into tantalum oxide. EDX data taken on the pristine flake and on both crystalline and amorphous regions of the oxidized flake are shown in Table 2.1. Note, that this com-

	O	Se	Ta
Pristine 1	62	24	11
Pristine 2	12	61	27
Oxide crystalline 1	80	1.7	19
Oxide crystalline 2	82	0.3	17
Oxide crystalline 3	77	0.2	23
Oxide amorphous 1	75	1.7	23
Oxide amorphous 2	75	0.7	24

Table 2.1: EDX atomic concentration quantification before and after laser oxidation. Atomic % relative uncertainty is 20%. The label numbers only indicate a different spot of the same region.

positional analysis has an uncertainty of ±20% hampering the determination of the exact stoichiometry after laser-oxidation. So even though the O/Ta ratio determined by EDX is too large for Ta_2O_5, one cannot rule out that this tantalum oxide is Ta_2O_5 due to uncertainties in EDX and the presence of surface oxides.

In order to determine the effect of laser oxidation on the flake's crystal structure, we performed a TEM analysis on the suspended flake. Figure 2.5b shows a bright field TEM image of the region highlighted with a square in Figure 2.5a. The transition boundary between the pristine (top) and oxidized (bottom) part of the flake is abrupt (<50 nm). A High Resolution TEM (HRTEM) image of the pristine suspended $TaSe_2$ is shown in Figure 2.5c, demonstrating a hexagonal atomic configuration, which is confirmed by Selective Area Diffraction Pattern (SADP) analysis.

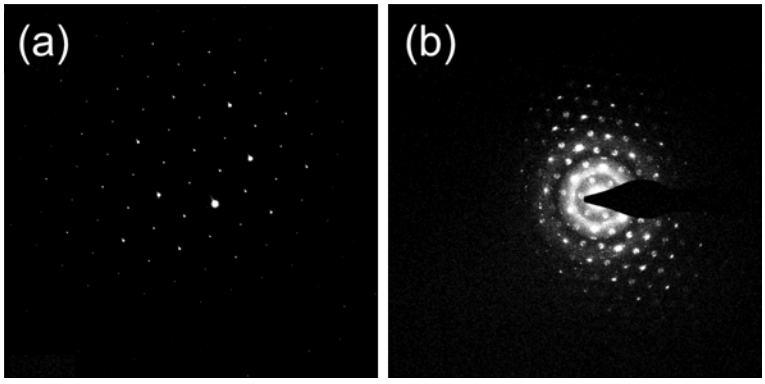

Figure 2.6: (a) SADP of the pristine single crystal flake. The reflections close to the origin are of type <1100> with d spacing 2.98 Å. (b) SADP of a laser-oxidized area.

Figure 2.6a shows SADP patterns of the crystalline pristine and oxidized flake. The lattice spacing of the crystals can be deduced according to $d = \lambda_e L/D$, where d is the lattice spacing, λ_e is the electron wavelength, L the camera length and D the distance measured on the

CCD detector from the reflected beam to the undiffracted beam. The measurement uncertainty is usually 1-2%. The lattice spacing between the crystal planes in the pristine flake is found to be d_{pris} = 2.98 Å, in correspondence with a Ta-Ta spacing of $2d/\sqrt{3}$ = 3.44 Å in 2H-$TaSe_2$ [128]. After oxidation, the SADP becomes more complex, as is shown in Figure 2.6b. The dominant hexagonal pattern shows d = 3.14 Å as lattice spacing, rather different from the pristine part (2.98 Å). In between the dominant reflections vague rings exists, indicative of small ordered areas. Ordered because they correspond to twice the 3.14 Å spacing, and small because the reflections are wide. In the background, vague rings can be seen, that correspond to amorphous regions as is confirmed from a separate SADP on the amorphous area showing similar amorphous rings.

The crystal structure and lattice constant from HRTEM and SADP are consistent with an in-plane orientation of the layered 1100 planes of 2H-$TaSe_2$ with an interatomic Ta-Ta spacing of 3.44 Å (inset). Figure 2.5d presents a HRTEM image of the oxidized region of the suspended material. Both amorphous and crystalline regions are observed. In the crystalline domains, HRTEM (inset) and SADP show a hexagonal configuration with an interatomic Ta-Ta spacing of 3.63 Å, larger than in $TaSe_2$. The hexagonal structure and Ta-Ta distance obtained from TEM of laser oxidized $TaSe_2$ matches that of TT-Ta_2O_5 (also called δ-Ta_2O_5) [129, 130, 131]. Together with the Raman spectrum and photoluminescence spectra of the oxidized flake corresponding to that of Ta_2O_5 (section below) [132], we can conclude that the modification is the oxidation reported in $TaSe_2$ when heated up to around T_{ox} = 600°C [133], which results in a crystal structure that bears most resemblance to TT-Ta_2O_5.

The oxidation process in the suspended $TaSe_2$ happens as follows. Once the temperature of $TaSe_2$ is increased over that critical temperature T_{ox} by laser-heating, it oxidizes and becomes more transparent. The increased transparency reduces light-absorption and thus leads to a temperature reduction in the flake. Thus, despite inhomogeneities in the laser power and thermal resistances over the flake, this self-limiting mechanism prevents the flake from exposure to temperatures significantly higher than T_{ox}. This effect also prevents ablation [134], and improves the homogeneity of both the composition and stress in the oxidized film.

2.3.2. VIBRATION AND PHOTOLUMINESCENCE BY RAMAN SPECTROSCOPY

Micro-Raman spectroscopy on a $TaSe_2$ flake over SiO_2/Si was carried out with the same Renishaw in Via Raman microscope that was used for the laser oxidation in order to obtain more information about the material after laser exposure. Measurements were performed in backscattering configuration excited with visible laser light (λ = 514 nm) on the suspended part of a $TaSe_2$ drum and on its surroundings [126]. The spectra are collected through a 100× objective (NA = 0.95) and recorded with a 1800 lines/mm grating providing a spectral resolution of ~0.5 cm^{-1}. During the characterization, the laser power is kept at low power levels, $P \sim 250$ μW.

Raman spectroscopy revealed that the suspended part was more easily oxidized and with less exposure time than the regions on top of the substrate. This is attributed to a higher

thermal resistance of the suspended part of the flake, as a consequence of which less heating power is needed to reach the oxidation temperature. Figure 2.7 displays the Raman spectrum for $TaSe_2$ before laser-exposure in a suspended region. The Raman spectrum shows the E_{12g} and A_{1g} peaks and a background signal. After laser-exposure (Figure 2.8), a feature around 255 cm^{-1} appears. This Raman peak is at the same energy as the most characteristic Raman peak for crystalline Ta_2O_5 in that part of the spectrum [132]. Moreover, two broad peaks around 1350 cm^{-1} and 1550 cm^{-1} develop, corresponding to a photoluminescence emission around 550 nm to 560 nm, respectively. Similar photoluminescence emission has been reported for Ta_2O_5 [135, 136].

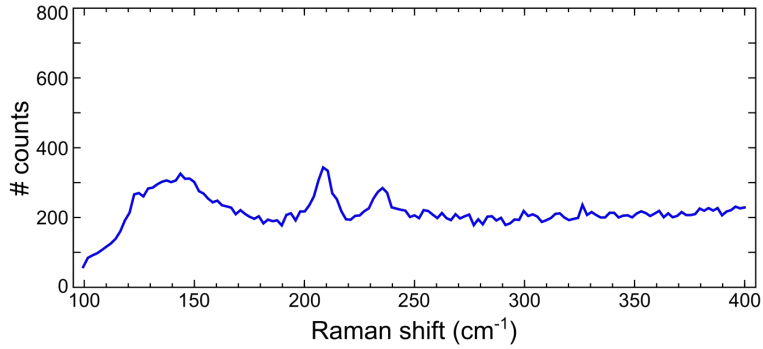

Figure 2.7: Raman spectrum of a $TaSe_2$ flake in a suspended region. The characteristic E_{12g} (210 cm^{-1}) and A_{1g} (235 cm^{-1}) peaks are visible.

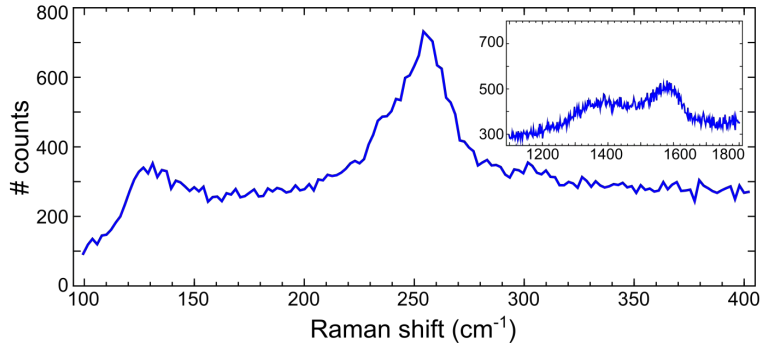

Figure 2.8: Raman spectrum of a laser-oxidized $TaSe_2$ region. A prominent peak appears around 255 cm^{-1}, which matches the same energy of the main Raman peak for crystalline Ta_2O_5. Inset: two broad peaks around 1350 cm^{-1} and 1550 cm^{-1} are also visible, corresponding to similar photoluminescence emission as reported for Ta_2O_5.

2.3.3. THICKNESS OF RESONATORS BY AFM

An atomic force microscope (AFM, Digital Instruments D3100) with cantilevers (Budget-Sensors, spring constant 40 N/m, tip curvature <10 nm) is operated in the amplitude modulation mode to study the topography and to determine the thickness of the flakes. The thickness of the drums is determined both before and after laser-oxidation by measuring step heights. The measured thickness reduction after laser-oxidation is typically 3±1 nm, independent of the initial flake thickness.

2.4. MECHANICAL CHARACTERIZATION OF RESONATORS BEFORE/ AFTER LASER-OXIDATION

After having established the effects of laser-oxidation on the composition and crystal structure of $TaSe_2$, we now study its effects on the mechanical properties of drumhead resonators. $TaSe_2$ drumhead resonators are fabricated by transferring mechanically exfoliated $TaSe_2$ flakes onto a SiO_2/Si substrate with circular cavities of 3.2 μm in diameter and 285 nm in depth. The mechanical properties of the drumhead resonators are investigated by measurement of their fundamental mechanical resonance mode using the optical interferometer setup described above [108, 127]. The mechanical spectrum is measured over a wide frequency range, although we use only the fundamental mode for the analyses.

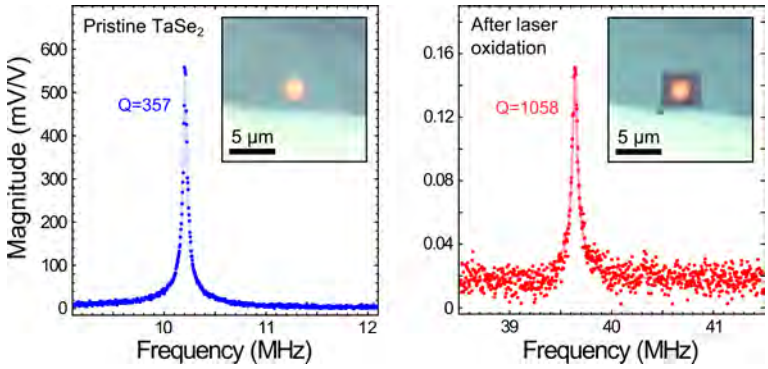

Figure 2.9: Mechanical resonances of $TaSe_2$ flakes before and after laser-oxidation. (a) Fundamental mechanical resonance peak of a pristine 3.2 μm diameter drum with a thickness of 17 nm. Inset: Optical image of the drum. (b) Fundamental resonance peak of the same drum after laser-oxidation of the square region shown in the inset. A large enhancement of the resonance frequency and Q factor is observed.

Figure 2.9 shows the mechanical resonance spectrum of a 17 nm thick $TaSe_2$ drumhead resonator vibrating in its fundamental mode before and after laser-oxidation. The insets show the corresponding optical images of the device, and the square-shaped laser-exposed area containing the suspended drumhead in the oxidized case. The resonance frequency increases from $f_{pris} = 10.2$ MHz to $f_{ox} = 39.6$ MHz after oxidation, where f_{pris} and f_{ox} are the fundamental frequencies for the pristine and oxidized cases, respectively. At the same time,

the Q factor rises from $Q_{pris} = 357$ to $Q_{ox} = 1058$. A driven harmonic oscillator model fits the data and is used to determine the Q factor (solid lines). The magnitude of the interferometer signal after oxidation is a factor 3700 smaller than the signal before oxidation. This is attributed to a reduction of the photothermal actuation efficiency by a diminished optical absorption and to a reduction of the interferometric signal by reduction of the drum's reflectance after oxidation. After having demonstrated a controlled enhancement of f_0 and Q, we proceed to perform a systematic study on devices of different thickness.

Figure 2.10 shows the resonance frequencies and Q factors of 3.2 μm-in-diameter drums with thicknesses ranging from 6 to 89 nm, all from the same flake to ensure that they have the same built-in pre-stress, before (blue squares) and after laser-oxidation (red circles). Starting with the pristine drums (blue data), we observe for thick devices a linear relation between resonance frequency and thickness because the bending rigidity dominates the mechanics of the resonator (dashed lines represent this plate-like mechanical behavior). In the limit of small thickness, the resonance frequency converges to a constant value because the pre-stress dominates the mechanics (dotted lines represent this membrane limit). In the oxidized drums (red circles in Figure 2.10(a)), the resonance frequency behavior in the plate limit is similar to that of the pristine devices. However, the thin oxidized drums show a much higher resonance frequency in the membrane limit, which indicates a larger pre-stress.

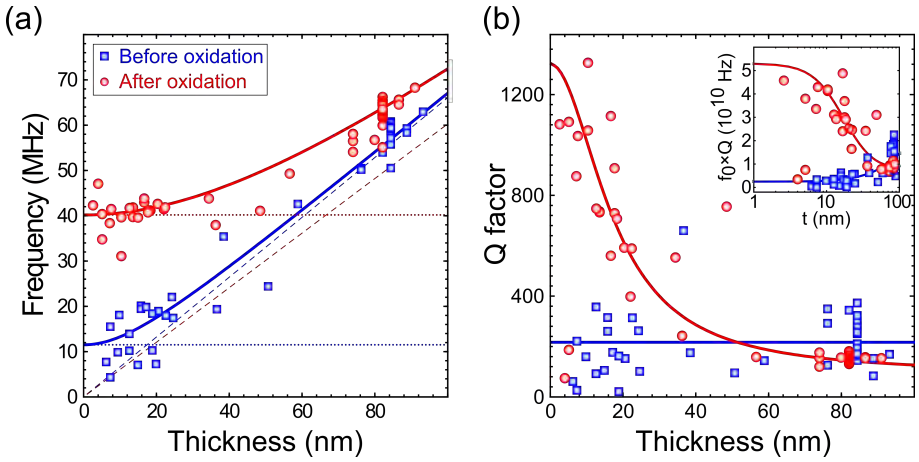

Figure 2.10: Thickness dependence of f_0 and Q of several drum resonators before and after laser-oxidation. (a) Resonance frequency versus thickness of drums with a diameter of 3.2 μm from the same $TaSe_2$ flake before (blue squares) and after oxidation (red circles). Equation 2.2 (solid lines) is used to fit the data. For small thickness the resonance frequency follows the membrane limit (horizontal dotted lines, Equation 2.1), whereas for thick drums the data converges toward the plate limit (dashed lines, Equation 2.1). (b) Q factor versus thickness: for thin drums an increase in Q is observed after laser-oxidation. Solid red lines correspond to fits to the data by Equation 2.3. Inset: In thin drums, laser-oxidation increases the f-Q product.

2.4.1. OXIDATION-INDUCED STRESS

To extract the stress increase caused by laser-oxidation, we modeled the resonance frequency of the drums as follows. For thin drums, the fundamental resonance frequency of the drums converges to the membrane limit f_{mem}, whereas for thick drums the frequency converges to the plate limit f_{plate} [137]:

$$f_{mem} = \frac{2.40}{\pi d}\sqrt{\frac{\sigma}{\rho}} \qquad f_{plate} = \frac{10.21}{\pi}\sqrt{\frac{E}{3\rho(1-\nu^2)}}\, t/d^2, \tag{2.1}$$

where E is Young's modulus, $\nu \approx 0.2$ is the Poisson's ratio [138], ρ is the mass density (ρ_{pris} = 8660 kg/m^3, $\rho_{ox} = 0.655\rho_{pris}$ [133]), t is the thickness, d is the resonator diameter, and σ is the pre-stress in the drumhead. For drums of intermediate thickness, the resonance frequency can be approximated by addition of the spring constants of plate and membrane modes giving:

$$f_0 \approx \sqrt{f_{mem}^2 + f_{plate}^2}. \tag{2.2}$$

A fit of Equation 2.2 to the data in Figure 2.10a (solid lines) gives an estimate of the Young's modulus (E_{pris} = 110 GPa and E_{ox} = 60 GPa) and of the stress (σ_{pris} = 20 MPa and σ_{ox} = 160 MPa) values before and after oxidation. The estimated Young's modulus for $TaSe_2$ is in good agreement with values found in literature [139, 140, 141, 142, 143, 144]. Since the crystal structure of the oxidized flake consists of a mixture of amorphous and crystalline regions it is not possible to make a comparison between the Young's modulus of the oxidized flake and the data available in the literature. The fit shows a large increase of the tensile stress in the membrane from 20 MPa to 160 MPa. The drastic increase in the resonance frequency during oxidation of the thin $TaSe_2$ drums can be mainly attributed to the increase in tensile stress.

Having established clearly the presence of oxidization-induced stress, we now address a possible mechanism for how this stress is created. The laser-oxidation occurs locally and only heats up the material without significantly affecting the substrate beneath. During the recrystallization of the oxide at high temperature T_{ox} = 600°C, atoms rearrange, which leads to stress relaxation in the suspended part of the drum. While cooling down, thermal contraction of the drum increases the stress in the membrane. An estimated value of the resulting tensile stress, using the coefficient of thermal expansion $\alpha_{ox} = 3.6\ 10^{-6}$ K^{-1} of Ta_2O_5 [145] yields $\sigma_{ox,e} \approx (T_{ox} - 25°\text{C})\alpha_{ox}E_{ox}$ = 120 MPa, in agreement with the measured stress σ_{ox} = 160 MPa.

In addition to changing the frequency of the mechanical resonators, the oxidization process also significantly changes the mechanical quality factor. Figure 2.10b shows the thickness dependence of the quality factor of the fundamental resonance before and after laser-oxidation. We find that the quality factor in pristine $TaSe_2$ resonators (blue squares) is almost independent of the thickness. For laser-oxidized drums on the other hand, the quality factor shows a strong thickness dependence: in thin oxidized drums the quality factor is up to a factor 9.4 higher than that in thick oxidized drums.

In the following, we show that the increase of the Q factor originates from the large tensile stress of the thin oxidized drums. A similar increase in Q factor in highly stressed thin membranes has been observed in Si_3N_4 resonators and reduced graphene oxide [119, 123, 124, 146, 147, 148, 149]. The almost thickness-independent Q factor in low-stress (plate-like) drums observed in the pristine material can be phenomenologically described [123, 124] using a material model with a frequency-independent complex Young's modulus $E = E_1 + iE_2$. The imaginary part of the Young's modulus causes dissipation. Since the bending rigidity is proportional to the Young's modulus, the complex plate spring constant will be given by $k_{plate} = k_{plate,1} + i\,k_{plate,2}$. The resonator's Q-factor in the plate limit will therefore be given by $Q_{plate} = \frac{E_1}{E_2} = \frac{k_{plate,1}}{k_{plate,2}}$. Similarly, in the membrane limit the Q factor can be expressed as $Q_{mem} = \frac{k_{mem,1}}{k_{mem,2}}$, however since the losses due to elongation are much lower than the losses due to bending we will assume that $Q_{mem} >> Q_{plate}$ and $k_{mem,2} \approx 0$.

By adding the bending and membrane spring constants (as in Equation 2.2), the stress dependence of the Q factor is therefore given by $Q = \frac{k_{mem,1}+k_{plate,1}}{k_{plate,2}}$. This relation shows that a stress-induced increase of $k_{mem,1}$, will result in an increase of the resonator's Q factor. Based on this relation an equation for the Q-ratio between pristine and oxidized drums is derived. In the presence of tensile stress, the real part of the spring constant will increase to a value $k_1 = k_{mem,1} + k_{plate,1}$ and the resonance frequency f_0 will become $f^2 = \frac{k_1}{m} = f_{plate}^2 + f_{mem}^2$. Then, the Q factor will become $Q = Q_{plate}\frac{f^2}{f_{plate}^2}$.

Based on the equations above and using $\frac{k_{plate,1,ox}}{k_{plate,1,pris}} = \frac{E_{1,ox}}{E_{1,pris}}$, it is now straightforward to derive the ratio of the Q factors of the oxidized and pristine drums:

$$\frac{Q_{ox}}{Q_{pris}} = \frac{f_{ox}^2}{f_{pris}^2}\frac{f_{plate,pris}^2}{f_{plate,ox}^2}\frac{E_{1,ox}}{E_{1,pris}}\frac{E_{2,pris}}{E_{2,ox}} = \alpha\left(\frac{f_{ox}}{f_{pris}}\right)^2, \tag{2.3}$$

where $\alpha = \frac{m_{ox}}{m_{pris}}\frac{E_{2,pris}}{E_{2,ox}}$ and m is the mass of the drumhead. Equation 2.3 is used to fit the thickness-dependence of Q_{ox} in Figure 2.10b (solid lines). The values of f_{pris} and f_{ox} determined from the fits in Figure 2.10a and an average value $Q_{pris} = 216$ are used. By adjusting the coefficient $\alpha = 0.5$ as the only fit parameter, the thickness dependence of Q_{ox} is well captured by Equation 2.3. The model based on a frequency-independent complex Young's modulus, that was proposed to model the Q-factor increase with stress in Si_3N_4 beams [118, 124, 148, 150], is thus observed to be consistent with the thickness dependence of the Q-factor in oxidized $TaSe_2$ flakes (Equation 2.3).

2.4.2. LOCAL OXIDATION OF RESONATORS

The laser-oxidation technique is unique because it allows local oxidation of selected devices in contrast to other oxidation techniques that modify all oxygen-exposed material. In Figure 2.11 we show the potential of the laser-oxidation technique for fabricating write-once-read-many (WORM) memory devices, where information is encoded in the resonance fre-

quency of the Ta-based resonators.

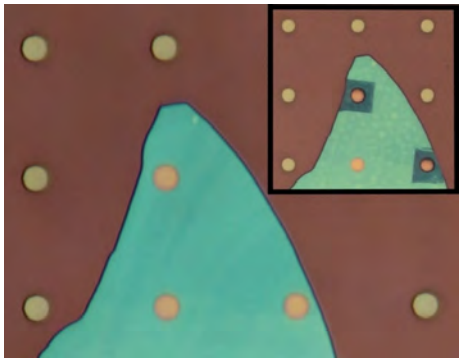

Figure 2.11: Blank Ta-based mechanical memory (drums of 3.2 μm in diameter). Inset: The laser oxidation technique is used to program the memory by writing bits. An interferometer can read the memory, giving a 1 or 0 depending on the measured resonance frequency of the drums.

2.5. CONCLUSIONS

The *f*-*Q* product is an important figure of merit for micro and nanoresonators, because high *f*-*Q* products can yield low phase-noise high frequency oscillators and sensors. Since tensile stress has been shown to increase both resonance frequency and *Q* factor, the presented laser oxidation procedure is a very effective method to increase the *f*-*Q* product as is shown in the inset of Figure 2.10b. The increase is as high as a factor 42 yielding a maximum *f*-*Q* product of 4.9 10^{10} Hz. To our knowledge the presented laser-oxidation method yields the highest *f*-*Q* product at room temperature in ultrathin resonators ($t < 20$ nm) made out of 2D materials, outperforming *f*-*Q* products reported in graphene and MoS_2 devices at room temperature [151].

In summary, a laser-oxidation procedure for enhancement of quality factor and resonance frequency of multilayer $TaSe_2$ resonators is demonstrated. The procedure increases the stress in the drums by a factor 8, due to thermal contraction during cooldown after laser-oxidation. The stress results in an enhanced resonance frequency (up to 9 times larger) and *Q* factor (over 14 times larger), which is attributed to a stress-induced increase in spring constant. The presented laser oxidation procedure thus provides a tool to locally and selectively modify the mechanical properties of 2D materials. This enables interesting applications, such as in-situ tuning of the resonance frequency and the *Q* factor, and, by the selective patterning of stress regions in suspended flakes, engineering the mechanical mode shapes and intermode relations. The same procedure is expected to be applicable in other 2D materials, as many metal dichalcogenides show oxidation reactions similar to $TaSe_2$ [133, 152].

Application 2: CVD graphene and h-BN for optomechanic sensing

3

LASER-INDUCED TENSIONING OF CVD DOUBLE-LAYER GRAPHENE DRUMHEAD RESONATORS

El signo de la vitalidad no es durar, sino renacer y adaptarse.
("The sign of vitality is not to last, but to be reborn and adapt.")

José María Arizmendiarrieta

If it's not fun, it's not worth it.

Santiago (in allusion to *The Virgin Way* by Richard Branson), Delft 2017

Stacking several layers of chemical-vapor-deposited (CVD) graphene have proved to be a promising route to improve the impermeability of graphene membranes for its use in hermetic pressure sensors. Here, we use a laser interferometry technique to characterize CVD double-layer (DLG) drumheads of different diameters to find that the material is as clean as exfoliated graphene, thus paving the way to its commercialization. Moreover, we analyze the heating effects from the laser on the resonance frequency and quality factor (Q) of these membranes, and introduce a new model that can explain Q as a function of thermally-induced variation of the sidewall length. This hypothesis predicts Q to be linearly dependent on the tension and diameter which we find experimentally, and should be inversely linear to the sidewall length variation and inversely quadratic to thickness as long as the material behaves like a membrane.

3.1. INTRODUCTION

Graphene, a single-atom layer of graphite, is going to revolutionize technology with its unique optical, electrical and mechanical properties. Its thinness and high tensile strength [114, 115] makes graphene suitable as material for MEMS, promising very sensitive devices due to the large tuneability when exposed to environmental changes. By exploiting the gas impermeability of graphene [52], one of the potential applications of graphene MEMS is pressure sensing: a cavity sealed with a graphene membrane would deform upon the application of pressure difference. However, such a sensor is required to be hermetically sealed so the cavity pressure can be used as reference during the device lifetime.

When it comes to commercialize graphene sensors, however, the impermeability property is hard to replicate as chemical vapor deposited (CVD) single-layer graphene (SLG) is usually produced with defects despite being the most promising route for scaling [116]. Stacking several layers improves the hermeticity of these devices [117, 153], hence offering a new route to bypass that problem. CVD double-layer graphene (DLG) has been proven to be a platform to study new phenomena with an optical microscope thanks to the larger absorption of light, which gives a greater contrast under certain conditions [154].

Laser interferometry has been used previously to study the dynamic behavior of SLG in the frequency domain, and it helped to characterize the mechanical properties of the material [105, 108, 111], study its impermeability [52] and other properties like self-oscillations [100, 155]. Although it is not a scalable characterization tool like a multiwavelength analysis with an optical microscope (colorimetry technique) [153, 154], it offers the option of contactless measurements in the MHz range unlike other techniques such as AFM nanoindentation.

Despite the non-contact nature of optical probing, laser measurements can be invasive as light absorption is transformed into heat, which increases temperature and can cause misinterpretations of the data. Hence, the performance of small devices can be largely influenced by a relatively small laser power flux. Particularly, graphene membranes suspended on cavities have been reported to be influenced by a photon-induced rigidity in laser interference measurements [155] and by photothermal straining in Raman spectroscopy [156].

Here, we report the characterization of CVD double-layer graphene devices by studying their resonance frequency and quality factor with a laser interferometry setup. We compare the extracted tensions to the values from AFM indentation to conclude that the DLG material has a mass density close to that of pristine bilayer graphene, hence proving to be very clean. Moreover, we show a mechanical softening effect followed by tensioning of a membrane when increasing the laser power, that we explain by sidewall delamination induced by heating. Based on this concept, we propose a model for 2D membranes that relates the quality factor to their cyclic tensioning and softening caused by the laser modulation, therefore predicting its dependence on the device diameter.

3.2. FABRICATION AND SETUP

Device cavities are fabricated by reactive-ion etching circular holes of different diameters through a thermally-grown 570 nm-thick SiO_2 layer on a silicon substrate. A DLG layer,

made out of two SLG CVD graphene layers previously piled up, is transferred onto the patterned substrate using a semi-dry transfer technique, thus resulting in suspended CVD DLG drums. In this work, we use DLG membranes due to their higher yield in larger diameters [154] and because their absorption in the visible spectrum of light is at least twice that of SLG, thus absorbing double amount of laser powers.

Figure 3.1a shows an optical microscope image of the large array of drums with diameters ranging from 3 to 20 μm. Device by device, the interference of a red laser (continuous wave with wavelength λ = 632 nm) is detected as a function of actuation frequency produced by a modulated diode laser.

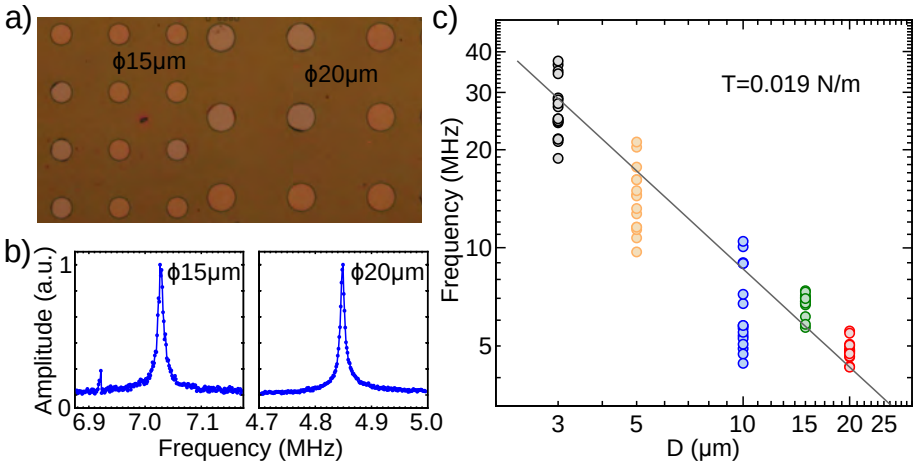

Figure 3.1: CVD double-layer graphene mechanical resonators. a) Optical microscope image showing drumhead membranes of 15 and 20 μm in diameter suspended on circular cavities of 570 nm in depth patterned on SiO_2/Si. b) Mechanical resonance peak of two of the membranes of 15 (left) and 20 μm in diameter (right). As expected from Equation 3.1, a larger diameter reduces the fundamental resonance frequency. c) Fundamental resonance frequency as a function of diameter D. 15 devices are measured for each diameter to study the variation in their mechanical properties. All measurements were performed with a power of 13.3 mW of the detection beam from the laser interferometer.

The dynamical behavior of suspended DLG is dominated by tension N, and their fundamental resonance frequency f depends on the diameter D following the theory for circular membranes [157]:

$$f = \frac{1}{2\pi}\sqrt{\frac{k}{m}} = \frac{2.4}{\pi D}\sqrt{\frac{N}{\rho t}}, \tag{3.1}$$

where m and $k = \pi N$ are the mass and spring constant of the membrane, respectively, with $\rho = 2100$ kg/m^3 the mass density of graphite, and $t = 0.67$ nm the theoretical DLG thickness. This inversely linear relation between resonance frequency and diameter is found experimentally, as shown in Figure 3.1b. For each diameter, 15 drums were measured at a fixed

laser power of 13.3 mW (spot size of ~1μ in diameter).

By using Equation 3.1, the tension N is extracted and plotted against their diameter in Figure 3.2 (top panel). The spread of tensions is caused possibly by membrane imperfections (wrinkles, defects or small holes) or more likely by variations of mass (polymer contamination or adhered hydrocarbon molecules). The standard deviation of the tension for each drum size is shown in the bottom panel. We note an abrupt reduction in the standard deviation at higher diameters that can be explained by the selective destruction of low-tensioned devices when a pressure difference is applied [154].

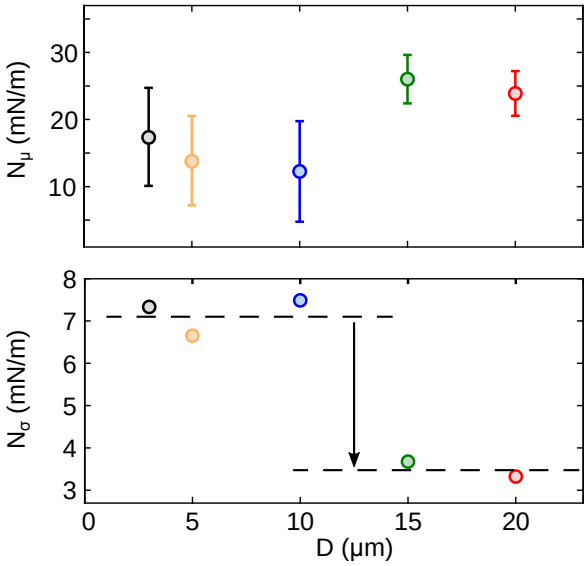

Figure 3.2: Variation of the tension N as a function of diameter. The tension values are extracted from the resonance frequency by using Equation 3.1. For a given diameter, we obtain the average (top panel) and standard deviation (bottom panel) values. The tension seems to be independent of the diameter, although the trends show a step between 10 and 15 μm possibly caused by a selective destruction of low-tensioned devices due to pressure changes [154].

Figure 3.3 displays the corresponding quality factors Q of the same drumheads, together with its standard deviation as a function of diameter. The quality factor is calculated as $Q = \frac{f}{\Delta f}$ and accounts for the ratio between dissipated and stored energy per cycle. The relation between Q and diameter has been studied in SiN and SLG membranes although it was not well understood [105, 111, 118, 119, 124, 148]. However, we describe below a hypothesis that predicts a linear function ($Q \propto D$).

To understand the influence of laser-induced heating on the resonance frequency, we performed a power study of the red laser. The laser power P was increased from 0.1 mW to 13.3 mW by placing different neutral density filters in the beam path (Thorlabs FW212CNEB). Figure 3.4a shows the frequency of a 5 μm in diameter DLG circular resonator as a function

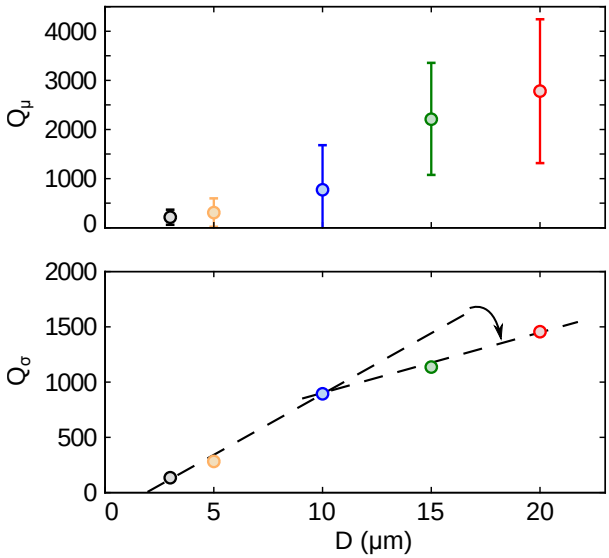

Figure 3.3: Dependence of the quality factor Q with the diameter. The average values (top panel) shows a linear relation as reported previously. The standard deviation (bottom panel) also increases linearly although it seems that the same mechanism as in Figure 3.2 affected the trend around 10 μm in diameter.

of laser power. The frequency decreases when increasing the heating at low powers until it reaches a minimum. Then, the drum begins to tension up linearly with the power with a slope of 0.078 MHz/mW ($4 \cdot 10^{-7}$ N/(m·mW)).

In Figure 3.4b, the inverse of Q is plotted against the red laser power. The linear relation can be used to extrapolate the experimental data to find the intrinsic quality factor, Q_{int}, which for this membrane is 83. In this particular device, the quality factor tends to infinity when the power is higher than 6 mW, thus becoming a self-oscillator. In contrast to externally-driven resonators, a self-oscillator does not require the modulated actuation signal from the blue laser to oscillate.

3.3. DISCUSSION

Self-oscillations in graphene drumheads have been studied previously and were found to be moving by heat-induced jiggling around the spatial inflexion point of a photothermal gradient (optomechanical back-action or feedback) [155]. The interference of the laser beam with its reflection from the mirror-like bottom of the cavity creates spacial regions of variable intensity and, depending on the position of the membrane inside that cavity, the suspended material absorbs different amount of light (statically). At the same time, the movement of the membrane across the static intensity gradients causes a photothermal force that damps or amplifies its movement. Thus, the tensioning and increase of Q of the membrane in Fig-

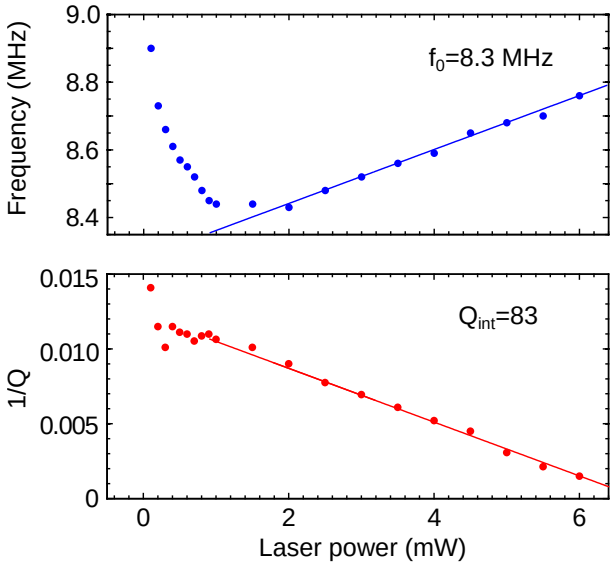

Figure 3.4: Influence of the laser power on the resonance frequency and quality factor of a drum of 5 μm in diameter. Top panel: The resonance frequency goes through two regimes when increasing the laser power: first it decreases until a minimum point before becoming linearly dependent on power. Therefore, there is a softening mechanism at low powers that is overcome by the known thermal tensioning. According to Equation 3.2, a laser-induced heating of a 2D material with negative expansion coefficient like graphene could cause the contraction of the membrane, resulting on a delamination from the sidewalls at first (without variation of tension, but gaining mass density), followed by an in-plane compression once the material is clamped only from the edges. By extrapolating the thermo-elastic regime, we obtain an ideal fundamental mode f_0 of 8.3 MHz (pre-tension of 6-9 mN/m). Bottom panel: The inverse of the quality factor decreases linearly with the laser power. By extrapolating the data to zero-power, we obtain an intrinsic quality factor of 83. According to Equation 3.3, a membrane of 5 μm in diameter with $N = 0.019$ N/m would have a quality factor in the sidewall-adhesion regime of 97 for a variation of the sidewall length of 1 nm. Beyond 6 mW, this particular drum becomes a self-oscillator due to the photothermal effect discussed in [155].

ure 3.4a at higher laser powers (before the condition of self-oscillations is satisfied) could be explained by means of photothermal feedback with the right conditions. However, this model cannot explain the static decrease of tension (softening) when increasing the power at low laser powers.

Similarly to the complete version of the photon-induced rigidity model, we can expand Equation 3.1 to assume that N depends on the temperature to describe the change of static tension induced by laser absorption. Here, we introduce a temperature-dependent sidewall length that balances the sidewall adhesion energy and the elastic energy of the membrane as reported in h-BN resonators [158]. For the particular case of a 2D material with negative expansion coefficient such as graphene, Equation 3.1 is modified to include the temperature-induced tensioning of the membrane due to its adhesion to the sidewalls of the cavity when

expanding:

$$f(T) = \frac{2.4}{\pi D}\sqrt{\frac{N + N_{sidewall}(T)}{\rho t}} = \frac{2.4}{\pi D}\sqrt{\frac{N_T}{\rho t}}, \tag{3.2}$$

where $N_{sidewall}(T) = Et\frac{24tL(T)}{D^2}$, with $E = 1$ TPa being the Young's modulus of graphene and $L(T)$, the sidewall length proportional to the expansion coefficient of graphene in the basal plane α. $N_{sidewall}$ is the tension contribution from the adhesion force that a suspended membrane suffers when it sticks to the sidewalls of its circular cavity. This mechanism depends on the variation of temperature $\Delta T = T - 300$ K as the membrane would expand laterally towards the bottom of the cavity when cooled, or delaminate from the sidewall when warmed up (the diameter remains always constant). By considering the biaxial in-plane strain originated from the variation of mass a) delivered to the sidewall when the membrane expands or b) removed back to the suspended structure when the graphene contracts, we find that $L(T) = \frac{D}{4}\alpha\Delta T$ [159].

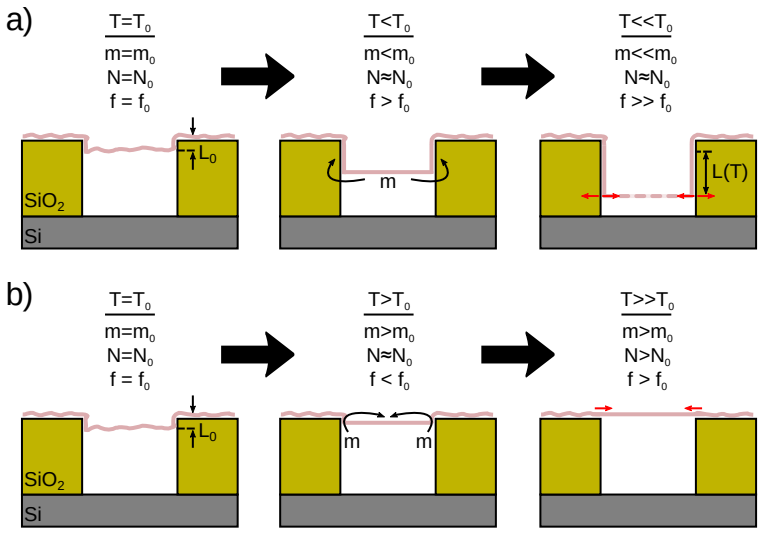

Figure 3.5: Behavior of a 2D membrane of negative expansion coefficient with an initial sidewall length L_0 when changing its temperature. a) When cooling down, a fully-clamped suspended graphene tends to expand by sending part of the freestanding mass to the sidewalls of the cavity, hence resulting in an increase of the sidewall length $L(T)$. Without assuming a particular model, we would expect a self-balancing of adhesion-separation forces at the edges of the membrane that may not change much its tension, while the loss of suspended mass would induce an increase of its resonance frequency. b) On the other hand, if the suspended membrane is heated, the suspended material will compress by retracting part of the adhered mass in the sidewalls of the cavity (delamination), hence resulting in a decrease of $L(T)$. This action would initially enlarge the suspended mass (decreasing the resonance frequency) until the membrane reaches the edge of the cavity and starts tensioning.

Figure 3.5 illustrates the behavior of a graphene membrane when a) decreasing and b) increasing its temperature. According to Equation 3.2, a laser-induced heating of the neg-

ative expansion graphene will cause the membrane contract resulting on a delamination from the sidewalls at first (without variation of tension, but gaining mass density), followed by an in-plane compression once the material is clamped only from the edges. This two regimes, the sidewall-adhesion dominated and the fully-clamped state, are visible in Figure 3.4.

The same model can be applied to understand the quality factor. For that, we consider a time-varying heating induced by laser absorption (either due to the membrane crossing different regions of the interfered red laser or due to the modulation of the blue laser) and we assume that the heat transfer and conduction through the membrane is effective. Then, the variation of tension is $\Delta N(T) = N_{sidewall}(T)$ and we could redefine the quality factor as function of temperature-dependent tension modulation:

$$Q(T) = \frac{f}{\Delta f} = \frac{2N_T}{\Delta N(T)} = \frac{N_T D^2}{12Et^2\Delta L(T)} = \frac{N_T D}{3Et^2\alpha\Delta T}. \tag{3.3}$$

According to Equation 3.3, a variation of the sidewall length of 1 nm would cause a membrane of 5 μm in diameter and $N_T = 0.019$ N/m to have a $Q \sim 97$, similar to the value found in Figure 3.4b on the sidewall-adhesion regime.This unpredicted relation between quality factor sidewall length comes naturally by considering the recent finding about the difference between adhesion energy and delamination energy in graphene bubbles [160]. The quality factor should originate from the dissipated energy between a cycle of adhesion/delamination (tensioning/softening) caused by the laser heating.

Equation 3.3 thus predicts a linear relation between quality factor and the product of tension and diameter ($Q \sim ND$) or, equivalently, $Q \sim f^2D^3$. Figure 3.6 displays the experimental data showing such a trend. From fitting the data, we extract a temperature variation of 35 K if the material was pristine ($E = 1$ TPa) or more likely a $\Delta T = 3.5$ K for $E = 100$ GPa typical for CVD graphene.

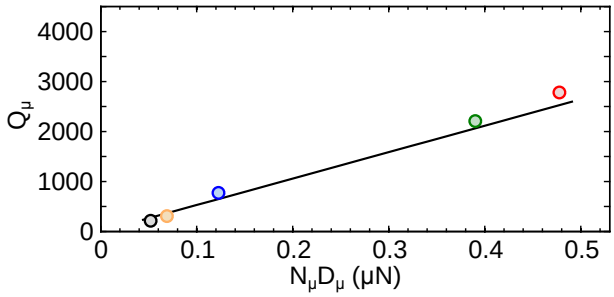

Figure 3.6: Dependence of the quality factor Q as a funtion of ND ($\sim f^2D^3$). The relations of Q according to Equation 3.3 appear to be describe the data trend. The fits correspond to $\Delta T = 35$ K for a $E = 1$ TPa or $\Delta T = 3.5$ K for a $E = 100$ GPa.

	Laser power 13.3 mW		Laser power 1 mW (extrapolated)		AFM $F_{PFM} = 5$ nN
Device	f (MHz)	N (10^{-3} N/m)	f (MHz)	N (10^{-3} N/m)	N (10^{-3} N/m)
1	24.87	14	23.91	13	28
2	21.19	10	20.23	9	25
3	28.82	19	27.86	18	38
4	18.81	8	17.85	7	16
5	24.19	13	23.22	12	34
6	27.08	17	26.12	15	15
7	28.43	18	27.46	17	14
8	24.40	13	23.44	12	19
9	36.44	30	35.47	28	32
10	21.60	11	20.64	10	19
11	27.71	17	26.75	16	30
12	24.53	14	23.57	13	22
13	37.43	32	36.46	30	32
14	34.86	28	33.90	26	25
15	34.21	26	33.25	25	42

Table 3.1: Comparison of tensions of CVD DLG drums of 3 μm in diameter measured with a laser interferometer and an AFM. Their fundamental frequency is used to indirectly obtain the tension from the laser interferometric technique (assuming an ideal mass of DLG). The extrapolated tension at low powers can be compared to that directly measured by AFM nanoindentation performed at the center of the drums, yielding a difference that we attribute to additional mass (about $0.4(\rho t)_{DLG}$). This possible contamination is comparable to that in pristine SLG [52, 56].

Since now we have a reliable way to compensate for the heating induced by the measurement system, we can also quantify the amount of contamination present in the material. It is well known that the cleaning of graphene -specially when freestanding- is one of the biggest challenges for its commercialization up to date. Despite the cleaning processes during fabrication, some polymer residue layer in the order of a nanometer might remain. To test this hypothesis, we performed nanoindentations at the center of CVD DLG drums of 3 μm in diameter and compared the directly measured tensions to the corresponding values of the same devices extracted from laser interferometry [158]. Since the laser-induced heating influences the tension, we use the linear dependence of resonance frequency with laser power to estimate the tension at 1 mW (extrapolated from the slope in Figure 3.4a). Table 3.1 collects all the values from which we obtain an averaged tension difference between AFM and laser interferometry of 1.4. As the AFM values are not influenced by mass, we can attribute this factor to the extra mass that the devices have in average (about $0.4(\rho t)_{DLG}$), possibly being polymer contamination. Therefore, we can conclude that these devices are as clean as the cleanest pristine graphene reported so far [52, 56].

3.4. CONCLUSIONS

This work has presented the mechanical characterization of CVD double-layer graphene resonators with a laser interferometry technique. A statistical study of their resonance frequency and quality factor as a function of their diameter was performed, and we explored the influence of the laser power. We revisited the model of circular membranes to include the effect of laser heating to the tensioning of the drumheads, and propose a sidewall delamination/adhesion mechanism to explain the quality factor. According to this theory, the quality factor should have a linear relation with the membrane diameter as experimentally observed, while depending quadratically with thickness and inversely linearly to the sidewall length. Moreover, we compared the tensions obtained from laser interferometry to those measured by AFM nanoindentation to conclude that the membranes have minimal contamination.

4

MECHANICAL CHARACTERIZATION AND CLEANING OF CVD SL h-BN RESONATORS

俺は海賊王になる!! *(Ore wa kaizoku-ou ni naru!!)*

Monkey D. Luffy in *One Piece*, by Eiichiro Oda

純粋な子供と侍の心 *(Junsuina kodomo to samurai no kokoro)*

Santiago, San Diego 2010

Hexagonal boron nitride (h-BN) is a 2D material whose single-layer allotrope has not been intensively studied despite being the substrate for graphene electronics. Its transparency and stronger interlayer adhesion with respect to graphene makes it difficult to work with, while applications exploiting the intrinsic properties of h-BN are scarce. We have developed a transfer technique for this adhesive material that does not require its visual localization, and fabricated mechanical resonators made out of chemical vapor deposited (CVD) single-layer h-BN. The suspended material was initially contaminated with polymer residues from the transfer, and the devices showed an unexpected tensioning when cooling them to 3 K. After cleaning in harsh environments with air at 450° C and ozone, the temperature dependence changed with f_0Q products reaching $2 \cdot 10^{10}$ Hz at room temperature. This work paves the way to the realization of highly sensitive mechanical systems based on h-BN, which could be used as an alternative material to Si_3N_4 for optomechanics experiments at room temperature.

Parts of this chapter have been published in npj 2D Materials and Applications **1**, 16 (2017) by S.J. Cartamil-Bueno, M. Cavalieri, R. Hwang, S. Houri, S. Hofmann, and H.S.J. van der Zant.

4.1. INTRODUCTION

Fabrication of suspended h-BN devices has been limited to few-layers [161, 162, 163]. Mechanical devices made out of 2D materials are often fabricated with a polymer-assisted transfer technique that requires a wet release of the suspended system [71, 75, 96], or a dry method that exploits the viscoelastic properties of polydimethylsiloxane (PDMS) [125, 164]. In the case of drum devices where the membrane seals a cavity of a few hundreds of nanometers in depth, a dry transfer is more convenient as surface forces caused by liquid menisci upon drying tend to break the structure or push it to the bottom of the cavity resulting in collapsed devices.

In this chapter, we report the fabrication and characterization of the first mechanical resonators made out of chemical vapor deposited (CVD) single-layer h-BN. The fabrication includes a novel transfer technique suitable for adhesive 2D materials and highly efficient cleaning process for h-BN resonators. Due to the transfer process, the single-layer h-BN devices were covered with polymer contamination and showed an unexpected tensioning when cooling them to 3 K. After cleaning processes in harsh environments, the temperature dependence of their mechanical behavior changed, and their figure of merit (f_0Q product) improved by a factor of 30 up to 2×10^{10} Hz at room temperature.

4.2. FABRICATION AND SETUP

Figure 4.1 shows the fabrication process of suspended h-BN devices. A continuous layer of CVD h-BN is grown on iron foils and characterized by transmission electron microscopy (TEM) to be single layer as previously reported [84]. Due to the stronger adhesion of h-BN to surfaces, it has to be transported from the growth substrate to the final substrate by using sacrificial layers. Poly(methyl methacrylate) (PMMA) is spin coated on top of the h-BN, and the stack is delaminated with the bubbling technique [165]: a voltage of 3 V is applied between the Fe/h-BN/PMMA stack (cathode) and a Pt wire (anode) of an electrochemical cell with 1 M NaOH (electrolyte). From scanning electron microscopy (SEM) images taken before the delamination, the grain size is estimated to be around 20 μm. The h-BN/PMMA stack is then transferred onto a piece of silicon covered with 300 nm of Poly(vinyl alcohol) (PVA), and the PMMA is removed by an acetone bath, resulting in a Si/PVA/h-BN structure.

Using this sandwiched structure, we developed a dry transfer technique that is a hybrid of the methods described in references [71, 125] especially designed for the transfer of CVD h-BN to make sealed cavities. Figure 4.1a (steps vi-xii) describes the dry transfer process. A piece of PDMS (GelPack x8 PF film) is placed on top of the Si/PVA/h-BN, and the stack is left floating in deionized water. The water dissolves the PVA layer slowly until the h-BN/PDMS detaches from the silicon substrate which sinks. The floating h-BN/PDMS is picked up with tweezers and dried with nitrogen, and then placed on a clean microscope slide. From this point, we continue with the technique from reference [125]: the h-BN is dry transferred deterministically by using the viscoelastic properties of PDMS on top of the target substrate. A silicon substrate with 300 nm of thermally-grown SiO_2 is patterned via e-beam lithography and reactive ion etching to make circular cavities of different diameters on the oxide layer

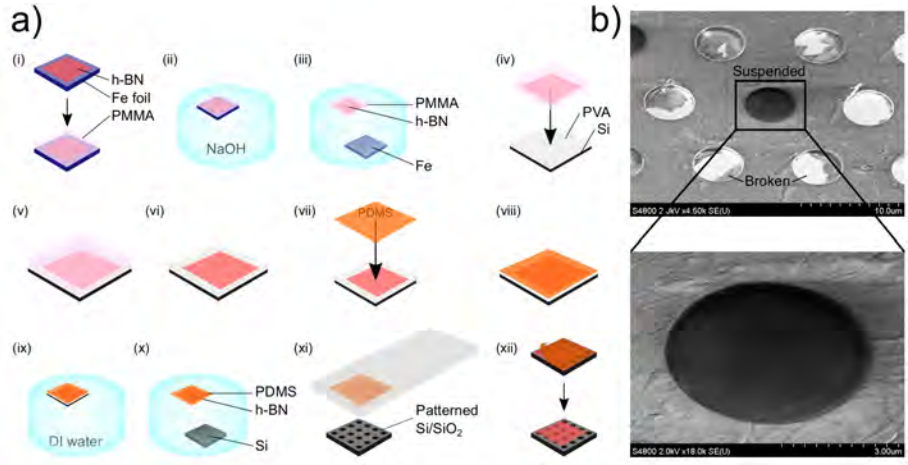

Figure 4.1: CVD single-layer h-BN growth and dry transfer. (a) Large-area single-layer h-BN is grown by chemical vapor deposition (CVD) on Fe foils, and it is coated with PMMA (i). Then, the h-BN/PMMA stack is delaminated from the foil by means of bubbling [84] (ii-iii). The h-BN is transferred to a Si/PVA substrate, and the PMMA is removed with acetone (iv-vi). PDMS is placed on the Si/PVA/h-BN (viii), and the structure is left floating on DI water (ix). When the Si substrate detaches from the layer stack (x), the h-BN/PDMS is picked and dried. From this point, the usual viscoelastic dry transfer technique [125] is used to transfer the CVD single-layer h-BN on patterned substrates (xi-xii). (b) Scanning electron microscope image of CVD single-layer h-BN covering circular cavities of 5 μm in diameter (top panel). Since h-BN is an insulator, electrons are trapped in the suspended material and appear with high contrast. A flat drum with a few wrinkles is shown in the bottom panel.

(fully etched through to the silicon). By using the developed transfer technique, we cover the cavities with CVD single-layer h-BN resulting in drums as shown in Figure 4.1b. Some of these suspended membranes have small perforations, wrinkles and polymer contamination as can be seen in the Atomic Force Microscopy (Figure 4.2) and Scanning Electron Microscopy (Figure 4.3) before the cleaning processes.

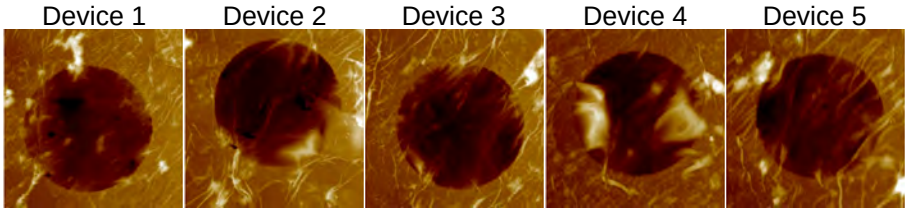

Figure 4.2: AFM images of single-layer h-BN mechanical devices before cleaning. Devices are 5 μm in diameter.

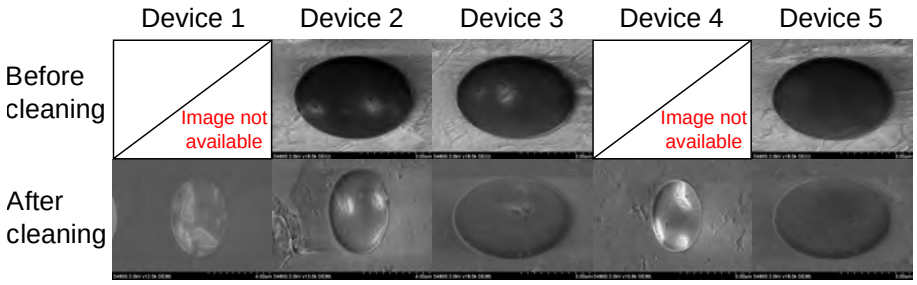

Figure 4.3: SEM images of single-layer h-BN mechanical devices of 5 μm in diameter before and after cleaning in harsh environments.

4.3. MATERIAL CHARACTERIZATION OF CVD SL H-BN BEFORE/ AFTER CLEANING

4.3.1. VIBRATION AND PHOTOLUMINESCENCE BY RAMAN SPECTROSCOPY

Figure 4.4a shows the Raman spectrum with the characteristic peak around 1370 cm^{-1} [76, 166], which supports the TEM characterization on its single-layer nature. Raman spectroscopy on the h-BN material over Si/SiO_2 was carried out with a Renishaw in Via Raman microscope. Measurements with a laser light of 514 nm were performed on supported areas. The backscattered light was collected with a 100× objective (NA = 0.95) and recorded with a 1800 lines/mm grating, which gives a spectral resolution of 1.75 cm^{-1}. The laser power was about 25 mW. Figure 4.5a shows the Raman spectrum before the cleaning. The single-layer h-BN peak is visible over the contamination 'bump'. Figure 4.5b shows the Raman spectrum of h-BN with a contamination features after the oven annealing in air at 450°C. Figure 4.5c shows the Raman spectrum of the material without the contamination signature as result of the cleaning in ozone environment for 30 minutes.

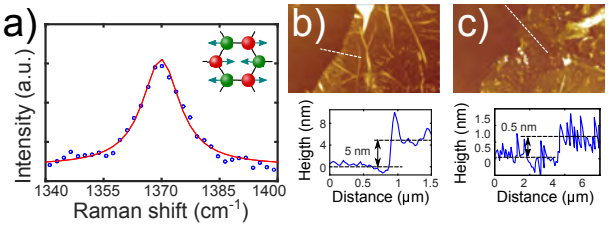

Figure 4.4: Single-layer h-BN characterization. (a) Raman spectroscopy is used to determine the single-layer nature of the suspended material. As reported in reference [76], we find a peak at 1370 cm^{-1} that corresponds to a monolayer h-BN. Inset: Vibrational mode of a h-BN ring for that Raman frequency. (b) AFM height image of a h-BN material edge before cleaning. The obtained thickness (5 nm) is larger than that expected for single-layer (0.44 nm). The material is covered with polymer contamination that can be removed by oven annealing at 450°C in air and ozone as seen in (c), where areas of 0.5 nm thick are found.

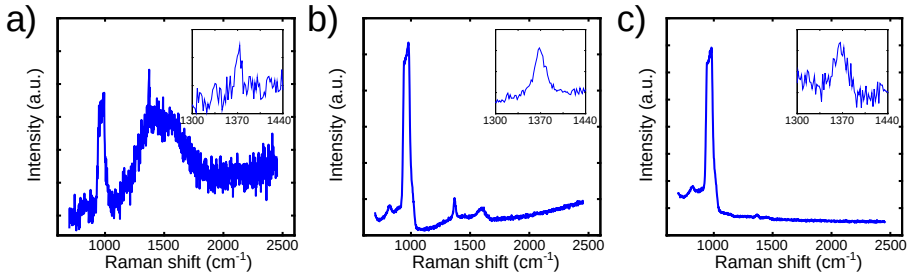

Figure 4.5: Raman spectrum of the h-BN material (a) before cleaning, (b) after oven annealing, and (c) after ozone cleaning.

4.3.2. THICKNESS BY AFM

The thickness and topographic flatness are measured with an atomic force microscope (AFM, Bruker Fastscan) in tapping mode (FastScan-A probe). As observed in Figure 4.4b, the AFM indicates a thickness of 5 nm which is larger than that of a monolayer (0.44 nm), probably due to polymer contamination that disappears in some areas after cleaning processes as seen in Figure 4.4c.

4.4. MECHANICAL CHARACTERIZATION OF RESONATORS BEFORE/ AFTER CLEANING

The static mechanical characterization of suspended CVD single-layer h-BN is performed by AFM nanoindentation. We use the Peak Force mode (ScanAsyst-Fluid probe) to deflect drums of 5 μm in diameter with a controlled force of 5 nN. Figure 4.6a shows the AFM image of the suspended drum from Figure 4.1b with its corresponding force-deflection curve at its center. The tension and Young's modulus of the material are extracted by fitting the data for positive forces to the following equation valid for a circular structure under a central point load F [157]:

$$F = \left[\frac{4\pi t^3 E}{3(1-\nu^2)R^2} + \pi N_0\right]\delta + \frac{tE}{(1.05-0.15\nu-0.16\nu^2)^3 R^2}\delta^3, \tag{4.1}$$

where N_0, E and $\nu = 0.18$ [167] are the pre-tension, Young's modulus and Poisson's ratio of the suspended material (chosen as an intermediate value in the range reported in literature), respectively; $t = 0.44$ nm is its thickness, R is the radius of the drum, and δ is the deflection induced by the AFM tip. The Young's modulus E is extracted by fitting the large-deformation data to the cubic term, although for small applied forces the accuracy is limited. The thickness-dependent term of the linear spring constant is negligible in these atomically-thin devices as the transfer of the material usually introduces stress that dominates the response at small deformations. This membrane behavior (e.g., tension dominated suspended structures) is found experimentally in the h-BN drums as shown below.

The extracted tension and Young's modulus values are shown in Table 4.1 for the 5 different drums shown in Figures 4.2-4.3, and they are expected to be influenced by the polymer in a second order of importance. Note the large Young's modulus of an undamaged drum (device 5) which is comparable to that of pristine graphene [51], and the lower values obtained for the other perforated devices.

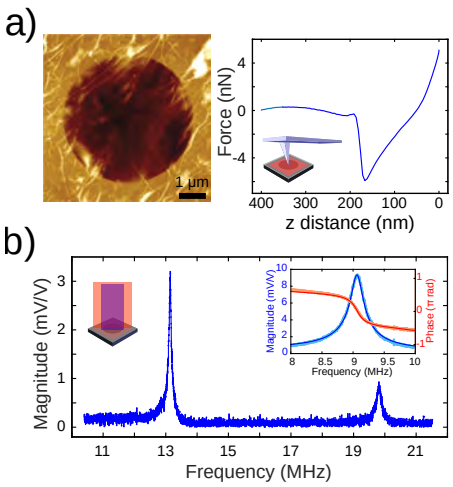

Figure 4.6: Characterization of h-BN 5 μm in diameter drums. (a) AFM image of the h-BN drum showed in Figure 4.1b. The CVD material shows wrinkles and sidewall adhesion as in CVD graphene (left panel). The force distance curve in the center of the drum is obtained by AFM indentation in Peak Force mode. From the retraction curve we extract the tension and Young's modulus. (b) Mechanical frequency spectrum of the same drum at room temperature and ~10^{-6} mbar when measured with the optical interferometric technique after cleaning. The second resonance peak appears around 1.5 times the fundamental frequency, indicating membrane behavior [157]. Inset: Mechanical fundamental frequency and phase analysis of the same drum before cleaning. By fitting the frequency peak to the driven harmonic oscillator equation, we extract the tension values.

The mechanical properties are also measured indirectly from the drum dynamics with a laser interferometric technique in a cryo-station setup (Montana Instruments). A power-modulated diode laser ($\lambda = 405$ nm) photothermally actuates the drum while a continuous-wave He-Ne laser ($\lambda = 633$ nm) allows the measurement of its resonance frequency f_0 [164]. Figure 4.6b displays the frequency spectrum of the same drum shown in Figure 4.6a at a room temperature and pressure of ~10^{-6} mbar, showing the fundamental mode around 13 MHz and the second (splitted) mode around 1.5 times the fundamental one. The factor of 1.5 indicates that the single-layer h-BN acts as a membrane in which pre-tension dominates over the bending rigidity [157]. The fundamental mode is given by:

$$f_0 = \frac{2.4}{2\pi R}\sqrt{\frac{N_0}{\rho t}}, \tag{4.2}$$

where $\rho = 2100$ kg/m^3 is the mass density of the suspended material. By fitting the fun-

Device	N_0 (10^{-3} N/m)	E (GPa)
1	21	102
2	25	199
3	21	186
4	38	81
5	48	936

Table 4.1: Tension and Young's modulus values determined from AFM nanoindentation measurements before cleaning for 5 different drums of 5 μm in diameter.

	Before cleaning		After oven annealing		After UV cleaning	
Device	f_0 (MHz)	N_0 (mN/m)	f_0 (MHz)	N_0 (mN/m)	f_0 (MHz)	N_0 (mN/m)
1	8.5	2.7	14.8	8.6	9.1	3.3
2	9.9	3.7	13.5	7.2	14.2	7.9
3	10.0	3.8	17.8	12.5	19.9	15.6
4	10.4	4.1	9.9	3.9	17.0	11.4
5	9.1	3.1	13.2	6.8	20.3	16.3

Table 4.2: Fundamental frequency and tension of CVD single-layer h-BN drums at room temperature from the laser interferometric technique before and after cleaning in harsh environments.

damental peak to the response function of a harmonic oscillator, we extract the resonance frequency that is used to calculate the tension from Equation 4.2. The pre-tension values are shown in Table 4.2.

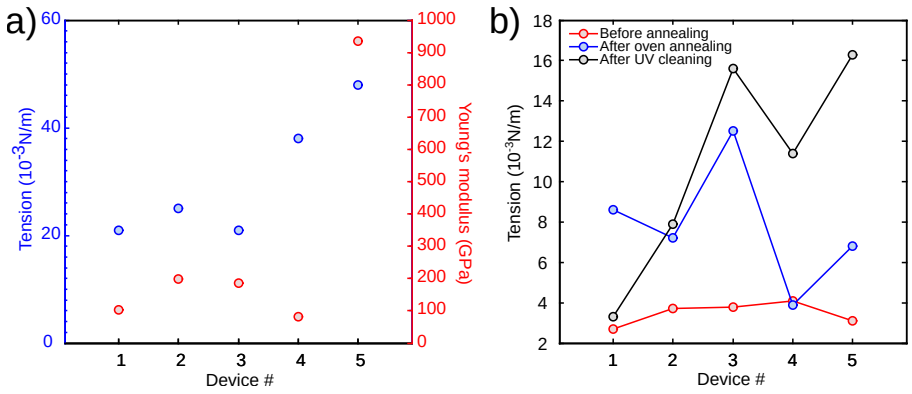

Figure 4.7: Mechanical properties of the devices at room temperature. a) Tension and Young's modulus values determined from AFM nanoindentation measurements (Table 4.1). b) Extracted tension values from the laser interferometric technique before and after cleaning in harsh environments (Table 4.2). The tension values assume that the devices are clean (mass density of only one layer of h-BN).

Figure 4.7 displays the data presented in Table 4.1 and 4.2 in the main text. Figure 4.7a

shows the tension and Young's modulus of the 5 different devices of 5 μm in diameter measured by AFM indentation (before cleaning). Device 5 has a larger Young's modulus than the other devices possibly due to the lack of small perforations in the membrane. Figure 4.7b shows the apparent tension of the same devices when using the laser interferometer before and after the cleaning processes. There is a clear trend in the devices to increase their frequency after each consecutive cleaning process.

4.5. TEMPERATURE DEPENDENCE OF THE RESONANCE FREQUENCY

When cooling a resonator, the resonance frequency and quality factor increases as pictured in Figure 4.8.

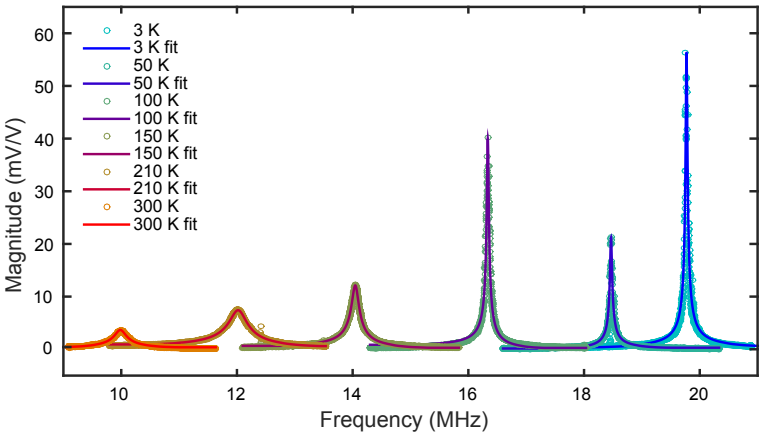

Figure 4.8: Evolution of the fundamental resonance frequency with temperature for a h-BN drum before cleaning (device 3).

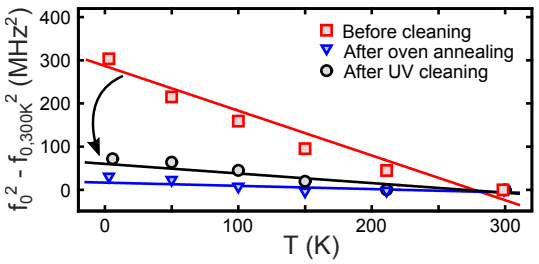

Figure 4.9: Temperature dependence of the mechanical resonance frequency (fundamental mode) averaged for the h-BN drums before cleaning, after oven annealing, and after UV ozone cleaning. By cooling the drums from 300 K down to 3 K, the material is tensioned resulting in higher frequencies. Despite the expected negative in-plane thermal coefficient of h-BN, no compression is observed even after cleaning, hence suggesting that other tensioning mechanisms are present.

Figure 4.9 shows the temperature dependence of the fundamental frequency when cooling the device from 300 K to 3 K. Equation 4.2 is modified to take into account the temperature-induced tensioning of the membrane due to the in-plane expansion coefficients of the 2D material and the underlying substrate dominated by the thermal expansion of the Si:

$$f_0(T) = \frac{2.4}{2\pi R}\sqrt{\frac{N_0}{\rho t} + \frac{N_{adhesion}(T)}{\rho t}}, \tag{4.3}$$

$$N_{adhesion}(T) = \begin{cases} Et\frac{\Delta T}{(1-\nu)}(\alpha_{Si} - \alpha_{2D}), & \alpha_{Si}(T) < \alpha_{2D}(T) \\ N_{sidewall}, & \alpha_{Si}(T) > \alpha_{2D}(T) \end{cases}$$

where α_{Si} and α_{2D} are the temperature-dependent expansion coefficient of silicon and the 2D material, respectively, in the basal plane; $\Delta T = T - 300$ K is the temperature difference from room temperature. $N_{sidewall}$ is a new tensioning mechanism that originates from the adhesion of the suspended 2D material to the sidewalls of the circular cavity, which happens when the membrane tries to expand laterally inside the cavity as shown in Figure 4.10a.

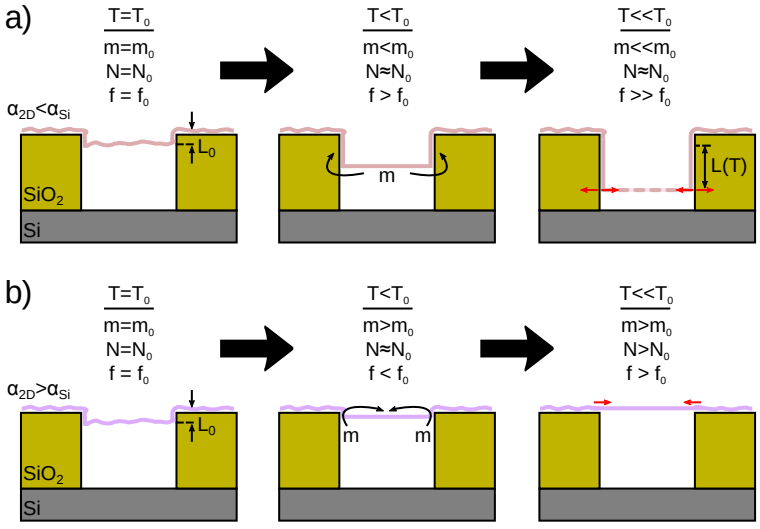

Figure 4.10: Behavior of 2D membranes with an initial sidewall length L_0 when being cooled down. a) A suspended 2D material with negative expansion coefficient like h-BN or graphene tends to expand by sending part of the freestanding mass to the sidewalls of the cavity, hence resulting in an increase of the sidewall length $L(T)$. Without assuming a particular model, we would expect a self-balancing of adhesion-separation forces at the edges of the membrane that may not change much its tension, while the loss of suspended mass would induce an increase of its resonance frequency. b) On the other hand, if the suspended 2D material has a positive expansion coefficient like MoS_2, the suspended material will compress by retracting part of the adhered mass in the sidewalls of the cavity (delamination), hence resulting in a decrease of $L(T)$. This action would initially enlarge the suspended mass (decreasing the resonance frequency) until the membrane reaches the edge of the cavity and starts tensioning.

This adhesion could balance out ($N_{sidewall} = 0$) [168] or increase the tension due to a biaxial in-plane strain ($N_{sidewall}(T) = Et\frac{6tL(T)}{R^2} \propto \alpha_{2D}\Delta T$, where L is the change of adhered length on the sidewall) [159]. When cooling down the device made out of single-layer h-BN with negative in-plane thermal expansion coefficient ($\alpha_{Si}(T) > \alpha_{h-BN}(T)$), we would expect a constant or monotonic increase of f^2, i.e., $f_0^2(T) - f_0^2(300\text{ K}) \propto T$ with a zero or negative slope. The data, red circles in Figure 4.9, show such a trend suggesting that $N_{adhesion} = N_{sidewall}$. However, another possible explanation for this could be residual resist remaining on top of the h-BN after transfer.

4.6. IMPACT OF CLEANING PROCESSES

To test these hypothesis, we clean the membranes by annealing the samples at 450°C for 3.5 hours in an air environment (78% N_2, 21% O_2), and in a further cleaning step using UV-induced ozone environment for 30 minutes. The oven annealing is expected to cause thermal and chemical degradations of polymers (boiling and evaporation of PVA, oxidation and gasification thermolysis of PMMA), and the UV ozone cleaning should produce photo-induced and chemical decomposition of polymers (photolysis of remaining PVA/PMMA and ozonolysis of PDMS) and decomposition of other organic matter with the UV ozone cleaning. Despite these cleaning processes in harsh environments, the h-BN remains suspended and the material becomes invisible under the optical microscope as expected from its low absorption of visible light [76], thus indicating that the contaminating polymer layer has been largely removed. After the treatments, the fundamental mode frequency at room temperature increased for all drums, although slightly. We also repeated the measurement as a function of temperature as shown in Figure 4.9 by the blue (after oven annealing) and black data points (after ozone cleaning). The conclusion from the data is that when cooling a slight increase in the resonance frequency remains, although the effect is smaller than before annealing.

4.7. DISCUSSION

References [75] and [169] report the mechanical characterization by AFM indentation of similar devices made out of CVD multilayer h-BN (1-2 nm and 5-15 nm in thickness, respectively). In those works, the material is placed on top of cavities with different transfer techniques that also introduce polymer contamination and wrinkles as we have observed in our devices by SEM and AFM. The Young's modulus reported (220-250 GPa and 1160 GPa, respectively) are comparable to our measured values at room temperature, and in particular device 5 proves to have a stiffness close to the theoretical value of single-layer h-BN (885-995 GPa). In another work on graphene [170], the temperature-dependence of the Young's modulus was proven to be strongly influenced by the presence of wrinkles in the suspended membranes. More importantly, the previous works on h-BN present membranes that sag into the cavities due to the van der Waals forces between the material and the sidewalls. Considering that the 2D Young's modulus scales with the thickness, it is expected that single-layer h-BN shows larger sagging than previously reported (20-50 nm and 15 nm, in

the mentioned works). AFM scans of our devices show sagging of 50-60 nm, thus supporting the monolayer nature of the material.

Bulk h-BN has a negative in-plane thermal expansion coefficient for temperatures higher than 75 K [171]. We assume that single-layer h-BN exhibits the same tendency as graphene with respect to graphite, i.e., that it has the same negative temperature dependence as in the bulk, but with a larger magnitude [172]. The observed tensioning must therefore originate from a) an unexpected positive in-plane thermal expansion coefficient for h-BN as a single layer caused by the presence of polymer contamination even after cleaning [122], b) other tensioning mechanism such as the proposed sidewall adhesion or the presence of wrinkles, or c) defect creation during UV ozone cleaning.

When comparing the tension values from the AFM and the laser interferometric studies as shown in Tables 4.1 and 4.2 (before cleaning), we observe a difference of one order of magnitude between the two. The indirect calculation of the tension from Equation 4.2 includes the mass of the membrane as a parameter as opposed to the direct measurement, where the mass does not appear in Equation 4.1. In fact, the thickness of the material measured by AFM before cleaning (5 nm, about 10 times that of single-layer h-BN) may explain the difference in values obtained from the AFM indentation and the laser interferometric techniques. The spread in values obtained with both techniques can also be justified with residues of inhomogeneous thickness and hence mass. In addition, the quality factors increased significantly with respect to the pre-cleaning values as shown in Figure 4.11b, suggesting that the polymer residues play a significant role in damping the mechanical motion, probably due to their visco-elastic properties.

Figure 4.11 shows the dependence of the mechanical properties with temperature. The dissipation (Q^{-1}) in these kind of systems has a low-temperature $T^{1/3}$ and high-temperature T^2 or T^3 power-law dependences, which are still not understood [56, 105]. From Figure 4.11b we obtain an low-temperature dependence of $T^{0.49}$, $T^{0.22}$, and $T^{0.07}$ for the h-BN drums before cleaning (red circles), after annealing (blue circles), and after ozone cleaning (black circles), respectively. The high-temperature power-law dependence for those cases become $T^{2.10}$, $T^{0.82}$, and $T^{0.76}$.

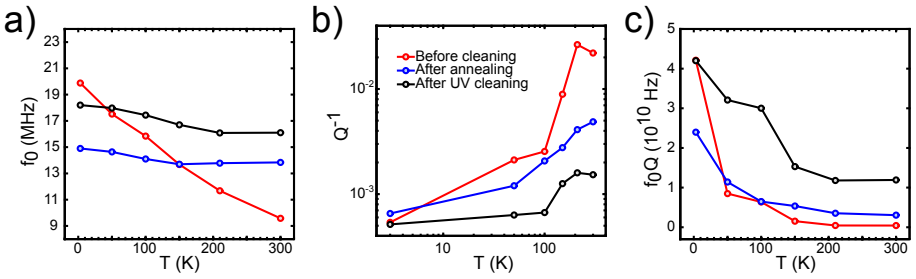

Figure 4.11: Temperature dependence of the mechanical properties for the h-BN drums before cleaning, after oven annealing, and after UV ozone cleaning. a) Averaged frequency versus temperature. b) Averaged dissipation versus temperature. c) Averaged $f_0 Q$ product versus temperature.

On the other hand, the increase of the fundamental frequencies at room temperature before and after cleaning (Table 4.2) indicates that either the oven annealing introduced larger pre-tensions (enhanced adhesion to the surface or the sidewall of the cavity) and/or a decrease in the mass (hence obtaining tensions more similar to those obtained from the AFM) according to Equation 4.2. The mechanical quality factor of the resonators improved after each of the two cleaning steps. This fact coupled to the disappearance of traces of polymer contaminants and the on-average increase in the resonance frequency of the resonators suggests that polymer contamination is the main damping mechanism encountered in these resonators. It is unclear if there remains some polymer residue, although the tensioning trend when cooling has been reported in graphene and several transition metal dichalcogenide membranes [56, 105, 173]. However, this trend should be explained differently for 2D materials with a negative expansion coefficient like h-BN or graphene [174], and for that reason we propose an alternative tensioning effect caused by the sidewall adhesion, which should balance out or increase the tension when cooling certain 2D membranes, and explains our results and those on graphene drumheads. Other stronger cleaning routes for h-BN are available [175, 176], although not all of them might be compatible with suspended single-layer structures.

4.8. CONCLUSIONS

This study has presented the fabrication, mechanical characterization and cleaning of CVD single-layer h-BN drumhead resonators. We have developed a transfer technique that allows the transfer of this extra-adhesive material from the growth substrate to a patterned SiO_2 surface with circular microcavities, resulting in suspended h-BN drums. The tension and Young's modulus of the material were characterized by performing AFM indentation on several devices, and the tension values are compared to those measured indirectly from the resonance frequency by means of laser interferometry. The temperature dependence of the dynamics of the drum is realized by cooling the devices to 3 K, and corroborates the assumption of having polymer residues covering the h-BN that dominates the tensioning of the devices. After cleaning in harsh environments, we observe a substantial improvement in the quality factor of the drums, and a change in their temperature-induced tensioning, which demonstrates cleaning of the suspended material. However, the temperature behavior suggests that some residues may still be present or that the structural mechanics model needs to be revisited for 2D materials, thus requiring further research. The strong adhesion of h-BN layers compared to other 2D materials could be exploited to make highly sensitive mechanical systems. Its electrical and optical properties are different than those from graphene, hence being a desirable material for applications where low-optical absorption or electrical insulation is required. Its nearly-zero extinction coefficient above 500 nm and good reflectivity could be used to make large f_0Q NEMS for optomechanics experiments. Moreover, it could be combined with other 2D materials to fabricate NEMS *à la carte* with new functionalities for transparent and flexible electronics.

Application 3: CVD graphene for pressure sensing

5

MASSIVE CHARACTERIZATION OF GRAPHENE MECHANICAL DEVICES USING A COLORIMETRY TECHNIQUE

Let there be light.

Anonymous, *Genesis 1:3*

The truth is a puzzle of lies: the more pieces one collects,
the truer our experience-based interpretation of reality becomes.

Santiago, Granada 2009

We use a scalable optical technique to characterize more than 21000 circular nanomechanical devices made out of suspended chemical-vapor-deposited (CVD) single- and double-layer graphene on cavities with different diameters (D) and depths (g). To maximize the contrast between suspended and broken membranes we used a model for selecting the optimal color filter. The method enables parallel and automatized image processing for yield statistics. We find the survival probability to be correlated to a structural mechanics scaling parameter given by D^4/g^3. Moreover, we extract a median adhesion energy of $\Gamma = 0.9\ J/m^2$ between the membrane and the native SiO_2 at the bottom of the cavities.

Parts of this chapter have been published in Nanoscale **9**, 7559-7564 (2017) by S.J. Cartamil-Bueno, A. Centeno, A. Zurutuza, P.G. Steeneken, H.S.J. van der Zant, and S. Houri.

5.1. INTRODUCTION

Studies performed so far on CVD graphene have shown large variations in its physical properties such as Young's modulus [114], mass density or stress [105, 111] and permeability [117]. To get a better insight into these variations, the mechanical properties of CVD graphene should be determined not only at device level, but also on a very-large-scale integration (VLSI) level for commercial applications.

Although inspection via optical microscopy could be used for such a massive characterization, the monoatomic thickness of graphene leads to a low optical reflectivity that makes it hard to study. Visibility under an optical microscope can be enhanced by selecting the thickness and optical properties of the underlying substrate [177]. However, this approach has not yet been applied in the case for suspended graphene. Statistical studies were performed with laser interferometry [105, 111], Raman spectroscopy [106, 112, 113, 156], atomic force microscopy [114, 115], and electrical modulation [178], but such approaches tend to be complicated and time consuming hence preventing a successful commercialization of graphene mechanical devices.

In this work, we use a scalable colorimetry technique [153] to measure yield statistics on more than 21000 graphene drumheads of different diameters and cavity depths (several substrates) for both CVD single-layer (SLG) and double-layer graphene (DLG). We also use an optical model to optimize the reflectance contrast between suspended and broken devices. With these tools, we obtain the survival probability of SLG and DLG samples, and find a scaling rule that governs the yield of suspended CVD graphene membranes.

5.2. FABRICATION AND SETUP

Device fabrication starts by etching circular holes into the thermally-grown SiO_2 layer on a silicon chip. A total number of 3016 circular cavities are produced on each sample substrate, having diameters ranging from 2 to 20 μm. Several chips are fabricated with cavity depths of 285, 570, 630 and 1140 nm, and two additional samples of 630 nm are coated with a thin layer of Au/Ti (100 nm/10 nm). Afterwards, the samples are sent to Graphenea to transfer the CVD SLG and CVD DLG (DLG membranes are made by stacking two SLG CVD graphene layers).

Upon inspection of the suspended structures with an optical microscope, the surviving devices prove to be difficult to identify as they offer very low optical contrast with broken drums. This low contrast is seen in the rightmost panels of Figure 5.1 for cavities of 1140 nm in depth in two different samples (SLG top, and DLG bottom), in which under white light illumination a suspended drumhead is indiscernible from the broken ones. This is due to interference of the light being reflected from the Si substrate and that being reflected from the graphene layer [78]. This interference can be either constructive or destructive depending on the wavelength λ and effective cavity depth g (distance between the membrane and the bottom of the cavity). In the case of white light illumination, these constructive and destructive interference contributions average out, thus reducing the observed contrast such that suspended drums become indiscernible.

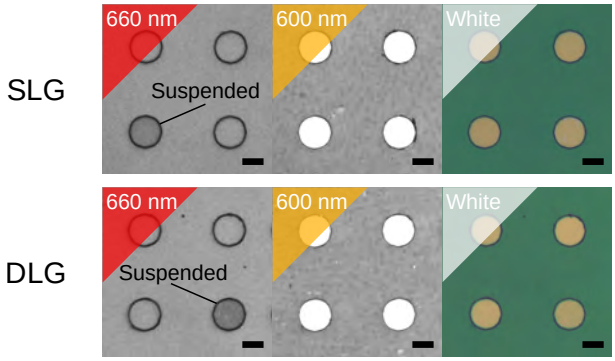

Figure 5.1: Visualization of suspended graphene drumheads using color filters. Optical microscope images with narrow band illumination (660 nm and 600 nm) and white light for CVD single layer (SLG) and double layer (DLG) graphene suspended on Si/SiO_2 cavities 1140 nm deep. The suspended 15 μm-in-diameter graphene membranes appear darker than the broken ones when using a color filter of 660 nm. Scale bars are 10 μm.

A judicious selection of the illumination wavelengths can increase the contrast and therefore the visibility of the suspended drums. A similar approach was taken to make supported graphene on SiO_2 more visible [177].

An OLYMPUS BX60 optical microscope with Köhler illumination is used with its halogen lamp as the effective multiwavelength white light source. Pictures are taken using an infinity corrected 20× objective lens (OLYMPUS UMPlanFI) with a numerical aperture of 0.46 and a 3 mm working distance. A consumer camera (Canon EOS 600D) collects images of the sample in a monochrome RAW format. A series of color filters (Thorlabs FL460, FLH532, FB600, FLH633, FBH660) are mounted on a motorized computer-controlled wheel, and placed in front of the camera imager as shown schematically in Figure 5.2.

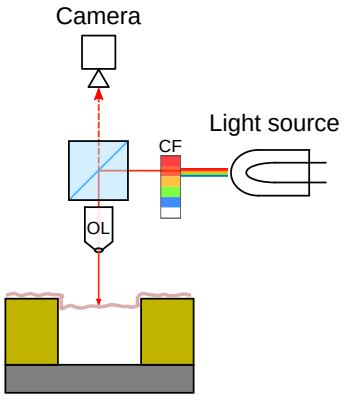

Figure 5.2: Colorimetry setup: an optical microscope with Köhler illumination and a 20× objective lens (OL) is used for visualizing the drums. The white light illumination of a halogen lamp goes through a color filter (CF).

Under the 20× magnification it is possible to observe 500-1000 graphene drums simultaneously (depending on their diameter), as shown in the example image in Figure 5.3. Thus for each of the samples, that contains 3016 cavities, a total of three optical microscope images per color filter are enough.

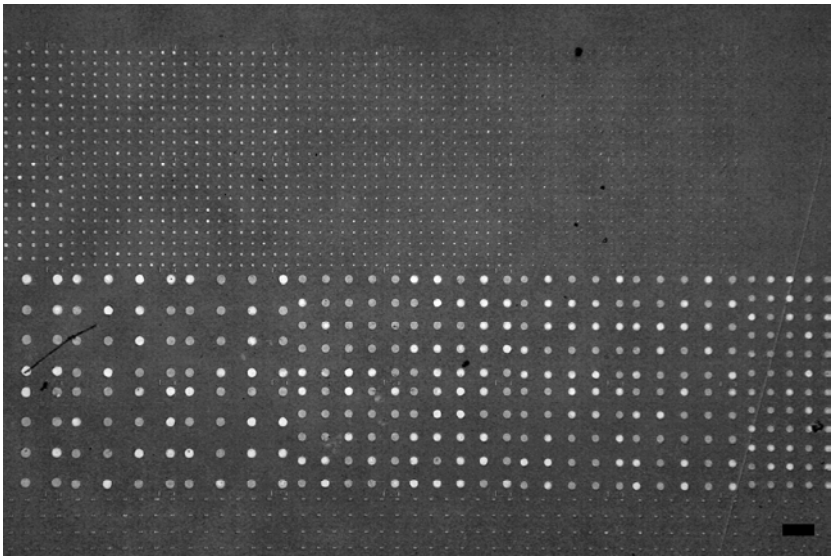

Figure 5.3: Example of an optical microscope picture taken with 460 nm color filter. Nearly 1000 drums of varying diameters are seen. In this particular image, dark devices are suspended drumheads. Scale bar is 50 μm.

5.3. CONTRAST BETWEEN SUSPENDED AND BROKEN DRUMHEADS

The enhancement of the optical contrast between suspended and broken drumheads is shown in the leftmost panels of Figure 5.1 where a 660 nm color filter (10 nm of bandwidth) enables their identification. On the other hand, this contrast is once again lost if a filter wavelength of 600 nm is chosen. As seen in the figure, the behavior is common to both SLG and DLG, although the DLG membrane absorbs more light thus giving a higher contrast between suspended and broken devices.

For a given cavity depth, the relation between reflected contrast and light wavelength can be understood with a Fresnel-law model with three optical layers (air, graphene, air) interfacing a reflective substrate (silicon). The reflectance of the suspended membrane can be written as:

$$R = |2r_1 e^{i\phi_2}\sin(\phi_1) + r_2 e^{-(\phi_1+\phi_2)} - \frac{r_1^2 r_2 e^{i(\phi_1-\phi_2)}}{e^{i(\phi_1+\phi_2)} + r_1^2 e^{-i(\phi_1-\phi_2)} + 2r_1 r_2 e^{-i\phi_2}\sin(\phi_1)}|, \tag{5.1}$$

where r_1 and r_2 are the Fresnel reflection coefficients of air-graphene and air-silicon interfaces, respectively. ϕ_1 and ϕ_2 are the phase changes induced by the optical path through the graphene and the cavity respectively, t_G is the graphene layer thickness, and λ is the optical wavelength [177].

To find the optimum wavelength to differentiate suspended from failed membranes, we use the Weber contrast between the reflectance of a suspended membrane and the silicon substrate (representative of a broken drum). The Weber contrast, C, is defined as:

$$C = \left| \frac{R - R_{Si}}{R_{Si}} \right|. \tag{5.2}$$

Figure 5.4 plots the calculated values of C for different cavity depths and wavelengths in the case of SLG. The reflected contrast value can be maximized for a given cavity depth by selecting the optimal illumination wavelength. For instance, the freestanding membranes of the samples in Figure 5.1 would be more visible when using color filters of 420 nm, 510 nm or 660 nm (dotted vertical red line at cavity depth = 1140 nm). On the contrary, illumination of 600 nm would lead to a lower contrast, as seen experimentally.

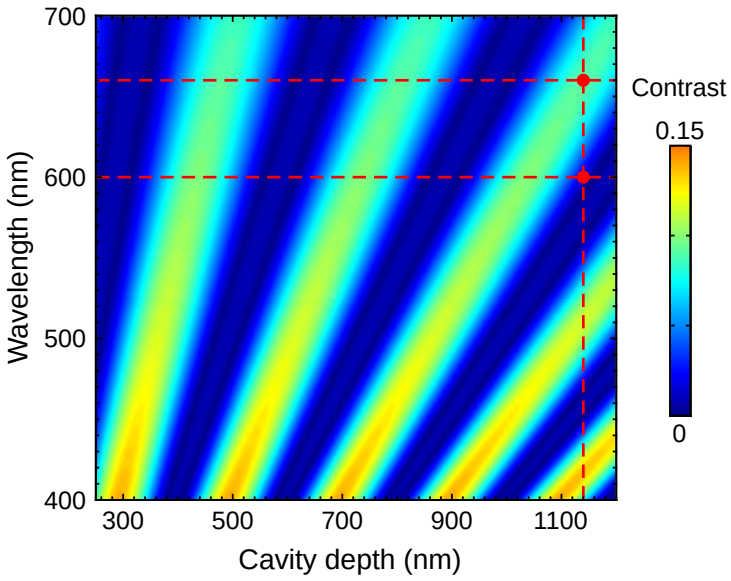

Figure 5.4: Calculated optical Weber contrast (C) as a function of the cavity depth and light wavelength for freestanding SLG. For a given cavity depth, the contrast between a suspended membrane and the silicon substrate (broken device) can be maximized by choosing the right color filter. The intersections of the dashed red lines indicate the expected contrasts for the drumheads shown in Figure 5.1 (depth of 1140 nm). The refractive index of graphene is taken to be n_G =2.6-1.3i.

5.4. YIELD STUDY: NUMBER OF LAYERS, DEVICE DIAMETER AND CAVITY DEPTH

Next, we perform a large-scale characterization of device yield by using the colorimetry technique. Filtered microscopic images with 500-1000 cavities each are taken with a colorimetry setup and analyzed with image edition tools. The measurements are done on samples that have undergone more than 2000 stress cycles consisting of changing the environment pressure from 1 bar to 10 mbar (pumping) and viceversa (venting). For all cavity depths the optimum filter is selected using Figure 5.4. Filtered microscopic images of large numbers of drums are made and analyzed. We calculate the yield as the ratio of surviving-to-total drums, we obtain the error bar as the standard deviation divided by the square root of the total number of devices, and we equate the yield fraction with survival probability by inserting the corresponding error bar.

Figure 5.5 collects the yield for the SLG and DLG samples (top and bottom panel, respectively) for different cavity depths (in different colors). The solid lines are guide-to-the-eye sigmoid curves plotted to show the survival probability dependence of suspended membranes on the cavity diameter. Three trends are clearly observable: the yield increases with deeper cavities, the yield reduces with increasing diameter, and the yield of DLG is higher than that of SLG. The only notable exception are the DLG samples with 1140 nm cavity depth that will be discussed below.

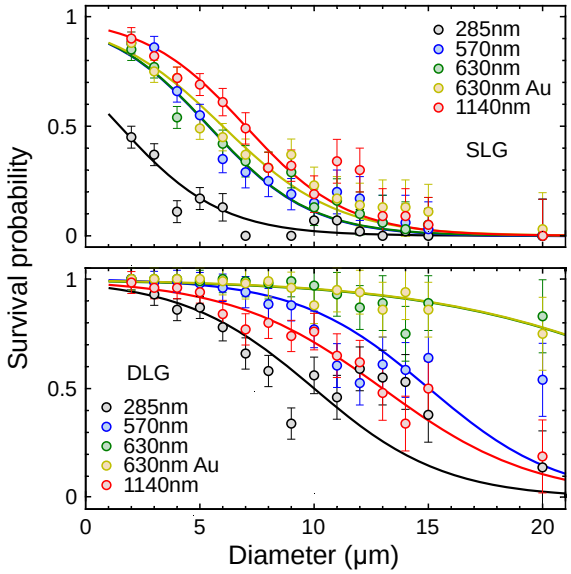

Figure 5.5: Survival probability of suspended CVD SLG (top) and DLG (bottom) as a function of cavity depth and diameter. Sigmoid curves (solid lines) are added as a guide to the eye to underline the tendency of large drumheads and shallow cavities to fail. The survival probability is significantly higher for DLG samples. The legend values indicate the cavity depth g.

5.4.1. FAILURE MECHANISM AND SCALING PARAMETER

To quantitatively understand the dependence of the yield on the cavity diameter and depth, we hypothesize that failure is caused by the physical contact between the drums and the Si bottom of the cavity. The contact would take place when the membranes deflect downwards under the effect of a pressure difference between the inside and outside of the cavity.

In the above failure mode, the drum's deflection needs to be equal to the cavity depth. By treating the drums as circular elastic membranes, it is possible to relate the maximum deflection of the center of the membrane δ to an external force as:

$$F = \Delta P A_T = k_1 \delta + k_3 \delta^3, \tag{5.3}$$

where F is the force causing the membrane to deflect, originating from the pressure difference ΔP acting on the drum's total area A_T. k_1 and k_3 are the linear and cubic stiffness of the circular membrane [153, 179, 180]. Since we assume membrane behavior, the linear component of the stiffness is dictated by the pre-tension T_0 in the structure, $k_1 = 4\pi T_0$. The nonlinear component originates from the stretching of the membrane as it deforms, with $k_3 = \frac{32\pi E_{2D}}{3D^2(1-\nu)}$. Here, E_{2D} is the 2D Young's modulus of the graphene membrane taken to be 350 N/m for the SLG [51] and 700 N/m for DLG, $\nu = 0.16$ is the Poisson's ratio of graphene, and D is the membrane's diameter. With typical values of k_1 around tens of mN/m, it is clear that the nonlinear term dominates for deflections on the order of 100 nm and larger. Then for $\delta = g$, the correspondence between the cubic term and the pressure difference deforming the membrane is given by:

$$\frac{E_{2D}}{\Delta P} \approx \frac{3(1-\nu)}{128} \frac{D^4}{g^3}. \tag{5.4}$$

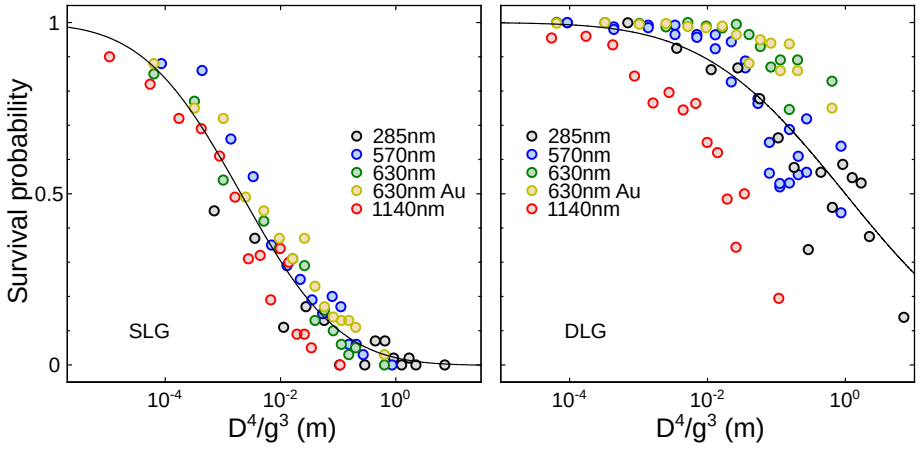

Figure 5.6: Fitted logarithmic-Gaussian distribution (solid lines) of the survival probability of 5715 suspended SLG drumheads (left) and 16079 suspended DLG drumheads (right) plotted against the cubic stiffness parameter D^4/g^3.

Therefore, for a certain pressure difference ΔP it is expected that the drums with $\frac{D^4}{g^3} < \frac{128E_{2D}}{3(1-\nu)\Delta P}$ will not touch the bottom of the cavity, and will thus survive. In Figure 5.6 we plot the yield of all the data for SLG (left panel) and DLG (right panel) as a function of the scaling parameter D^4/g^3. It is clear from the figure that the different samples tend to collapse on a single curve with a trend that can be fitted using a logarithmic Gaussian distribution (solid lines). From the fit we obtain using Equation 5.4 the median value of $E_{2D}/\Delta P$ to be $4.1 \cdot 10^{-5}$ m for SLG and $2.2 \cdot 10^{-2}$ m for DLG. Thus, doubling the number of graphene layers shifts the median value of the scaling parameter by three orders of magnitude. The survival probability in Figure 5.6 follows a distribution that extends over 5 decades, whereas typical variations in the Young's modulus of CVD graphene are on the order of 10% [114], and cannot therefore explain the span of the observed distribution. However, since the membranes have different permeabilities, they will not experience the same ΔP during pressure cycling, which can explain the extracted ratio $E_{2D}/\Delta P$. Leakage could also account for some of the large 20 μm DLG membranes surviving the pressure test despite the predicted failure according to theory (Discussion section).

Moreover, the DLG sample with 1140 nm of cavity depth shows a larger failure probability for all diameters against the general trend. This fact could be an indication of a failure mechanism different from the collapse of the membrane and related to the cavity volume. Wherein, the volume plays an important role in the deflection of these devices due to the asymmetry between inflation and deflation of the membranes [153].

5.5. STUCK DRUMHEADS AND THEIR ADHESION ENERGY

Besides broken structures, another failure mode was observed in a small subset of the membranes (5-30% of the total devices per sample). These devices show fringes in the optical images as illustrated in the inset of Figure 5.9, which indicate that the devices are permanently adhered (stuck) to the cavity bottom. The collapsed drum shown in the inset was also mapped using an atomic force microscope (AFM) as shown in Figure 5.7.

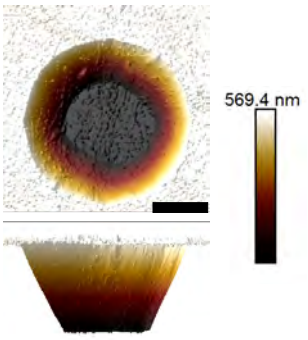

Figure 5.7: AFM image of a stuck drum see from above (top) and cross section (bottom). Scale bar is 5 μm.

These stuck devices give an opportunity to explore graphene adhesion to surfaces. Curiously, although we observe such stuck devices for the DLG samples we observe no such features in the SLG samples, indicating that adhesion ruptures and destroys suspended SLG membranes upon contact with the substrate.

We can obtain information about the adhesion energy by analyzing the adhered area A_S. By assuming a perfect clamping and approximating the stuck area by a circle, it is possible to extract the adhesion energy through the equilibrium between the adhesion force and the restoring tension.

We approximate the stuck region of the drum to a circular region concentric with the circular drum, and assume perfect clamping as shown in Figure 5.8.

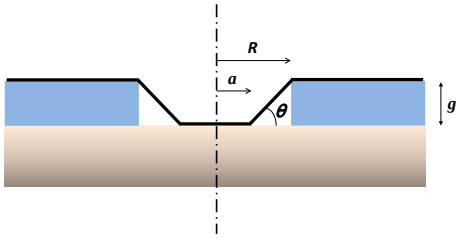

Figure 5.8: Model of a stuck circular membrane of radius R, the stuck area is assumed to be circular with a radius a, and a cavity depth g. The tensed suspended part of the membrane forms an angle θ.

The geometric proportions mean the angle θ is relatively small, we can therefore approximate the slope by:

$$\theta \approx \sin(\theta) \approx \tan(\theta) = \frac{g}{R-a} = \left(\frac{g}{R}\right)\frac{1}{1-\sqrt{\eta}}. \tag{5.5}$$

where $\eta = \left(\frac{a}{R}\right)$ is ratio of stuck-to-total area, g is the cavity depth, R is the drum's radius. We neglect radial displacement and assume only a vertical displacement $W(r)$ given as:

$$W(r) = \begin{cases} -g, & \text{for } 0 \le r < a \\ \frac{g}{R-a}(r-a) - g, & \text{for } a \le r \le R \end{cases} \tag{5.6}$$

The radial strain induced by elongation can be obtained as [181]:

$$\epsilon_r = \frac{1}{2}\left(\frac{\partial W(r)}{\partial r}\right)^2, \tag{5.7}$$

The strain energy of the membrane is given by [181]:

$$U_s = \frac{\pi E_{2D}}{2}\int_0^R \epsilon_r^2 r dr = \frac{\pi E_{2D}}{2}\int_a^R \epsilon_r^2 r dr, \tag{5.8}$$

Since the adhesion area does not change upon pressure cycling, the stuck drum is in a stable force equilibrium between adhesion force and the tension. The adhesion force given

as [182]:

$$F_{ad} = 2\pi a\Gamma, \tag{5.9}$$

where Γ is the adhesion energy in J/m^2. Inserting Equation 5.7 in Equations 5.8 and 5.9, and applying the static force equilibrium condition, i.e. $F_{strain} = \frac{dU_s}{da} = F_{ad}$, the adhesion energy Γ can be expressed in terms of geometric parameters and E_{2D} as:

$$\Gamma = 16E_{2D}\left(\frac{g}{D}\right)^4 \frac{2+\sqrt{\eta}}{\sqrt{\eta}\left(1-\sqrt{\eta}\right)^4}. \tag{5.10}$$

The histogram of the extracted adhesion energy is shown in Figure 5.9 for a total of 506 DLG devices stuck to the bottom of their cavities. By fitting a logarithmic Gaussian distribution to the histogram (red line), we obtain a median value for the adhesion energy of 0.9 J/m^2. The obtained value of adhesion energy for a pristine graphene-SiO_2 contact is higher than that reported in literature [183, 184, 185, 186] or expected by theory [101, 187, 188]. Note that here we consider the bottom of the silicon cavity to be covered with a native oxide layer. This higher-than-expected adhesion energy can have its origin in graphene slippage or sliding [120]. If slipping takes place, the strain in the membrane would relax compared to that calculated based on ideal clamping, thus skewing the obtained value of Γ. More indication to this latter effect can be seen from comparing Raman images of a suspended and a stuck drum obtained by fitting the G and 2D peaks (5.6).

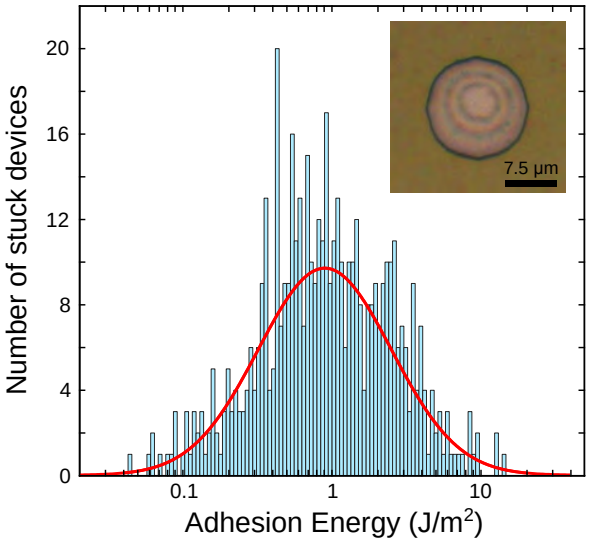

Figure 5.9: Histogram of the adhesion energy of 506 stuck DLG drumheads (all samples on SiO_2). The fitted Gaussian distribution appears as solid line. Inset: Optical image of a stuck drumhead. Scale bar is 15 μm.

5.5.1. COLLAPSED DEVICES AS A FUNCTION OF DIAMETER

Figure 5.10 shows the ratio of stuck devices to the total number of devices as a function their diameter. Only samples with the cavity depths in the legend contain these stuck devices.

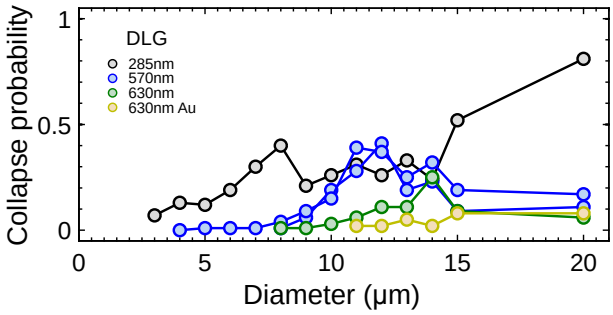

Figure 5.10: Proportion of stuck drums as a function of their diameter.

5.6. RAMAN SPECTROSCOPY OF SUSPENDED AND COLLAPSED DRUMS

A Renishaw in via system is used to scan a focused laser spot (λ = 514 nm) over the a suspended and a collapsed drumheads of 15 μm in diameter and 570 nm of cavity depth. We use the streaming feature to perform line scans of 25 μm in 360 s with steps of 600 nm at a laser power of 25 mW.

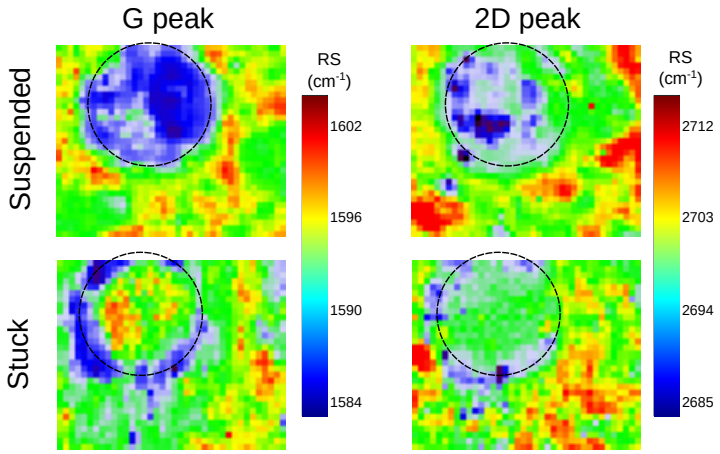

Figure 5.11: G and 2D Raman peak maps of a suspended (top) and a collapsed drums (bottom) of 13 μm in diameter.

Figure 5.11 shows the spatial maps of the G and 2D peaks of a freestanding (top) and a collapsed drums (bottom). The blue (red) color indicates low (high) Raman shift which implies a high (low) strain.

These images not only indicate a high strain in the stuck drum (in the suspended areas), but also a higher strain in the anchoring area nearest to the drum compared to the same area of the suspended drum, thus indicating that some of the stress induced by stiction is being transferred to the graphene outside the drum.

5.7. DISCUSSION

Equation 5.3 in the main text relates the deflection δ of a circular membrane under a pressure difference ΔP across it:

$$\Delta P = \frac{16T_0}{D^2}\delta + \frac{128\pi E_{2D}}{3D^4(1-\nu)A_T}\delta^3, \tag{5.11}$$

where T_0 is the pre-tension in the structure, E_{2D} is the 2D Young's modulus of the graphene membrane, $\nu = 0.16$ is the Poisson's ratio of graphene, and D is the membrane's diameter.

Assuming a perfectly impermeable membrane with $T_0 = 0.017$ N/m (Cartamil-Bueno et al, work in progress) under a pressure difference of 1 bar, we can find the theoretical limit of drums before collapse, in explanation, the minimum value of the Young's modulus to deflect the center of the circular membrane a distance equal to the depth of its cavity $\delta = g$. Figure 5.12 shows the colormap of the minimum Young's modulus for different cavity depths and diameters in the case of SLG (left) and DLG (right).

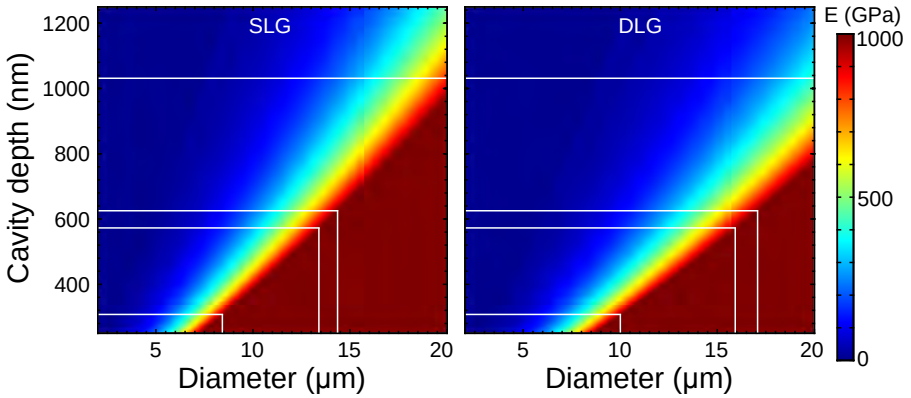

Figure 5.12: Minimum Young's modulus of circular SLG (left) and DLG (right) membranes for different diameters and cavity depths for which a pressure difference of 1 bar would induce a deflection equal to the cavity depth.

Given the fact that pristine graphene has a Young's modulus of 1 TPa and assuming that is the maximum value a CVD graphene can have, the theoretical model predicts a maximum diameter for a particular cavity depth beyond which the membrane would contact the bottom of the cavity and possibly collapse. For instance, all DLG membranes larger than 10 μm in diameter would contact the bottom of their cavities for cavity depths of 285 nm. The fact that some of the drums survive (Figure 5.5) even though they are expected to touch the cav-

ity bottom according to Figure 5.12, might be caused by unsticking from the cavity bottom or by membrane pores that result in smaller values of ΔP.

5.8. CONCLUSIONS

This chapter introduces a technique for fast yield characterization that can be automatized for large scale testing of graphene mechanical devices. We use a model that allows the selection of appropriate color filters to identify freestanding graphene devices under an optical microscope. We use the colorimetry technique to analyze more than 21000 drums that have underwent many thousands of pumping-venting cycles, and we show that a single scaling parameter (D^4/g^3), derived from structural mechanics, governs the survival probability of these 2D suspended structures. Moreover, doubling the number of graphene layers increases significantly the device yield for a same value of this scaling parameter. Furthermore, by analyzing the properties of DLG structures that are stuck to the bottom of the cavities, we are able to extract a value of adhesion energy as $\Gamma = 0.9$ J/m^2. This value is larger than what has been reported in literature, and it could be skewed by graphene slippage.

This work provides a framework for studying yield and failure mechanisms in arrays of suspended 2D material membranes. In particular these methods are expected to be useful for yield optimization in applications that require VLSI 2D nanomechanical arrays such as sensing systems or graphene interferometric modulation displays (GIMOD).

6

COLORIMETRY TECHNIQUE FOR SCALABLE CHARACTERIZATION OF SUSPENDED GRAPHENE

And yet it moves.

Galileo Galilei

Time will tell.

Santiago, Barcelona 2012

Previous statistical studies on the mechanical properties of chemical-vapor-deposited (CVD) suspended graphene membranes have been performed by means of measuring individual devices or with techniques that affect the material. Here, we present a colorimetry technique as a parallel, non-invasive, and affordable way of characterizing suspended graphene devices. We exploit Newton's rings interference patterns to study the deformation of a double-layer graphene drum 13.2 µm in diameter when a pressure step is applied. By studying the time evolution of the deformation, we find that filling the drum cavity with air is 2-5 times slower than when it is purged.

Parts of this chapter have been published in Nano Letters **16**, 6792–6796 (2016) by S.J. Cartamil-Bueno, P.G. Steeneken, A. Centeno, A. Zurutuza, H.S.J. van der Zant, and S. Houri.

6.1. INTRODUCTION

Statistical variations in the mechanical properties of single-layer graphene (SLG) drums have been extensively studied by measuring several drums with laser interferometry [105, 111], Raman spectroscopy [106, 112, 113], and atomic force microscopy [114, 115]. However, any attempt to commercialize graphene mechanical sensors is ineffective unless a characterization technique that is parallel, contactless, and affordable at the same time becomes available. Furthermore, CVD SLG usually contains gas permeable lattice defects and nanoscale pores due to its growth on imperfect substrates [116], which blocks its application in gas pressure sensing devices that require impermeable membranes. A possible route to overcome this difficulty is to stack several CVD layers to reduce the probability of having nanopores from different layers aligned on the same spot [117].

In this chapter, we introduce a new non-invasive optical technique to characterize the mechanical properties and the permeance of large arrays of suspended graphene membranes that is similar to Cornu's interference [189] and Fizeau interference [190] methods. We observe Newton's rings on a suspended CVD double-layer graphene (DLG) drumhead when applying a pressure difference between inside and outside of the cavity, which allows us to study the deformation of this mechanical system. We find that the rate of volume change is different for purging and filling the cavity with air. Based on these observations, the permeance of the DLG membrane is determined and found to be two to three orders of magnitude higher than that of pristine graphene.

6.2. FABRICATION AND SETUP

Device fabrication starts with a silicon substrate covered with 600 nm of thermally-grown SiO_2. Circular cavities of different diameters are patterned and etched through the oxide by means of reactive ion etching. Afterwards, a double-layer graphene, made by stacking two SLG CVD graphene layers, is transferred onto the SiO_2/Si substrate using a semi-dry transfer technique, thus resulting in suspended CVD-DLG drums. In this chapter, we use DLG membranes because their absorption in the visible spectrum of light is at least twice that of SLG, which increases its reflectance while remaining highly transparent [191].

Upon the application of a pressure difference between the inside of the cavity P_{int} and the outside of the cavity P_{ext}, the circular membrane is deformed. The drum deflects inward (upward) if the pressure difference $\Delta P = P_{ext} - P_{int}$ is positive (negative). Figure 6.1a shows an image of a DLG drum of 13.2 μm in diameter under white light illumination with $\Delta P \approx 1$ bar (top) and ΔP=0 (bottom). When the membrane is highly deflected as in Figure 6.1a, top panel, the circular geometry of the device causes the creation of concentric rings, which are also known as Newton's rings [192]. Progressively with time, air fills the cavity until P_{ext} and P_{int} become equal, resulting in a homogeneous color across the whole drum (Figure 6.1a, bottom panel).

When illuminated, part of the light is reflected from the suspended membrane I_g, and interferes with the light that crossed the membrane and is reflected from the bottom of the cavity I_s. This interference is constructive or destructive depending on the illumination

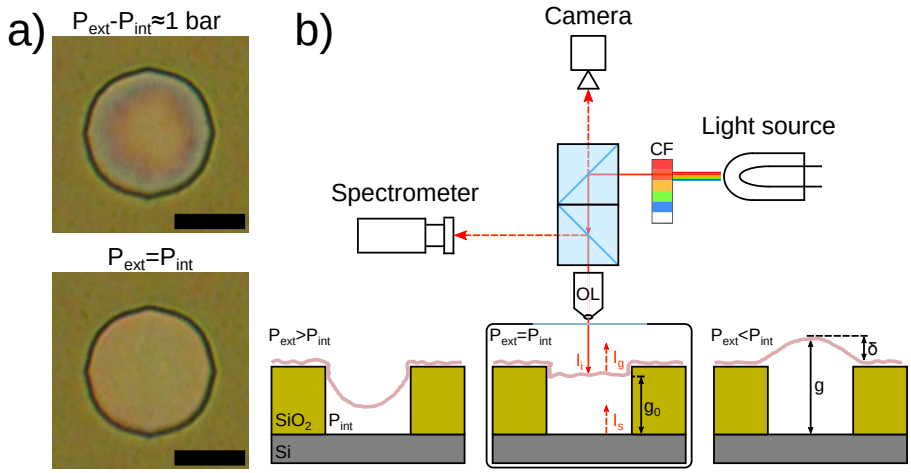

Figure 6.1: Newton's rings in a graphene drum and colorimetry setup. (a) Top: White light camera image of a downward deflected CVD double-layer graphene drum (13.2 μm in diameter) showing Newton's rings when the pressure difference between outside and inside the cavity is about 1 bar. Pressure-induced deflection of the drumhead changes the gap distance of the optical cavity radially. Bottom: After a certain time in an atmospheric environment, the cavity pressure is balanced and the drumhead is flat again, showing an homogeneous color. Scale bars are 10 μm. (b) Colorimetry setup: a customized optical microscope with a 100× objective lens (OL) and Köhler illumination is used for imaging the suspended graphene drum. White light from a Halogen lamp goes through a color filter (CF), and the intensity reflected from the drum I_g and the silicon substrate I_s is collected by a calibrated consumer camera and a spectrometer. Depending on the pressure difference, the drumhead bends downwards (left panel), remains flat (center panel) or bulges up (right panel).

wavelength and the distance separating the two surfaces. Since the absorption and internal reflections of the circular DLG membrane play a small role in the interference, the total reflected intensity for a given wavelength λ at a distance r from the center would be approximately $I(r) = I_g + I_s + 2\sqrt{I_g I_s}\cos\left(\frac{4\pi}{\lambda}(g_0 - \delta(r)) + \phi\right)$, where g_0 is the gap distance between the non-deflected membrane and the bottom of the cavity, $\delta(r)$ is the radial deflection, and ϕ is the phase change induced by the reflecting surfaces [177].

To fully exploit this phenomenon for fast mechanical and permeance characterization of suspended membranes, we use monochromatic illumination. For this purpose, a cost-effective customized optical microscope setup with Köhler illumination using a simple white light Halogen lamp (Thorlabs OSL2) as an effective multi-wavelength source is built as shown in Figure 6.1b. A consumer camera (Canon EOS 700D) collects the total reflected intensity from each point of the drum that is placed inside a vacuum chamber. Monochrome RAW images are taken at a particular wavelength by using color filters (FWHM 4-10 nm). Since consumer CMOS cameras apply an artificial compression to the received intensity values, the intensity values from the images are calibrated to correct for gamma compression [193]. First, we measure the intensity values reflected from the SiO_2 substrate for different illumination intensities by using neutral density filters to characterize the gamma factor. Fig-

ure 6.2 shows the power relation of the curves for three wavelengths, from which we obtain an average gamma of 0.4545 for all the wavelengths. Then, we compensate for the compression by applying a gamma correction

$$I = 255\left(\frac{I_{RAW}}{255}\right)^{2.2}. \tag{6.1}$$

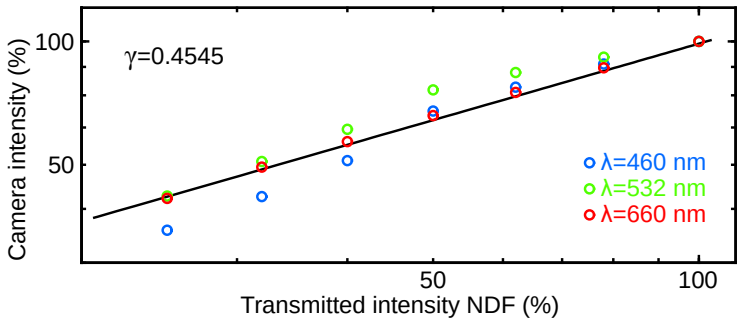

Figure 6.2: Gamma characterization.

6.2.1. RADIAL REFLECTANCE AND NEWTON'S RINGS

The reflectance of a certain image pixel is determined by applying $\mathscr{R} = \frac{I}{I_s}\mathscr{R}_s$, where $\mathscr{R}_s$ is the silicon reflectivity [177], and I_s is the reflected intensity measured from an uncovered circular cavity. This normalization also cancels the inhomogeneous spectral intensity of the source and eliminates the impact of changes in the illumination intensity over time.

The radial deflection function of a circular membrane with radius R can be approximated by the maximum deflection at the center δ_c multiplied by the profile function $f(r) = 1 - 0.9\frac{r^2}{R^2} - 0.1\frac{r^5}{R^5}$ [194]. Then, the reflectance as a function of r becomes

$$\mathscr{R}(r) \propto \cos\left(\frac{4\pi}{\lambda}\left(g_0 - \delta_c f(r)\right) + \phi\right) = \cos\left(\Omega f(r) + \phi'\right), \tag{6.2}$$

where $\Omega = -\frac{4\pi}{\lambda}\delta_c$ and $\phi' = \frac{4\pi}{\lambda}g_0 + \phi$ are the spatial frequency and phase of the Newton's rings. Therefore, $\mathscr{R}(r)$ depends on the wavelength and the maximum deflection. Figure 6.3a shows three monochromatic images of the drum for different wavelengths (λ=460 nm, 532 nm, and 660 nm) at $\Delta P \approx 1$ bar. Note that shorter wavelengths result in higher spatial frequency Ω. To improve the data analysis, especially for the short-wavelength noisy images, we take advantage of the centro-symmetry of the device and perform a radial average as shown in the figure for the corresponding monochromatic images. By fitting the radial-averaged reflectance to Equation 6.2, it is possible to obtain a value of Ω and hence δ_c. In the case of the Newton's rings in Figure 6.3, the extracted center deflection is δ_c=-262 nm.

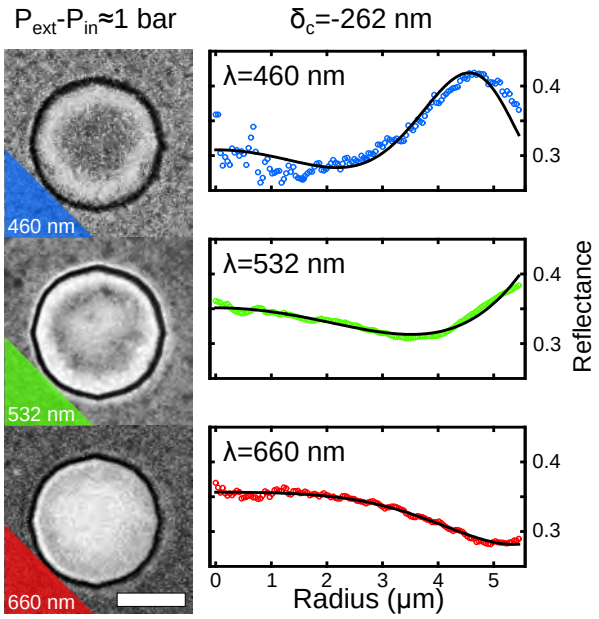

Figure 6.3: Radial reflectance across the drum. On the left, reflectance profiles for three wavelengths at the same pressure difference as in Figure 6.1a (top). Scale bar is 10 μm. On the right, the radial-averaged reflectance (circles) of the corresponding wavelengths. The Newton's rings fit (line) gives a center deflection value of δ_c=-262 nm.

6.2.2. NEWTON'S RINGS DURING A BULGE TEST

The Newton's rings fitting can be used to study the change in pressure-induced deflection with time, and therefore measure the permeance of the drum. Figure 6.4 shows the Newton's rings reflectance data fitted to Equation 6.2 for different deflections for both purging the air and filling the cavity (λ=532 nm).

The time-dependent maximum deflection as obtained for λ=532 nm illumination is shown in Figure 6.5 for both purging the air (top) and filling the cavity (bottom). We observe that the gas escapes from the cavity faster than when it has to fill it. As a technical remark, we also observe that the value of δ_c saturates around 70 nm due to the inaccuracy of fitting the data to Equation 6.2 in the limit of small deflections. To understand these rate differences we model the gas filling and purging of the cavity using the ideal gas law, and Hooke's law considering only the non-linear term for large deflections [121]. The molecular flux from/to the inside of the cavity at large deflections is

$$\frac{\mathrm{d}n}{\mathrm{d}t} = \frac{4bk_3\delta^3 + 3g_0k_3\delta^2 + AbP_{ext}}{RT}\frac{\mathrm{d}\delta}{\mathrm{d}t}, \tag{6.3}$$

with positive deflection when purging and negative deflection when filling, and where R is the universal gas constant, T=300 K is the temperature, k_3 is the nonlinear spring constant

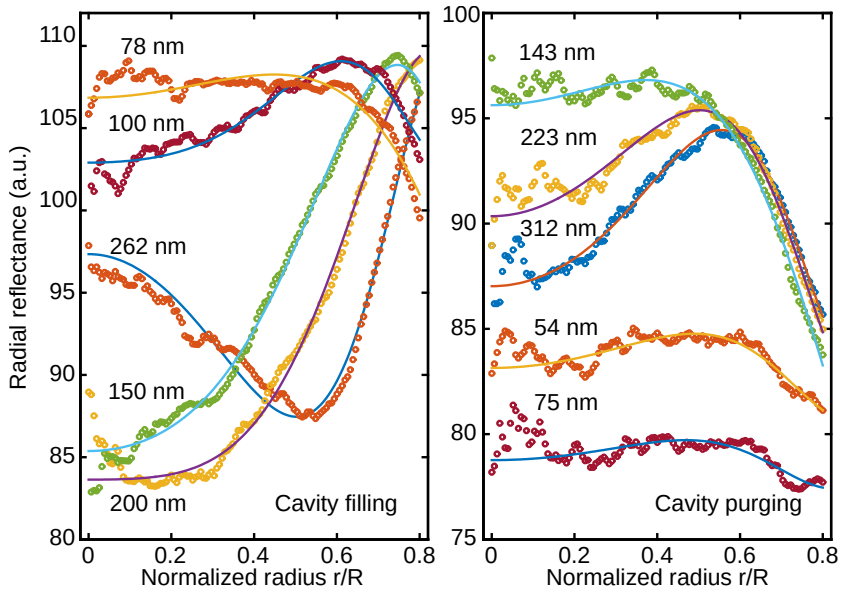

Figure 6.4: Newton's rings fitting for different deflections.

of the drum and A, its area; b is a geometric volume factor from the profile of a deflected circular membrane [183]. This volume factor originates from the volume of a membrane with a radial profile described by the membrane function $f(r) = 1 - 0.9\frac{r^2}{R^2} - 0.1\frac{r^5}{R^5}$:

$$V = \delta \int_0^{2\pi} \int_0^R \left(1 - 0.9\frac{r^2}{R^2} - 0.1\frac{r^5}{R^5}\right) r\,\mathrm{d}r\,\mathrm{d}\theta = \pi R^2\, 0.52\,\delta. \tag{6.4}$$

Therefore, $V = A\,b\,\delta$, where $A = \pi R^2$ and $b = 0.52$.

Equation 6.3 has two different solutions that depend on whether the drum is bulged upward or inward. Furthermore, the equation predicts that the molecular flux at large deflections depends on the external pressure: when the chamber is pumped ($P_{ext} \approx 0$), the gas escapes the drum cavity faster than when the chamber is vented ($P_{ext} \approx 1$ bar) and the cavity is slowly filled. This difference in behavior between purging and filling of the cavity is corroborated in Figure 6.5 qualitatively. For large deflections, By applying Fick's law of diffusion $\frac{\mathrm{d}n}{\mathrm{d}t} = -\mathscr{P} A \Delta P$ to Equation 6.3, and given $A\Delta P = k_3\delta^3$, we obtain:

$$\frac{\mathrm{d}\delta}{\mathrm{d}t} = \frac{\frac{-RT\mathscr{P}k_3}{A^2}}{4bk_3\delta^3 + 3g_0k_3\delta^2 + AbP_{ext}}. \tag{6.5}$$

Equation 6.5 can be numerically integrated to obtain the time evolution of a deflating membrane. The curves in Figure 6.6 are plotted for purging and filling for the measured Young's modulus by AFM $E = 420$ GPa ($k_3 = 0.84\,10^{14}$ N/m^3) for different permeance values.

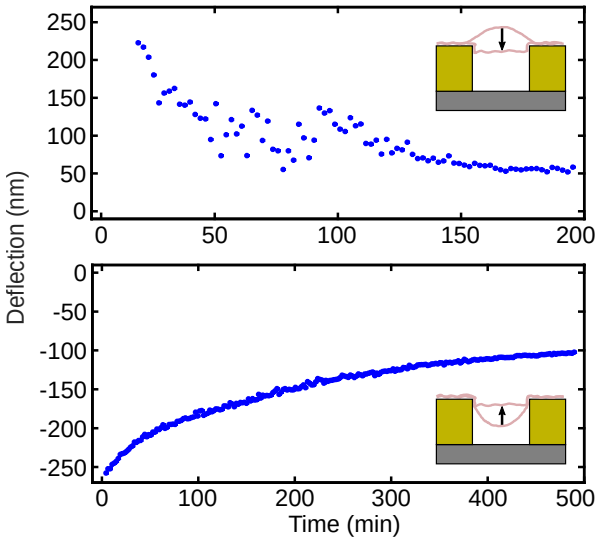

Figure 6.5: Time evolution of the deflection during purging and filling of the cavity. (a) The Newton's rings fitting is applied to a series of reflectance profiles of the same drum for λ=532 nm, resulting in the change of deflection while the drum returns to pressure balance (blue points). When the gas escapes the cavity (top), the deflection returns to zero faster than in when the gas fills the cavity (bottom). The fitting becomes inaccurate at small deflections.

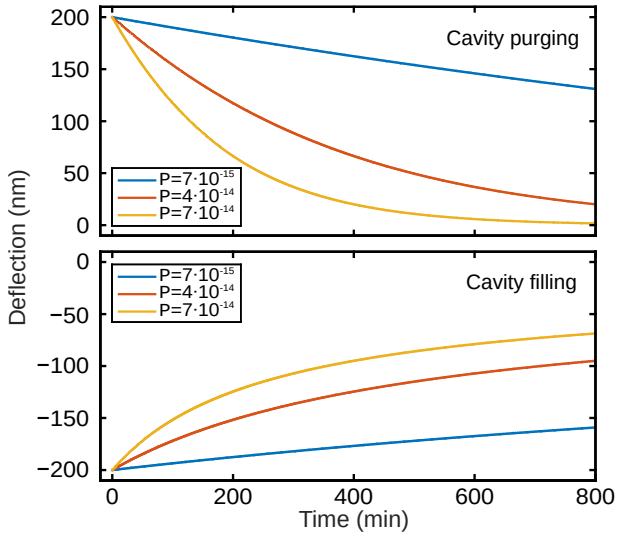

Figure 6.6: Simulated center deflection as a function of time for purging (top) and filling (bottom) experiments assuming a change of volume in the large deflection regime.

6.3. COLORIMETRY IN THE SMALL DEFLECTION REGIME

To extract the permeance quantitatively, we consider the small deflection limit. In this linear-deflection regime, the cavity volume can be assumed to be constant and the mechanical response of the drum is governed by its linear stiffness. Under these conditions the membrane deflection is given by a simple decaying exponential $\delta(t) = \delta_\infty + \delta_0 e^{-t/\tau}$ for both purging and filling, where $\tau = \frac{g_0}{\mathscr{P}RT}$ is the time constant of the system, $\mathscr{P}$ is the permeance of the membrane [195], and δ_∞, its position at rest which does not need to be zero due to side-wall adhesion [101, 106].

In addition, for small deflections, the drum reflectance averaged over its area $\mathscr{R}_{drum}$ is directly proportional to the deflection. The radial reflectance is

$$\mathscr{R}(r,t) \approx R_s + R_g + 2\sqrt{R_g R_s}\cos\left(\frac{4\pi}{\lambda}(g_0 - \delta(r,t)) + \phi\right) = R_s + R_g + 2\sqrt{R_g R_s}\cos(\Omega(t)\, f(r) + \phi'), \tag{6.6}$$

where $\Omega = -\frac{4\pi}{\lambda}\delta_c(t)$ and $\phi' = \frac{4\pi}{\lambda}g_0 + \phi$ are the spatial frequency and phase of a Newton ring. $f(r) = 1 - 0.9\frac{r^2}{R^2} - 0.1\frac{r^5}{R^5}$ is a profile function that can be approximated to $f(r) \approx 1 - \frac{r^2}{R^2}$ for small deflections. Then,

$$\mathscr{R}(r,t) \approx a + b\cos\left(-\frac{4\pi}{\lambda}\delta_c(t)\left(1 - \frac{r^2}{R^2}\right) + \phi'\right). \tag{6.7}$$

Taking the surface integral and using $r\mathrm{d}r = \frac{R^2}{2}\mathrm{d}\left(\frac{r^2}{R^2} - 1\right) = \frac{R^2}{2}\mathrm{d}X$

$$\begin{aligned}
\int_S \mathscr{R}(r,t)\, ds &= \int_0^{2\pi}\int_0^R \mathscr{R}(r,t)\, r\mathrm{d}r\mathrm{d}\theta \\
&\approx 2\pi\int_0^R \left[a + b\cos\left(\frac{4\pi}{\lambda}\delta_c(t)\left(\frac{r^2}{R^2} - 1\right) + \phi'\right)\right] r\mathrm{d}r \\
&\approx \pi R^2 a + \pi R^2 b\int_{-1}^0 \cos\left(\frac{4\pi}{\lambda}\delta_c(t)\, X + \phi'\right)\mathrm{d}X \\
&\approx \pi R^2 a + \pi R^2 b\frac{\lambda}{4\pi\delta_c(t)}\left[\sin(\phi') - \sin\left(\phi' - \frac{4\pi}{\lambda}\delta_c(t)\right)\right].
\end{aligned} \tag{6.8}$$

We can expand the second sine

$$\sin\left(\phi' - \frac{4\pi}{\lambda}\delta_c(t)\right) \approx \sin(\phi') - \frac{4\pi}{\lambda}\delta_c(t)\cos(\phi') - \frac{1}{2}\frac{4\pi}{\lambda}^2\delta_c^2(t)\sin(\phi'). \tag{6.9}$$

Therefore,

$$\begin{aligned}
\mathscr{R}_{drum}(t) &= a + b\frac{\lambda}{4\pi\delta_c(t)}\left(\sin(\phi') - \sin(\phi' - \frac{4\pi}{\lambda}\delta_c(t))\right) \\
&\approx a + b\frac{\lambda}{4\pi\delta_c(t)}\left(\frac{4\pi}{\lambda}\delta_c(t)\cos(\phi') + \frac{1}{2}\frac{4\pi}{\lambda}^2\delta_c^2(t)\sin(\phi')\right) \\
&\approx a + b\cos(\phi') + \frac{2\pi b}{\lambda}\sin(\phi')\delta_c(t).
\end{aligned} \tag{6.10}$$

For small deflections, we know that the change of deflection with pressure is a decaying exponential $\delta_c(t) = \delta_0\, e^{-t/\tau}$. Then,

$$\mathscr{R}_{drum}(t) \approx A + B\, e^{-t/\tau}, \tag{6.11}$$

where $A = a + b\cos(\phi')$, $B = \frac{2\pi b}{\lambda}\sin(\phi')\delta_0$, and δ_0 is the initial deflection in the linear regime.

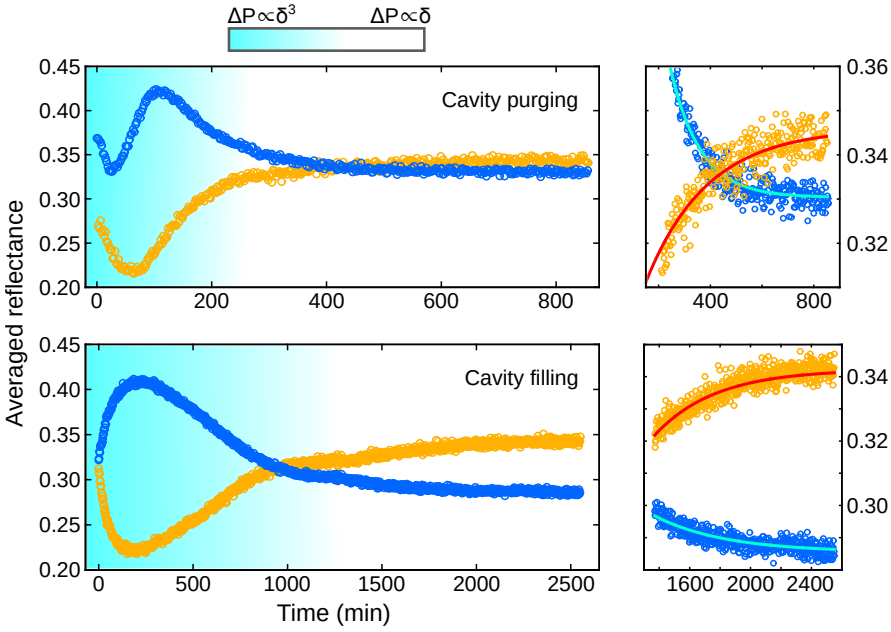

Figure 6.7: Change of drum averaged reflectance with time during purging and filling: time constant extraction. A simple exponential function is fitted to the linear-deflection regime of the drum averaged reflectance (blue circles for λ=460 nm and orange circles for λ=600 nm) to obtain the time constants of the drum when purging and filling (values showed in Table 6.1). The extracted time constants lead to a membrane permeance of around $1\times10^{-14}\,\frac{mol}{m^2 s\cdot Pa}$.

6.3.1. CHANGE OF DRUM AVERAGED REFLECTANCE WITH TIME

The drum averaged reflectance is shown in Figure 6.7 for two wavelengths, 460 nm (blue circles) and 600 nm (orange circles), for both cavity filling and purging. As the large deformation regime subsides after 200 minutes for the purging experiment and 1000 minutes for the filling experiment, the reflectance in the linear regime decays exponentially with time. This part of the curves is then fitted to obtain the time constant of the drum. The fitted time constants and the inferred permeance values are summarized in Table 6.1 for different wavelengths for the two experiments. It is worth noting that the drum's reflectance decays to different values in the case of the purging and the filling experiments as can be seen in Figure 6.7. The shift in the reflectance of the drum at rest could be an indication of the presence of side-wall adhesion or slack that changes the effective cavity depth.

	Filling		Purging	
Wavelength (nm)	τ (min)	$\mathscr{P}$ ($10^{-14}\frac{mol}{m^2 s \cdot Pa}$)	τ (min)	$\mathscr{P}$ ($10^{-14}\frac{mol}{m^2 s \cdot Pa}$)
460	446	0.87	125	3.12
532	653	0.60	125	3.12
600	519	0.75	237	1.65
633	573	0.68	6294	0.06
660	570	0.69	565	0.69
AFM	1914	0.20	630	0.62

Table 6.1: Values of time constants and permeances.

6.4. COMPARISON TO AFM MEASUREMENTS

To compare the permeance values and the purging/venting difference, and validate the colorimetry technique we repeated the experiments to measure the deflection with a calibrated atomic force microscope (Bruker Fastscan, Scanassyst-Fluid tip). By using the Quantitative NanoMechanics mode (QNM) that allows a direct control of the maximum force applied to the substrate (Peak Force mode), we were able to image the height and extract the deformation of the suspended circular membrane of 13.2 μm in diameter at 5 nN (Figure 6.8). Figure 6.9 shows the drum average deflection data for the purging (top) and filling (bottom) cases. Notice that the values of drum average deflection are a factor 0.52 from the actual deflection values at the center of the drum. Note that in the filling experiment we followed the same procedure as in the colorimetry technique (sample was left several days in a desiccator and moved to the AFM), while for the purging experiment we left the sample in an pressurized chamber at 2 bar for several days, hence having a positive pressure difference of 1 bar once returned to atmospheric pressure for AFM measurements.

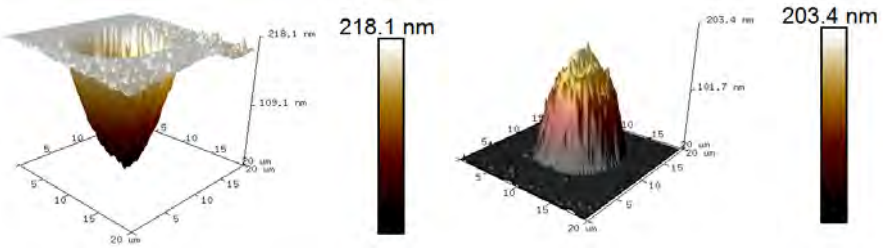

Figure 6.8: 3D AFM height image of the drum at the beginning of the filling (left) and purging (right) experiments.

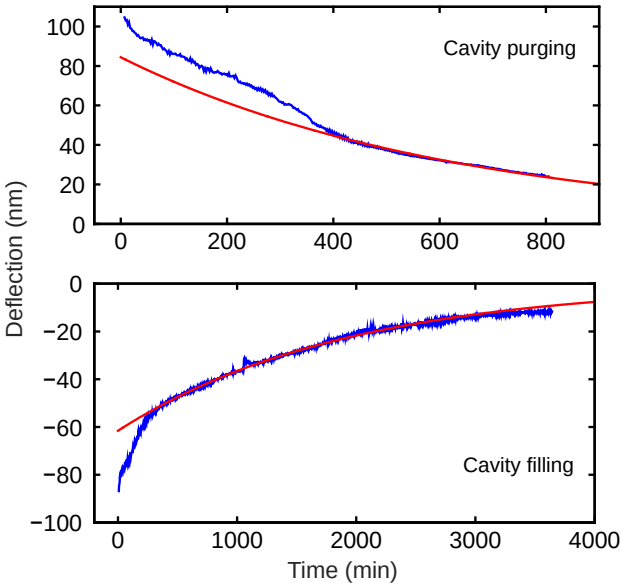

Figure 6.9: Drum averaged deflection for purging (top) and filling (bottom) experiments.

We also measured the roughness of the graphene-SiO_2 substrate in the surroundings of the drum. The R_a value obtained in an area free of wrinkles at the edge of the drum is 0.3 nm, which is basically the roughness of the thermally-grown SiO_2. We also measured the roughness including wrinkles in the surroundings of the drum in question, and we read a R_a value of 2.2 nm. The gas permeation could happen through the interface, especially with the presence of wrinkles. However, we should not discard other diffusion channels such as the oxide and the material itself.

6.5. DISCUSSION

Air diffusion could be taking place through the graphene material, although we cannot discard the interface and oxide as diffusion channels. Further studies must be done to determine the actual diffusion channel/s on these systems. The permeance for the DLG membrane is calculated to be $(0.71 \pm 0.10)10^{-14} \frac{mol}{m^2 s \cdot Pa}$ from the filling data, and $(1.43 \pm 1.39)10^{-14} \frac{mol}{m^2 s \cdot Pa}$ from the purging data, which are two to three orders of magnitude higher than the permeance measured in pristine BLG [121]. The spread in permeance values in Table 6.1 is larger in the purging experiment than in the filling case due to illumination difficulties that happen during the purging experiment and inaccuracies in the exponential fitting that can be large for certain wavelengths. Measurements performed by AFM yield similar permeance values and they unexpectedly show different values between filling and purging even in the small deflection regime. This discrepancy between purging and filling at small deflections is an indication that extra diffusion channels such as the graphene-oxide

interface play a role in gas permeation.

The difference between purging and filling the cavity arising from the difference of molecular flux at large deflections is reproducible, which bring us to the conclusion that the change in volume of these ultrathin microdrums cannot be ignored. The effect becomes strong when the membranes are deflected beyond the linear regime, which is usually the case when performing AFM nanoindentation or pressure studies. To extend these conclusions to other drums and study the dependence with their diameter, we can apply the colorimetry technique to hundreds of drums.

6.6. CONCLUSIONS

This study has presented the colorimetry technique as a scalable tool to characterize the mechanical properties and the permeance of suspended graphene microdevices. This non-invasive optical technique allows to extract the evolution of a thin membrane deflection with time when filling and emptying the microcavity with air. We observe the linear- and nonlinear-deflection regimes, and we find that the gas filling process is slower than the gas purging in the case of large deflection, where volume change is not negligible. Furthermore, we use small deflection measurements to extract the permeance of a double-layer CVD graphene membrane, finding that it is about two to three orders of magnitude higher than pristine BLG. Ultimately, the colorimetry technique could be employed to characterize the mechanical properties of suspended SLG and other 2D materials by using the right combination of cavity depth and wavelength. The parallelization of data acquisition by image processing tools combined with a controlled deformation of the membranes would allow the fast characterization of large arrays of these mechanical systems at once limited only by the resolution of the optical instrument, and could lead to the realization of interferometric modulator displays (IMOD) made out of graphene.

KILLER APPLICATION: CVD GRAPHENE FOR INTERFEROMETRY MODULATION DISPLAYS (IMOD)

7

GRAPHENE INTERFEROMETRY MODULATION DISPLAY

Right action is better than knowledge;
but in order to do what is right,
we must know what is right.

Charles I (Charlemagne), Holy Roman Emperor,
King of the Franks and King of the Lombards.

While a boss shouts the direction from a seat,
a leader joins the crowd to show the way.

Santiago, Delft 2016

In this work we study the optical response of electrically actuated graphene drumheads, and demonstrate their potential for use as pixels in a Graphene Interferometry Modulation Display (GIMOD). An electro-optical model that predicts the spectral response of the membrane as a function of the electrostatic pulling is presented and verified experimentally with a spectrometer. Furthermore, we apply stroboscopic illumination in order to observe membrane deflections at large actuation rates concluding that gas compression does not play a significant role for frequencies up to 400 Hz. The reliability and speed of these membranes in producing the desired electro-optic modulation makes them suitable as pixels for high refresh rate displays. As an example, we demonstrate the use of 5 μm in diameter devices to make a GIMOD prototype with 2500 pixels per inch that would correspond to a $5''$ *display with a resolution of 12K.*

7.1. INTRODUCTION

Graphene, the carbon monolayer and 2D allotrope of graphite, has the potential to impact technology and promises a wide range of applications with its exceptional properties [42, 43, 44]. According to the roadmap of the Graphene Flagship [62], it is expected to arrive in a span of 10 years to the markets [61, 63] although this would not be possible without characterization tools for the standardization of the material and graphene-based products.

A promising means for industrial scale production of graphene and other 2D materials is the use of the chemical vapor deposition (CVD) technique on catalytic foils such as copper [64, 65], nickel [66] or germanium [67]. However, CVD single-layer graphene (SLG) is usually produced with defects [116], which weakens its mechanical properties when compared to that of exfoliated from graphite [114, 115]. Furthermore, in order to create graphene MEMS/NEMS devices the material needs to be transferred from the growth substrate onto a substrate containing cavities and trenches, a process that remains challenging and that tends to cause low device yield [154] and large spread in the mechanical properties of the suspended devices from the same chip, in particular their built-in tension (Cartamil-Bueno et al 2018, in preparation).

Statistical studies on the mechanical properties of CVD SLG drumheads with laser interferometry [105, 111], Raman spectroscopy [106, 112, 113], and atomic force microscopy [114, 115] have been reported, although only recent advances in the visualization of graphene membranes with an optical microscope have allowed rapid characterization of large numbers of devices (Chapters 5 and 6 of this thesis). This progress was possible after the observation of color variations in deflected membranes made out of CVD double-layer graphene (DLG) that happens because of the larger absorption of light when stacking several layers [153]. However, the change of color in graphene membranes has only been observed upon the application of gas pressure differences, and more time-effective techniques should be developed for the characterization and commercialization of graphene MEMS.

Electrostatic transduction is used extensively as an actuation mechanism for MEMS devices, including graphene nanoelectromechanical structures [108, 196]. In contrast, here we investigate the far-from-resonance, quasi-static, large deformation regimes of graphene [197, 198]. It is anticipated that the gas trapped in graphene-sealed cavities may have a non-negligible effect on the electrostatic actuation which merits investigation [179, 199]. The optical modulation effect resulting from the absorption and interference of light from the graphene and the silicon back mirror is also a well-known technique used to detect small amplitude deformation of vibrating graphene membranes [190]. This optical modulation effect is mostly investigated in the regime of weak intensity modulation, and it is only recently that attention has been given to the large area optical behavior of highly deformed graphene membranes [153, 192].

Unlike other 2D materials-based electro-optic modulators that rely on electronic, plasmonic, or band gap tuning effects [200, 201], electromechanical-based optical modulators are capable of a significantly wider tuning range albeit at a lower rate. This makes these devices ideal for display technologies as have been demonstrated previously using silicon nitride structures to create an Interferometric Modulation Display (IMOD) [202]. Graphene

can take such an approach to its technological limits by implementing the concept using the ultimate electromechanical structures.

Here, we report the electro-optical response of graphene mechanical pixels by measuring the change in wavelength-dependent reflectivity of a suspended graphene drum as a function of electrical gating. We use a spectrometer to measure the wavelength spectrum at different voltages, and find a matching correspondence with a simple model based on light interference. Moreover, to verify that gas compression effects do not play an important role, we use a stroboscopic illumination technique to study the electro-optic response of these graphene pixels at frequencies up to 400 Hz. Based on these findings, we demonstrate a continuous full-spectrum reflective-type pixel technology with a Graphene Interferometry MOdulation Display (GIMOD) prototype of 2500 pixels per inch (ppi) equivalent to 12K resolution.

7.2. FABRICATION AND SETUP

Circular cavities are etched through thermally-grown SiO_2 layers (300 to 1180 nm in depth depending on the sample) on silicon substrates by means of reactive-ion etching. DLG layers, fabricated by stacking two CVD SLG graphene layers, are transferred onto the patterned substrate using a semi-dry transfer technique. This results in an optical cavity with a movable absorbing membrane made out of CVD DLG, and a fixed mirror formed by the underlying silicon surface. The silicon substrate equally plays the role of back electrode for electrostatic actuation. We use DLG membranes because of their higher yield [154] and their larger absorption in the visible spectrum than that of SLG.

The colorimetry setup used in this work consists of an optical microscope with Köhler illumination, a 20× apochromatic objective lens, and a Halogen lamp as a multi-wavelength light source. Light reflected from the sample is split into a calibrated consumer camera and a spectrometer. The spectrometer is placed in such a way as to collect light from a circular area that is nearly equivalent in dimensions to that of the studied drums. A series of 5-10 nm linewidth color filters with wavelengths ranging from 450 nm to 650 nm are mounted on a motorized computer-controlled wheel, and placed in front of the camera imager as shown schematically in Figure 7.1a.

Electrostatic actuation of the graphene drums is achieved by using a computer controlled DC source, where the silicon substrate is grounded. For these measurements a sample with 1180 nm oxide thickness was chosen, the capacitance of the roughly 1 cm^2 in area graphene/SiO_2/Si structure was measured to be 0.6 nF. For the stroboscopic measurements, the spectrometer and Halogen lamp are removed as they are not capable of operating at the required frequencies. A white LED is used for illumination, while a waveform generator is used as signal source. The dual channel generator outputs a narrow ($\frac{1}{72}$ of the actuation period) 5 V pulse to the LED, this illumination pulse is phase-locked to an actuation sine wave necessary to perform stroboscopic imaging.

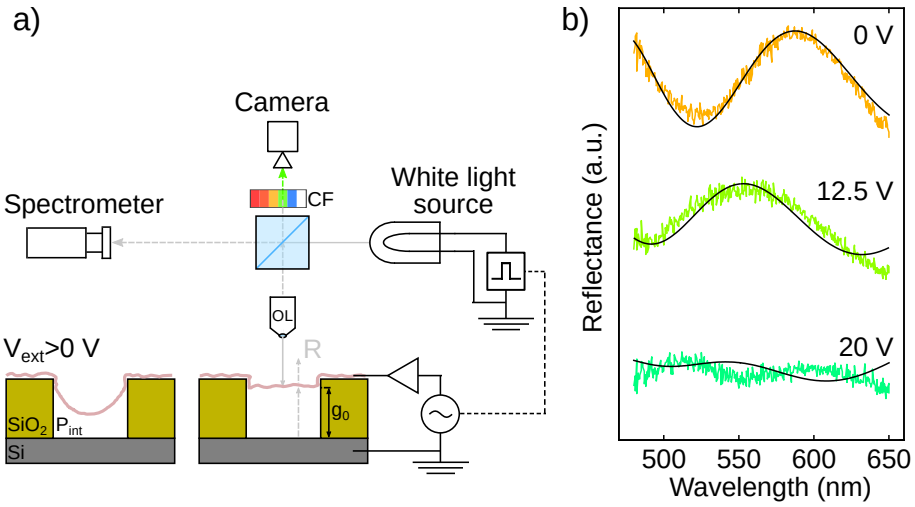

Figure 7.1: Electro-optical measurements with a colorimetry setup of a graphene drumhead of 20 μm in diameter. a) A suspended CVD DLG membrane can be pulled electrostatically while its reflectance spectrum is measured with a spectrometer and a calibrated camera. The white light illumination could be either a halogen lamp (for spectral studies) or a white LED synchronized to the membrane electrical control (for stroboscopic studies). b) At different voltages, the reflectance spectrum peak of the overall membrane shifts from 580 nm to 510 nm in a controlled and reproducible manner.

7.3. RESULTS

We start our investigation with the application of a voltage ramp going from 0 to 20 V and back to 0 V with steps of 0.25 V, after the application of each step the voltage is left constant for a period of 30 s before acquiring the data. As the voltage is ramped up we observe a shift in the peak of the spectrum of 70 nm for 20 V occurring for a wavelength of 580 nm. Figure 7.1b shows the shift in the spectrum between 0 V and 20 V: the overall color of the drumhead changes as a function of voltage going from orange ($\lambda = 580$ nm) at 0 V to green ($\lambda = 550$ nm at 12.5 V and $\lambda = 510$ nm at 20 V).

The electro-optic response of the graphene drums also allows us to extract key physical parameters. To do so, we apply a 1 degree of freedom model where assuming a perfect membrane behavior, i.e. no plate bending stiffness, we consider the drum's deflection under the effect of an electrostatic force to be axisymmetric and having a parabolic profile given by $\delta(r/a) = \delta_c(1 - r^2/a^2)$. Here, $\delta(r/a)$ is the deflection of the drum at a radial distance r from the center of the drum, a is the drum's radius, and δ_c is the center deflection of the drum. The electrostatic force due to an applied potential difference V can be obtained by differentiating the electrostatic energy, $E_{elec} = \frac{1}{2}C_{drum}V^2$, with respect to displacement, where the drum's capacitance C_{drum} is calculated based on the assumed deflection shape. Thus the expression for electrostatic force is approximated as:

$$F_{elec} = \frac{-C_0 V^2}{2g}\left(\frac{\bar{\delta} - (\bar{\delta}-1)ln(1-\bar{\delta})}{(\bar{\delta}-1)\bar{\delta}^2}\right), \tag{7.1}$$

where C_0 is the capacitance of the undeformed drum, and $\bar{\delta}$ is the normalized deflection at the center of the drum, i.e. $\bar{\delta} = \delta_c/g$, and g is the cavity depth (Cartamil-Bueno et al. 2018, in preparation). The deflection of the graphene membrane, if the perfect hermeticity assumption is to be maintained, requires that the force balance equation accounts for the hydrostatic pressure that develops from the compression of the gas trapped within the cavity and cannot escape it. Thus, the equilibrium position equation that accounts for linear and nonlinear stiffness, gas compression, and electrostatic force is given in a non-dimensional form as equation 7.1:

$$\bar{\delta} + \bar{k_3}\bar{\delta}^3 + \beta\frac{\bar{\delta}/2}{1-\bar{\delta}/2} = \frac{-\bar{V}^2}{2}\left(\frac{\bar{\delta} - (\bar{\delta}-1)ln(1-\bar{\delta})}{(\bar{\delta}-1)\bar{\delta}^2}\right), \tag{7.2}$$

where $\bar{k_3} = \frac{k_3 g^2}{k_1}$ and $\bar{V} = \sqrt{\frac{V^2 C_0}{k_1 g}}$ are the non-dimensional nonlinear stiffness and non-dimensional voltage, respectively, and $\bar{\beta}$ is a non-dimensional constant that depends on cavity volume and initial pressure. The optical reflectivity model on the other hand neglects any cavity effects and treats the suspended drum as an absorbing layer placed in front of the silicon back mirror. This simplification is valid for thin graphene membranes, less than 5 layers [203], and leads to the following drum reflectance:

$$R(r,\lambda) = A(\lambda) + B(\lambda)\cos(-\pi\bar{X}(r) + \phi), \qquad \text{for } \bar{X}(r) = \frac{4g\bar{\delta}(r)}{\lambda} \tag{7.3}$$

where λ is the wavelength, $A(\lambda)$ and $B(\lambda)$ are wavelength dependent constants, and $\phi = \frac{4\pi g}{\lambda} + \phi'$ is a phase shift induced by the optical travel path and by the graphene. Taking nominal values for the optical properties of graphene [177], we can neglect ϕ' as it is negligibly small compared to the travel path term. To obtain the optical response as perceived by the spectrometer we average the reflectivity over the entire drum, thus re-expressing equation 7.3 only in terms of the center deflection as:

$$R_{avg}(\lambda) = A(\lambda) + \frac{B(\lambda)}{\pi\bar{X}}\left[\sin(\phi) - \sin(\phi - \pi\bar{X})\right]. \tag{7.4}$$

7.4. DEFLECTION-VOLTAGE CURVES

The electro-optic response of a suspended 20 μm in diameter graphene drum, i.e. the drum averaged reflectance as a function of voltage, is shown in Figure 7.2a as obtained from the camera and spectrometer for the 550 nm wavelength. Using equation 7.4, we fit a value of

deflection, and plot the deflection vs. voltage in Figure 7.2b. The deflection curves from both camera and spectrometer agree well, although the camera fit is done on collected data from a narrow wavelength band (corresponding to that of the filter) while the spectrometer fit is done on the same wavelength range selected from the 475-700 nm spectral band. It is worth noting that the fits are insensitive to small deflections and thus to low actuation voltages.

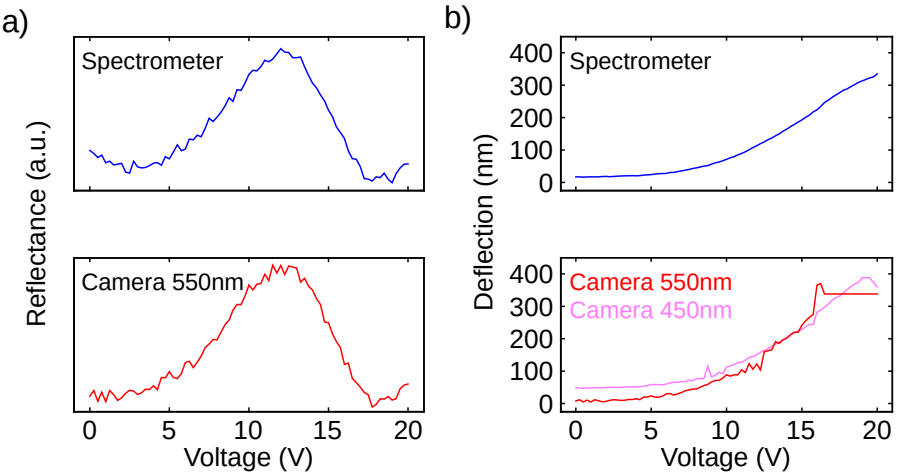

Figure 7.2: Conversion from reflectance-voltage curves to deflection-voltage curves for $\lambda = 550$ nm. a) The optical response in that selected wavelength from the spectrometer measurements (top panel) and color-filtered camera images (bottom panel) show the same trend. b) By fitting the reflectance curves with equation 7.4, we obtain the corresponding deflections as a function of applied voltage, which agree well for both types of measurements. A maximum deflection of 350-400 nm is obtained for this membrane (same device as in Figure 7.1).

7.5. STROBOSCOPIC MEASUREMENT

Had the graphene drum in question been fully hermetic, then the gas pressure as described in equation 7.2 would have prevented the structure from such a large deformation (gas stiffens is expected to be around 100 times that of the linear stiffness of the drum). This indicates that the graphene membrane has a permeation time constant that is below the 30 s settling time used for these measurements. If the permeation time constant is small, one could imagine that gas compression effects could alter the response of the membrane when pulling them at sufficiently high frequencies.

We investigate the possibility of a squeeze-film like response by substituting the halogen lamp with a white LED, which is powered by short duration pulses that are synchronized to a sinusoidal actuation voltage: $V_{act} = (17.5 + 2.5\sin(\omega_{act}t + \phi_{act}))$ V. By sweeping the phase difference between the illuminating pulse and the actuation signal we are able to reconstruct the time-domain response of the structure. An example is shown in Figure 7.3a where we see two snapshots of a 15 μm drumhead at opposing phases in the actuation cycle.

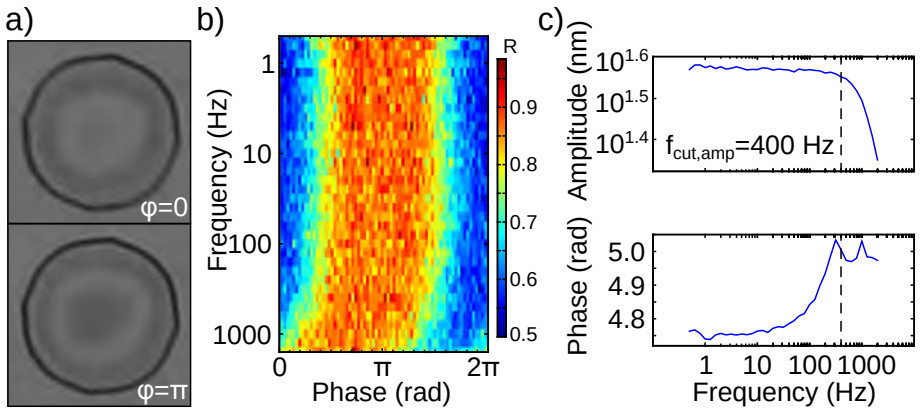

Figure 7.3: Stroboscopic measurement. a) Optical microscope image of a 15 μm in diameter drum at two opposite phases of vibration ($\phi = 0$ top, $\phi = \pi$ bottom) while actuated at 1 kHz. b) Colormap of the reflectance at the center of the same drum as a function of frequency and phase. A phase delay intrinsic to the signal amplifier is observed. c) Bode plots of amplitude and phase of the drum, showing that the response is flat up to 400 Hz (cutoff frequency of amplifier).

We stroboscopically measure 5 drums of 15 μm in diameter with actuation frequencies ranging from 0.5 to 2000 Hz. The measured structures do not exhibit a first-order response indicative of squeeze-film effect for frequencies up to 400 Hz, beyond which the cut-off frequency of the capacitively loaded amplifier (Physik Instrumente E660) is reached. The frequency response bode-plots are shown in Figure 7.3b, the lack of a first-order response indicates that the permeation time constants are below or above the measurement range depending on the drumhead in question. A bode plot fit of the displacement amplitude and phase are shown in Figure 7.3c, demonstrating no special feature until the amplifier cut-off.

7.6. GIMOD

The large electro-optic modulation and lack of mechanical delays at high frequencies make these devices interesting candidates for display applications beyond the flicker fusion threshold that require color reliability in the millisecond range such as virtual or augmented reality (VR/AR) [204]. Figure 7.4a-b shows a ~2500 ppi Graphene Interferometry MOdulation Display (GIMOD) prototype. The static image displaying the Graphene Flagship logo blinks across colors upon the application of a sinusoidal signal. All the mechanical pixels of 5 μm in diameter are addressed at once with the silicon substrate acting as a back gate. The pixel aperture -active to total area ratio- is ~50%, causing a contrast of about 1:2 due to the large separation between pixels (pixel pitch about double of the pixel size). The panels on the middle show a zoom-in of some pixels when they are actuated with 30 V (yellow state when OFF, top panel; blue state when ON, bottom panel).

By analyzing the RGB channels of one of the pixels, we obtain its average gamut and its evolution upon applied voltage. Figure 7.5 shows the pixel trajectory over a standard RGB

(sRGB) color map based on CIE1931 colorimetry [205]. From the map we can qualitatively corroborate the electro-optical modulation from yellow to blue of these pixels.

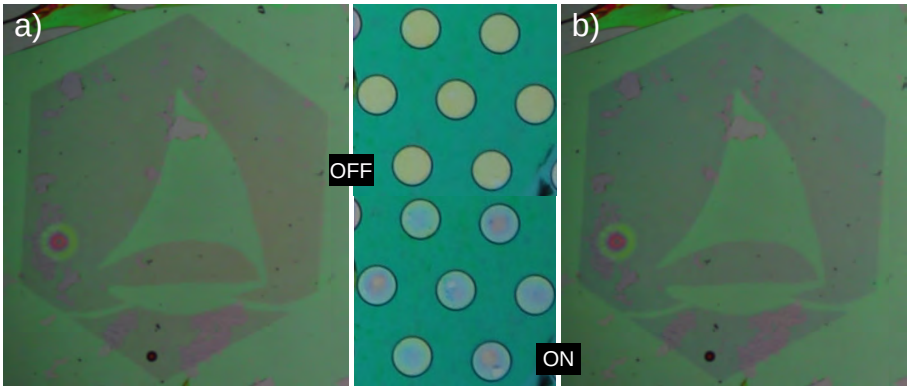

Figure 7.4: Graphene Interferometry MOdulation Display (GIMOD) prototype showing the logo of the Graphene Flagship. The graphene mechanical devices are used as continuous-spectrum pixels of 5 μm in diameter, hence resulting in a reflective-type display of 2500 pixels per inch (ppi), equivalent to 12K resolution for a display of 5″. a) GIMOD prototype OFF, with pixels showing a yellow color. b) GIMOD prototype ON, with pixels in a blue state.

7.7. DISCUSSION

The electrical control of devices in large arrays of NEMS can be affected by the fabrication yield when they are meant to be actuated capacitively. Reducing the pixel size and increasing the cavity depth guarantees a higher survival rate of the membranes as reported previously [154]. We have observed that the contact of the membranes with the bottom of their cavities causes an immediate device failure: either by sudden tearing of the membrane or by their permanent sticking to the silicon floor. To avoid ohmic leakage and loss of the voltage reference, we chose deep cavities of 1180 nm that prevents the formation of stuck membranes that could short-circuit the entire sample. However, these parameters are a trade-off with other factors such as the nonlinear spring constant k_3 and the actuation voltage range for a given maximum deflection. A graphene mechanical pixel would have to be optimized taking all this into consideration.

The transfer of graphene onto cavities introduces a spread in tension in addition to a significant spread in permeability (Cartamil-Bueno et al. 2018, in preparation). Since to act as efficient electro-optic modulators the drums have to be highly deflected over a large range to capture all wavelengths, their mechanical response will be dominated by their nonlinear stiffness rendering the initial spread in built-in tension of secondary importance. On the other hand, the spread in gas permeability is a more important issue that requires controlling the membrane's permeation time constant. This is possible to achieve by purposely damaging the drums with a post-transfer UV oxidation step to induce pore formation and significantly increase the permeability of the membrane [206].

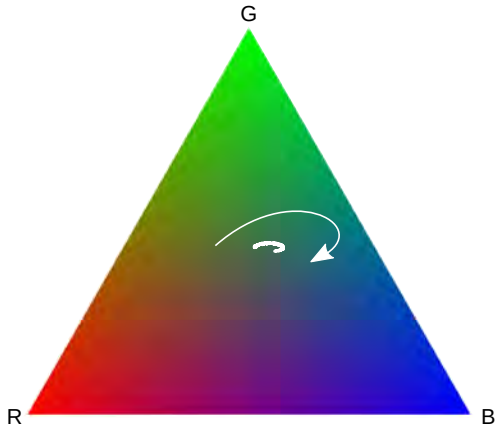

Figure 7.5: Gamut pixel trajectory of the average reflectance of a GIMOD prototype with pixels of 5 mum in diameter. The change of pixel color as a function of voltage, whose direction is pointed with an arrow, is displayed in the sRGB color triangle (subset of x,y chromaticity space) based on CIE1931 colorimetry.

7.8. CONCLUSIONS

In summary, we report on CVD double-layer graphene electromechanical electro-optic modulators, the characterization of their spectral response, and their application as pixels in a Graphene Interferometry MOdulation Display (GIMOD). In addition to observing the electro-optical modulation, we develop an electrostatic-optical model to describe their behavior. We use the reflectance-voltage plots to fit a deflection-voltage response and conclude that a device is not significantly hermetic. We further explored the permeation time constants by stroboscopically measuring 5 devices without finding the onset of squeeze-film effect due to the gas trapped in the cavity in the frequency range of 0.5 to 400 Hz.

The large color modulation and good frequency response of these graphene electro-optic modulators in ambient conditions enable the use of these mechanical devices as pixels with color reliability at high refresh rates. This application is demonstrated with a 0.5″ prototype with 2500 ppi that would equate to a 5″ display with 12K resolution.

Beside possibly eliminating the motion sickness in VR/AR applications, such a reflective-type (e-paper) pixel technology would greatly reduce power consumption as it is an interferometry modulation display (IMOD) technology. The use of graphene allows the large deformation of small membranes without mechanical failure or hysteresis allowing the fabrication of diffraction-limited devices for ultra-high resolution displays. Moreover, by using different voltages to actuate the pixels, each device is able to generate natural colors in the full-spectrum and in a continuous manner. This eliminates the need of RGB subpixels and reduces the addressing bandwidth to only one channel, with the consequential reduction of lower power consumption.

FUTURE APPLICATIONS

8

FUTURE APPLICATIONS

Plus Ultra.

Charles V, Holy Roman Emperor of German Nation, King of the Romans,
King of Italy, King of Spain and Lord of the Netherlands.

To Infinity and Beyond.

Santiago (quoting Buzz Lightyear in *Toy Story* by John Lasseter), Delft 2017

With this chapter, I conclude the thesis by presenting promising but unfinished work that shall be continued in the future. Here, I explain three directions for understanding and applying freestanding 2D materials. A conservative approach to the study of graphene membranes for pressure and gas sensing would use the colorimetry technique to perform further statistical studies beyond the fabrication yield. A more liberal prospect would involve the test of different types of cavity structures or geometries and different substrate materials that could lead to smarter sensors. And a radical change in the field should go through the abandonment of cavity-type structures and the direct study of the mechanical and optical properties without interference effects. This later path would not use 2D membranes for the creation of gas or pressure sensors –in principle– but for light applications such as radiation pressure propulsion for solar sailing in spacecrafts.

8.1. INTRODUCTION

Evolution is the result of the fractal-development of complexity in living forms when one branch is more efficient (i.e., that resists less to the pass of time, similarly to how a lightening branches looking for ground) [207, 208, 209, 210, 211]. In the last millennia, human civilizations have evolved from an original common past –possibly–, not always with interactions between each other and yet they followed similar developments to reach similar states.

Society development always required the skill of agriculture for horticultivation which was preceded by land research. Old cultures in the Americas such as native American culture from the Poverty Point or later the Incas at Moray (Peru) created concentric circular earthworks to understand and optimize their crops. Similarly, the Greeks and Romans built amphitheaters for the contemplation of an activity or entertainment, and even nowadays we continue using the same approach in public events like sport stadiums or cinemas.

Biological evolution is only one of the complexity branches of matter, possibly a more dynamical one from our time-limited human view, but that does not mean that inorganic matter cannot evolve. However, to speed up the process we can manipulate it to artificially give it a desired shape for a particular application.

8.2. BEYOND CIRCULAR CAVITIES: MORAY/COLOSSEUM CAVITIES

Graphene was isolated in 2004 from a process point of view [45], although its isolation from a substrate was demonstrated in 2007 when suspended in SiO_2 trenches [108] and TEM grids [102]. Graphene MEMS with a beam shape were found to dissipate energy when moving due to spurious vibrational modes [212], and soon this was solved by suspending graphene on circular cavities to have a full clamping [105]. Despite this improvement, the dissipation of these fully-clamped membranes is too high for sensing applications as the quality factor needs to increase from the usual 100-2000 at room temperature to 10^7. Unfortunately, there has been little progress on solving this issue since 2012 [111, 155].

Much is speculated in terms wrinkling [213] or slippage [120, 154] and there are studies on cross-mode energy transfer in graphene membranes [212, 214], although little effort has been put to study a more obvious, less exotic and possibly more dominant effect: the adhesion of the membrane when enters into contact with its immediate environment, i.e. the edges of its cavity. Understanding how exactly a drumhead membrane behaves and interacts with the sidewall of its cavity [101, 158], would throw light on the low quality factors. However, the nature of the membrane-sidewall should be investigated with custom tests that tackle that relationship alone. The circular devices have been studied to extenuation with no clear conclusions, and maybe it is time to look at the past and think what change has been done in similar situations to overcome a crisis.

In the flourishing of a civilization, many cultures realized artificial arrangements of land to create microclimates that could help them to optimize (and maybe understand) the cul-

The work in Section 8.2 is done by Santiago J. Cartamil-Bueno (structure design and experiment concept, graphene transfer and measurements) and Niels Lakens (EBID fabrication and measurements) in collaboration with Prof. Hagen's group.

tivation of crops. We learn now from the Moray ruins of the Inca Empire, in particular, that they dug concentric circular terraces to experiment with agriculture of potatoes and other vegetables [215, 216]. Due to the disposition of the ring depressions with respect to sun and wind and given their design in terms of depth and width, each of the terraced floors provided a different environment for the cultivation (different humidity levels and temperature variations of up to 15 K). Similarly to the Incas, and given the information exhaust from circular cavities with non-stepped sidewalls, we can create Moray structures sealed with graphene and use the colorimetry technique to contemplate the amount of sidewall length, adhesion and delamination energies, and pressure and temperature effects on the previous.

8.2.1. PRELIMINARY RESULTS

The electron beam induced deposition (EBID) technique enables the creation of customized microstructures with nanometer precision. We designed a Moray cavity with terraces of different step heights and plateau widths that allow us to extract information of the membrane to be deposited by only looking at it under the optical microscope.

Because large EBID structures require long writing times, we opted for building a Colosseum-looking cavity (similar to Moray-type, but without a terrace in the upper level) as a first approach. Then, we transferred a ~10-layer graphene flake on top of 4 of the Colosseum cavities with the viscoelastic transfer technique [125].

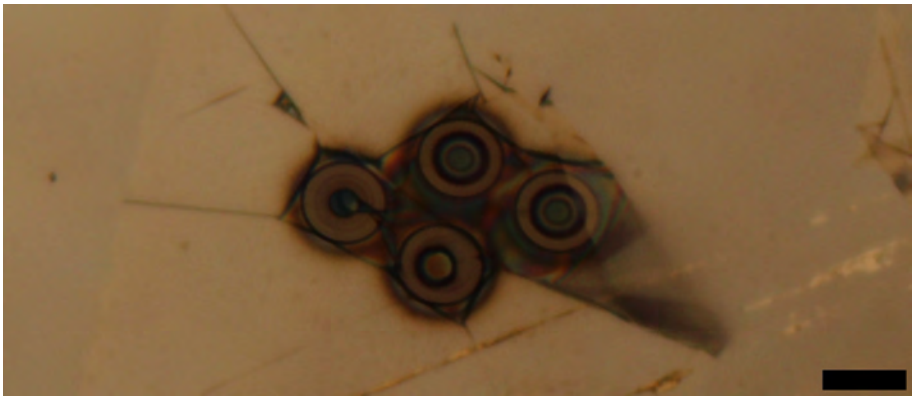

Figure 8.1: Graphene mechanical resonators on Colosseum cavities. The four devices are covered by a graphite flake (10 graphene layers), although only top and right ones have the membrane clamped at the highest plateau. The concentrically circular terraces are the proposed evolution of circular cavities to understand the behavior of membranes at the nanoscale in terms of plateau and sidewall adhesions. Also, this type of devices could lead to the creation of a new kind of pressure sensors with discrete changes in their resonance frequency. Scale bar is 5 μm.

Figure 8.1 shows the optical image of the first Colosseum drumhead devices immediately after the graphene transfer. We notice the colorful rings that appear on suspended membranes indicating their successful freestanding status. While three of the membranes display an outer black ring, one presents a clear/silver color instead. The lack of color in-

dicates that the membrane stuck to the outer terrace in that particular device in contrast to the other three that remain suspended over the first plateau of about 100 nm in depth.

We used the laser interferometry technique from Chapter 2 to measure the resonance frequency from one of the devices as a function of pressure (laser power of 4 mW). Figure 8.2 presents the colormap of the frequency spectrum when increasing the pressure from 10 mbar to 1 bar of N_2. We observed no hysteresis that could happen if the membrane reached and got stuck to a lower terrace. From the fundamental resonance frequency peak, we obtain an initial tension of 0.82 N/m that increases in two steps to 0.88 N/m and to 1.41 N/m. The tension value at zero pressure difference is about 40 times larger than measured in circular devices shown in this thesis, and it is unclear if it is due to the transfer process, the substrate material or membrane adhesion.

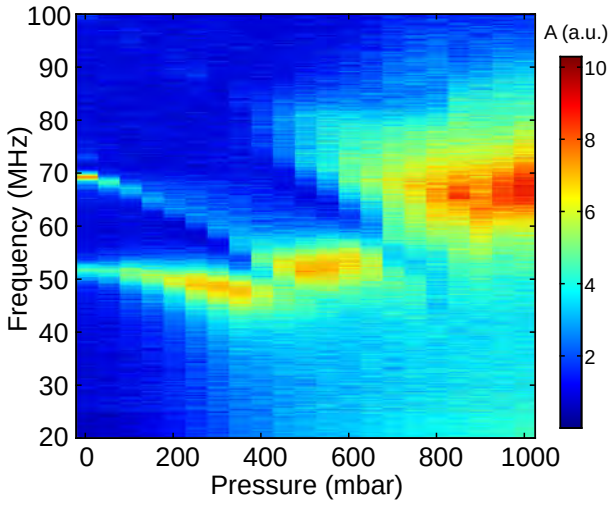

Figure 8.2: Resonance frequency change as a function of pressure in a Colosseum cavity. The fundamental mode seems to increase discontinuously (in steps) upon the increase of pressure.

Further work on Moray/Colosseum drumhead resonators will increase our knowledge on the adhesion of graphene and other 2D membranes to the cavity sidewalls. These measurements could be performed as a function of pressure, temperature and electrical pulling on terraces of smaller gaps to facilitate the membrane sticking to lower plateaus. Beside enabling the quick determination of the status of the membrane by inspecting the level of the black ring, I foresee a new type of device for sensing applications that exploits the discrete change of the resonance frequency of a membrane when moving from one terrace level to another.

8.3. BEYOND YIELD CHARACTERIZATION: STATISTICAL PERMEANCE

The industrial scale production of large-area graphene is currently led by material grown with the chemical vapor deposition (CVD) technique on catalytic foils made out of copper [64, 65]. However, the resulting CVD single-layer graphene (SLG) tends to have defects [116] that worsen many properties such as its Young's modulus [114, 115] and can allow gas molecules to permeate through the basal plane [121]. When transferring graphene onto cavities, those imperfections may also play a role in the successful suspension of the membranes by affecting the device yield and tension [154]. To reduce the effects of defects -especially regarding gas permeability-, two layers of CVD SLG can be stuck or piled up on top of each other, hence resulting in CVD double-layer graphene (DLG) membranes.

One of the promising applications of graphene MEMS/NEMS is their use as hermetic pressure sensors. The commercialization of these systems requires the development of techniques that allow their parallel and quick characterization for statistical studies and quality control. Techniques such as laser interferometry [105, 111], Raman spectroscopy [106, 112, 113], and atomic force microscopy [114, 115] are useful for in-depth investigation of individual devices. A more suitable tool is the colorimetry technique as it exploits the change of color interference when the membranes are deflected to non-invasively extract their mechanical properties and permeability with only an optical microscope [153].

Here we report a massive statistical permeability study of DLG drumheads with the colorimetry technique. We analyze 2760 CVD DLG drumheads of different diameters from two different samples with cavities of different depth. The statistical distributions show a large spread of the gas (N_2) permeance values from $2.8 \cdot 10^{-15}$ to $6.7 \cdot 10^{-14}$ $\frac{\text{mol}}{\text{m}^2\text{s}\cdot\text{Pa}}$, hence pointing to its independence from diameter. However, when the two samples are compared, there seems to be a correlation between larger time constants and deeper cavities, thus suggesting that the dominant gas leak channel are pores in the membranes.

8.3.1. PRELIMINARY RESULTS

For the fabrication of graphene drums, circular cavities of diameters ranging from 6 to 15 μm in diameter are etched through a thermally-grown SiO_2/Si layer. Two samples are prepared with two different cavity depths: 570 and 750 nm. Two SLG CVD graphene layers are stuck to each other and then transferred onto the patterned substrate with a semi-dry transfer technique, hence suspending the graphene with a drumhead shape. The choice of DLG over SLG membranes, as found in our previous works, is due to the higher yield [154] and their increased absorption in the visible spectrum of light that eases the visualization to perform colorimetry studies [153].

Previously, we showed that the application of a pressure difference across a DLG membrane sealing a cavity induces a change on its overall color, and the study of the reflectance over time allows us to measure the permeance of the device. By upgrading the code for the same colorimetry technique on an optical microscope with Köhler illumination, we analyze

The work in Section 8.3 is based on the Master thesis "Gas permeation study of CVD graphene nanodrums using colorimetry" by Ruben Smouter, supervised by S.J. Cartamil-Bueno and Dr. S. Houri (in collaboration with Prof. Steeneken's group).

hundreds of devices in parallel to obtain relevant statistical data on their deflection evolution when exposed to a stepped change of pressure.

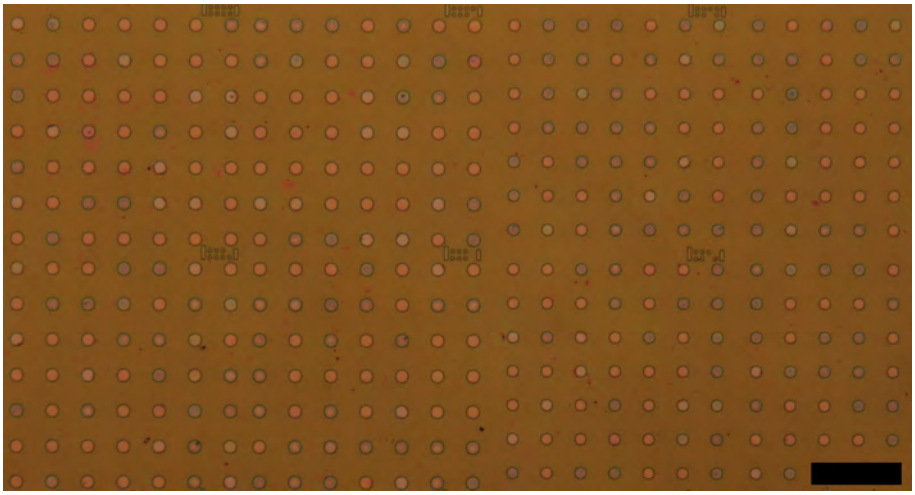

Figure 8.3: Hundreds of DLG drums in a purging experiment. Scale bar is 50 μm.

Figure 8.3 shows an area of different-sized drums for the sample with cavities of 570 nm deep during a purging experiment: after balancing the drums' internal pressure in an overpressure chamber (P_{inside} = 3 bar) for several days, the sample was brought to ambient pressure ($P_{outside}$ = 1 bar). The devices are bulged-up or upward deflected due to the gas trying to escape the cavity (hence being purged), following the mechanics of a circular membrane:

$$\frac{\Delta P}{A} = \frac{P_{outside} - P_{inside}}{A} = k_1\delta + k_3\delta, \tag{8.1}$$

where k_1, k_3 are the linear and nonlinear spring constants of the drum, respectively; A, its area; and δ is the deflection at the center of the drumhead.

The reason for which not all of the membranes in Figure 8.3 have the same color is their difference in permeance $\mathscr{P}$ [195]. The origin of gas leak in graphene drumheads is still unknown, although there are three hypothetical leak channels: through the SiO_2 cavity walls, through the SiO_2-graphene interface, and/or through pores in the membrane.

The permeance of membranes can be calculated from the time constant τ deflating in the small deflection regime as the membrane deflection follows a decaying exponential with time (Chapter 6):

$$\delta(t) = g_0 + \delta_0 e^{-t/\tau}, \tag{8.2}$$

where δ_0 and g_0 are the initial deflection in the linear regime and its position at rest, respectively, and $\tau = \frac{g_0}{\mathscr{P}RT}$, with R being the universal gas constant, and T=300 K, the temperature.

The overall reflectance then becomes

$$\mathscr{R}_{drum}(t) \approx A + B\, e^{-t/\tau}, \tag{8.3}$$

where A and B are constants that depend on the wavelength of the illuminating light and the phase delay of the light when being reflected.

Figure 8.4 shows the permeability distributions of the two samples. For the 570 nm sample (top panel), a distribution peak seems visible aroudn $0.5 \cdot 10^{-14}$ $\frac{\text{mol}}{\text{m}^2\text{s}\cdot\text{Pa}}$, while the same feature is inexistent for the sample of 750 nm of cavity depths (possibly being shifted to a lower permeance value). The wider bars at low permeance values represent the very hermetic drums in the samples that could not be fitted with a time constant due to the limitations of the measurement system.

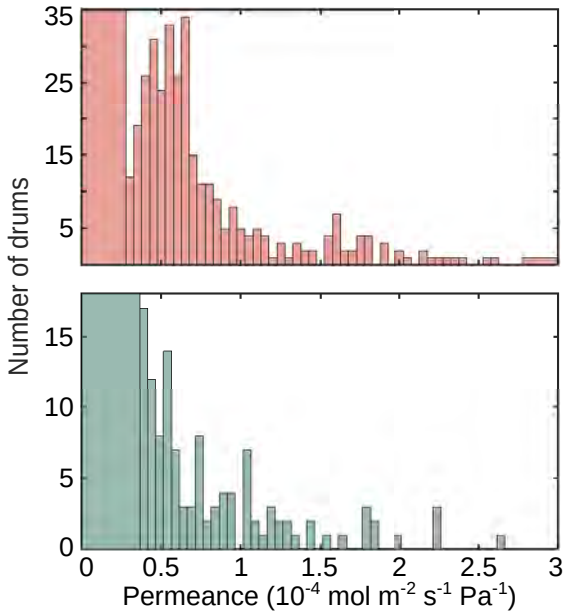

Figure 8.4: Distribution of the permeance for circular DLG membranes of diameters ranging from 3 to 20 μm in diameter. Two substrates with cavities of a particular depth are analyzed: 570 nm (above) and 750 nm (below).

By studying the time constant of the pressure decay as a function of the diameter D of graphene drums, we could determine which of the channels is more likely or contributes the most:

- $\mathscr{P} \not\propto f(D)$ for leak through pores in the graphene membrane;
- $\mathscr{P} \propto \frac{1}{D}$ for leak through substrate-graphene interface; or
- $\mathscr{P} \propto \frac{g_0}{D}$ for leak through the sidewalls of the SiO_2 cavity.

Figure 8.5 collects the complete datasets of time constants for the drumheads of different diameters in the two samples. As observed, the mean of the time constant seems to be constant as a function of diameter for the two samples, while it is slightly higher in the sample with deeper cavities.

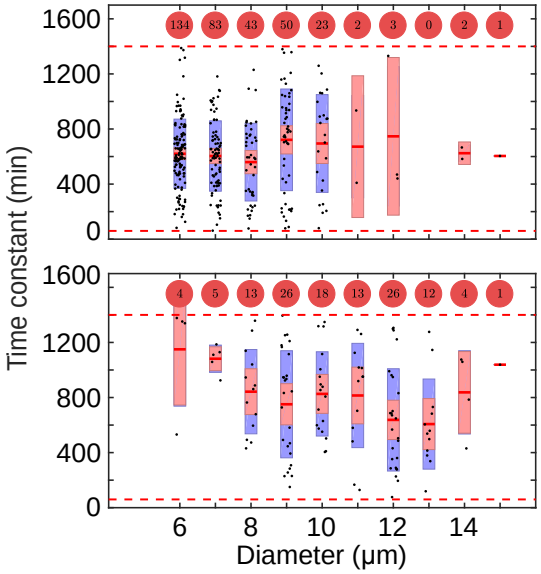

Figure 8.5: Distribution of the time constants as a function of diameter for the same circular DLG membranes from Figure 8.4 (570 nm sample above, 750 nm sample below). Each population is represented by its mean (red solid line), the 95% confidence interval of the mean (red bands) and the standard deviation (blue bands). Data points are plotted with a random lateral offset, and the red circles on top show the number of data points per diameter. The red dotted lines show the limits of the measurement.

These preliminary results are an important demonstration of the colorimetry technique for the massive characterization of the permeance of graphene membranes. The obtained values are similar to those reported before [153] and from exfoliated graphene drums reported in literature [52, 121]. However, the restrictions of the measurement system and the inconsistencies and misfits from the computer algorithm prevent us from having an unambiguous statement about the device behavior. Further studies with an improved technique is required to obtain a clear understanding of geometry dependences of the permeance in these drumheads and the channel of gas leaking. Statistics on the permeability of CVD graphene with different layers could also reveal the feasibility of hermetic sensors or molecular sieves.

8.4. BEYOND GRAPHENE SENSORS: GRAPHENEX'S LIGHT SAILS

Space exploration is nowadays limited to our solar system because there is no propulsion technology with enough thrust to accelerate spacecrafts once in space. An interstellar shuttle must reach velocities higher than 1% of speed of light to arrive to the closest solar system in less than a century [217]. Since chemical rocket propulsion has low specific impulse (ratio of thrust to propellant mass) and the amount of fuel is limited due to launch expenses, other alternatives for in-space propulsion must be found.

One of the proposed technologies is solar sailing to transport low-mass shuttles [218, 219, 220]. The Sun is a light source emitting photons with a momentum than can be transferred to a highly reflective material. In the past decade, the radiation pressure from the Sun has been used for altitude control of satellites and even as a primary propulsion system to explore the Solar System [221]. However, the thrust from light pressure is too low, and the sail should be made impracticably large to gain sufficient speed. For that reason, we must combine radiation pressure with other propulsion methods, or develop highly reflective materials with low mass and thickness yet mechanically strong and stiff so that the problems with sail deployment and space particle bombardment are reduced [222, 223, 224].

The recent advances in materials science that led to the discovery of 2D materials now could pave the way for the fabrication of solar sails with multiple functionalities that ultimately combine different types of propulsion mechanisms. The ultimate thinness of graphene –which implies a low mass density– makes it suitable for mechanical systems [56, 108, 111], although also causes its poor optical reflectance [225]. Suspending graphene on circular cavities or trenches eliminates the negative impact of the substrate on its thermal and electrical properties [78], allows the exploitation of its mechanical properties, and enables pure interaction with the material. For instance, illuminating isolated graphene with visible light causes an Auger-like phenomenon resulting in electrons of high energy being ejected from the material [226].

Figure 8.6 shows the mechanism of electron ejection from graphene claimed in reference [226]. Due to an Auger-like phenomenon, laser illumination in the visible spectrum promotes an energy increase of the electrons in the conduction band, resulting in the ejection of hot electrons with an average kinetic energy of 70 eV. This light-matter interaction consists of a double transfer of momentum –from the photon to the material when absorbed, and from the electron to the material when ejected– that could be used for propulsion. In the publication, lasers of different wavelengths and powers are used to displace a graphene composite material of about 3 mg.

Reference [226] states that the electron ejection phenomenon occurs due to the existence of an electronic bandgap (forbidden energy levels) originated from the isolation of freestanding graphene in the in the composite material. Since single-layer graphene has no bandgap, we will use double-layer graphene (a stack of two layers of graphene). Bilayer graphene is known to have a small bandgap [227] with a similar band dispersion energy as

Section 8.4 is part of the accepted proposal "Graphene-based spacecraft sail for light-induced propulsion" for ESA's Drop Your Thesis! 2017 Programme. The experiment was performed in November 2017 by GrapheneX team composed by Santiago J. Cartamil-Bueno (team leader), Dr. Rocco Gaudenzi, Davide Stefani, and Vera Janssen.

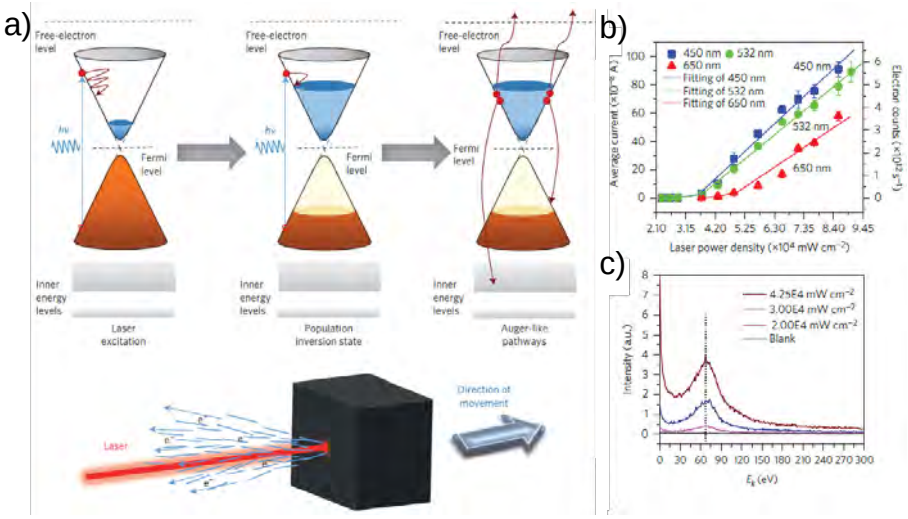

Figure 8.6: Light-induced thrust based on electron ejection from graphene-based material. (a) Proposed Auger-like mechanism for the ejection of electrons. (b) Measured electron flow escaping the graphene material for three laser sources of different wavelengths as a function of laser power. (c) Measured kinetic energy of the ejected electrons. A peak at around 70 eV is observed. All panels adapted from reference [226].

shown in Figure 8.6a, which supposedly prevents or hinders the electron-hole recombination processes after light absorption.

The work of reference [226] demonstrates that electrons are ejected with a kinetic energy of $E_k = 70$ eV in average, which means they escape at a speed of $v_e = \sqrt{\frac{(E_k - m_e c^2)^2 - m_e^2 c^4}{m_e c}} = 4.96 \cdot 10^6$ m/s (a 2% of the light speed). Furthermore, they measure an ejection rate from 2 to $57 \cdot 10^{12}$ electrons per second. Since the mass of an electron is $m_e = 9.1 \cdot 10^{-31}$ kg, the mass flow $\dot{M}$ is from 1.8 to $52 \cdot 10^{-19}$ kg/s. For the same sample mass, the thrust $T_e = (\dot{M} v_e)/m$ would be from 3 to $86 \cdot 10^{-7}$ N/kg, that would cause a displacement of 13 to 372 μm in 9.3 seconds. This micrometric displacement could be observed with a microscope objective parallel to the launch direction.

Taking into consideration that one graphene monolayer has a considerable optical absorption in the visible spectrum20, stacking several layers on top of each other would enhance the direct momentum transfer from light. The total force caused by radiation pressure considering both absorption and reflection of light would be $F = A(p_{abs} + p_{ref}) \approx 2\left(\pi\alpha + 2\frac{\pi^2\alpha^2}{4}\left(\frac{2}{2+\pi\alpha}\right)^2\right)\frac{P}{c} = 1.5 \cdot 10^{-10}\,\frac{\text{N}}{\text{W}} \cdot P[\text{W}]$ for a double-layer graphene illuminated normally in its whole area A by a laser of power P, where α is the fine structure constant that determines the universal opacity of graphene. As a result, for a sample of $m = 3$ mg in weight and a 1 W laser, the thrust from pressure radiation is expected to be $T_p = 5.1 \cdot 10^{-5}$ N/kg. This would cause a displacement of 2205 μm in 9.3 seconds.

Tests in our lab show that a blue laser is able to move this suspended double-layer material as presented in Figure 8.7, while however a red laser of larger power does not affect it. This contradicts the universal absorption from reference [225] but sustains the absorption-enhancement (and thus increased heating) induced by interferometry effects in graphene cavities as discussed in Chapters 3-4. In the optical microscope image we observe a silicon chip with circular cavities that are covered by double-layer graphene. One of these circular membranes has a visual yellow color that originates from the light interference due to the position of the membrane with respect to the surface level. When it is illuminated with a laser of 405 nm and about 1 mW of power, the color of the membrane changes, which indicates a change of the position in the order of hundreds of nanometers. Unfortunately, the device used in this test (a cavity sealed with graphene) is not ideal to prove displacement caused by the laser since thermal effects between the suspended material and the substrate could result in the same effect, the bottom of the cavity is a mirror-like material that reflects the laser back to the membrane, and the substrate material could induce electrostatic effects that affect the experiment. Other tests in our lab with graphene suspended on holey kapton films point in the same direction, although the mechanical clamping together with its undesirable thermal expansion prevents us from proving the light-induced displacement.

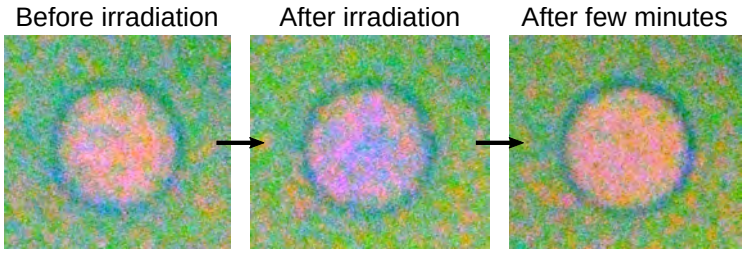

Figure 8.7: Light-induced change of color of suspended double-layer graphene membrane of 13 μm in diameter. Colorimetry techniques indicates that the illumination of the membrane with a laser of 405 nm and about 1 mW of power has induced a displacement of the membrane with respect to the surface level. This displacement is reversible since the suspended membrane has a certain spring constant.

In this experiment within the European Space Agency (ESA) Drop Your Thesis! Programme 2017, we will test the claims of the light-induced electron thrust reported in [226] in a controlled environment. Instead of using a composite material that could be hard to reproduce and model, we will use CVD graphene from a company provider (Graphenea S.A.), which undergoes quality control processes and has been studied exhaustively. In order to obtain measurable displacements, we will suspend the CVD graphene on holey transmission electron microscope (TEM) grids that would act as the frame of a millimetric solar sail of 1-5 mg of weight.

Measuring the displacement in a controlled environment where we can rule out thermal and gravitation effects will help us to clarify the physical mechanism that dominates the light-induced displacement of graphene. Depending on the amount of displacement and its wavelength dependence, we could improve the model and clearly determine if the mo-

mentum transfer is ruled by electron ejection or pressure radiation. Moreover, the success of the experiment would open the door to a new application of graphene in the aerospace industry and would lead to new studies on 2D materials for solar sailing that could transfer the material technology and the public attention on graphene to the space industry sector.

8.4.1. PRELIMINARY RESULTS

Prior to the measurement, we designed and built a vacuum-sealed setup consisting of two KF50 cross tubes that host similar components. One of the tubes is intended for testing a sample and the other one for measuring a reference TEM grid. Inside a cross tube, a release mechanism (shown in Figure 8.8a) keeps in place the graphene light sail (copper TEM grid of about 25μm of thickness and 40% of transmission covered with graphene) until the microgravity condition ($10^{-6}g_0$) is reached during the experiment. At that moment, the sail is released and a laser beam of 1 W and a chosen wavelength (450, 532 and 655 nm) impinges the test sample from below.

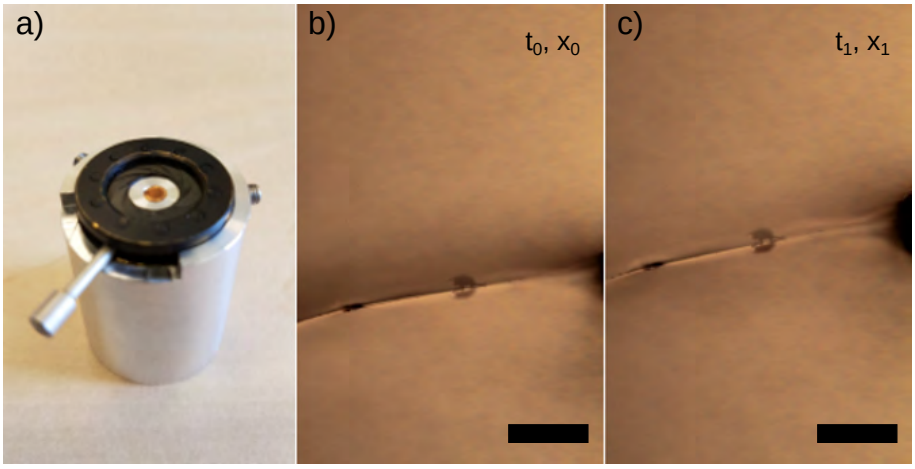

Figure 8.8: GrapheneX setup and measurement. a) Release mechanism holding a graphene light sail (TEM grid of 3 mm in diameter covered with graphene) will be inside a KF50 cross tube in vacuum. A custom microscope will record the cross-section movement of the sail upon laser irradiation. b-c) show pictures from the side of the TEM grid emulating two instants of the displaced sail at two different positions. Scale bars are 250 μm.

A custom microscope composed of a consumer camera (Canon EOS 600D) and a microscope objective of 5× (Mitutoyo M Plan APO) records the sample motion from its side from the capsule launch until the end of the microgravity condition (emulation in in Figure 8.8b-c). Analysis of the video data by means of extracting the sail displacement as function of incident laser wavelength will determine the nature of the phenomenon. If we do not observe a wavelength-dependence of the displacement, the displacement mechanism is dominated by radiation pressure; otherwise, the displacement is affected by electron ejection (similar as in a previous work [226]) or some new phenomenon we would have to research further.

REFERENCES

[1] Wikimedia Commons, *File:periodic table armtuk3.svg,* Wikimedia Commons, the free media repository (2017).

[2] Wikipedia, *History of materials science,* Wikipedia, The Free Encyclopedia (2017).

[3] Wikipedia, *History of technology,* Wikipedia, The Free Encyclopedia (2017).

[4] Wikipedia, *Timeline of materials technology,* Wikipedia, The Free Encyclopedia (2017).

[5] Wikipedia, *Transistor,* Wikipedia, The Free Encyclopedia (2017).

[6] Wikipedia, *Graphite,* Wikipedia, The Free Encyclopedia (2017).

[7] Martin and J. Norgate, *Old cumbria gazetteer, black lead mine, seathwaite,* http://www.geog.port.ac.uk (2016).

[8] A. Wainwright, *A pictorial guide to the lakeland fells: The western fells,* Westmorland Gazette (1964).

[9] G. Britain and D. Pickering, *The Statutes at Large, from the First Year of K. William and Q. Mary, to the Eighth Year of K. William III: To which is Prefixed, a Table Containing the Titles of All the Statutes During that Period,* Joseph Bentham, printer to the University (1764).

[10] Wikimedia Commons, *File:kimmirut graphite.jpg,* Wikimedia Commons, the free media repository (2015).

[11] G. Hodan, *Paper and a pencil,* www.PublicDomainPictures.net (2017).

[12] Wikipedia, *Empiricism,* Wikipedia, The Free Encyclopedia (2017).

[13] C. W. Scheele, *Versuche mit wasserbley; molybdaena,* Svenska Vetenskaps Akademiens Handlingar **40**, 238 (1779).

[14] C. A. S. Hoffman, *Mineralsystem des herrn inspektor werners mit dessen erlaubnis herausgegeben,* Bergmännisches Journal **1**, 369 (1789).

[15] B. C. Brodie, *On the atomic weight of graphite,* Philosophical Transactions of the Royal Society of London **149**, 249 (1859).

[16] A. K. Geim, *Graphene prehistory,* Physica Scripta **2012**, 014003 (2012).

[17] P. Debye and P. Scherrer, *Interferenzen an regellos orientierten teilchen im röntgenlicht i,* Nachrichten von der Gesellschaft der Wissenschaften zu Göttingen, Mathematisch-Physikalische Klasse **1916**, 1 (1916).

[18] V. Kohlschütter and P. Haenni, *Zur kenntnis des graphitischen kohlenstoffs und der graphitsäure,* Zeitschrift für anorganische und allgemeine Chemie **105**, 121 (1919).

[19] O. Hassel and H. Mark, *Über die kristallstruktur des graphits,* Zeitschrift für Physik A Hadrons and Nuclei **25**, 317 (1924).

[20] J. D. Bernal, *The structure of graphite,* Proceedings of the Royal Society of London, Series A, Containing Papers of a Mathematical and Physical Character **106**, 749 (1924).

[21] Wikimedia Commons, *File:carbon allotropes.svg,* Wikimedia Commons, the free media repository (2016).

[22] Wikimedia Commons, *File:graphite-layers-top-3d-balls.png,* Wikimedia Commons, the free media repository (2015).

[23] Wikimedia Commons, *File:carbon-phase-diagramp.svg,* Wikimedia Commons, the free media repository (2016).

[24] Wikimedia Commons, *File:benzene orbitals.svg,* Wikimedia Commons, the free media repository (2016).

[25] Wikimedia Commons, *File:sp2-orbital.svg,* Wikimedia Commons, the free media repository (2014).

[26] L. F. Dobrzhinetskaya, R. Wirth, J. Yang, I. D. Hutcheon, P. K. Weber, and H. W. Green, *High-pressure highly reduced nitrides and oxides from chromitite of a tibetan ophiolite,* Proceedings of the National Academy of Sciences **106**, 19233 (2009).

[27] W. H. Balmain, *Bemerkungen über die bildung von verbindungen des bors und siliciums mit stickstoff und gewissen metallen,* Advanced Synthesis & Catalysis **27**, 422 (1842).

[28] E. Tiede and H. Tomaschek, *Über das aktivierende element im leuchtenden borstickstoff,* Zeitschrift für anorganische und allgemeine Chemie **147**, 111 (1925).

[29] F. Wöhler, *Ueber den stickstoffbor,* European Journal of Organic Chemistry **74**, 70 (1850).
[30] E. Podzus, *Widerstände einiger reiner isolatoren bei. hohen temperaturen,* Verhandlungen der Deutschen Physikalischen Gesellschaft **1917**, 231 (1917).
[31] R. H. Wentorf Jr, *Cubic form of boron nitride,* The Journal of Chemical Physics **26**, 956 (1957).
[32] R. Machaka, *Ion Beam Modifications of Boron Nitride By Ion Implantation (PhD Thesis),* Faculty of Science, University of the Witwatersrand, Johannesburg (2008).
[33] Wikimedia Commons, *File:boron-nitride-(sphalerite)-3d-balls.png,* Wikimedia Commons, the free media repository (2015).
[34] Wikimedia Commons, *File:boron-nitride-(hexagonal)-side-3d-balls.png,* Wikimedia Commons, the free media repository (2015).
[35] Wikimedia Commons, *File:boron-nitride-(hexagonal)-top-3d-balls.png,* Wikimedia Commons, the free media repository (2015).
[36] V. M. Goldschmidt, *Darstellung und eigenschaften des krystallisierten bornitrides,* O. Hassel: Die Kristallstruktur des Bornitrides, BN. –Norsk Geologisk Tidskrift **1926**, 258 (1926).
[37] R. S. Pease, *An x-ray study of boron nitride,* Acta Crystallographica **5**, 356 (1952).
[38] P. Miró, M. Audiffred, and T. Heine, *An atlas of two-dimensional materials,* Chemical Society Reviews **43**, 6537 (2014).
[39] K. S. Novoselov, D. Jiang, F. Schedin, T. J. Booth, V. V. Khotkevich, S. V. Morozov, and A. K. Geim, *Two-dimensional atomic crystals,* Proceedings of the National Academy of Sciences of the United States of America **102**, 10451 (2005).
[40] A. K. Geim and I. V. Grigorieva, *Van der waals heterostructures,* Nature **499**, 419 (2013).
[41] K. S. Novoselov, A. Mishchenko, A. Carvalho, and A. H. C. Neto, *2D materials and van der Waals heterostructures,* Science **353**, aac9439 (2016).
[42] A. K. Geim and K. S. Novoselov, *The rise of graphene,* Nature Materials **6**, 183 (2007).
[43] A. K. Geim, *Graphene: status and prospects,* Science **324**, 1530 (2009).
[44] K. S. Novoselov, V. I. Falko, L. Colombo, P. R. Gellert, M. G. Schwab, and K. Kim, *A roadmap for graphene,* Nature **490**, 192 (2012).
[45] K. S. Novoselov, A. K. Geim, S. V. Morozov, D. Jiang, Y. Zhang, S. V. Dubonos, I. V. Grigorieva, and A. A. Firsov, *Electric field effect in atomically thin carbon films,* Science **306**, 666 (2004).
[46] K. S. Novoselov, A. K. Geim, S. Morozov, D. Jiang, M. Katsnelson, I. V. Grigorieva, S. Dubonos, Firsov, and A. A, *Two-dimensional gas of massless dirac fermions in graphene,* Nature **438**, 197 (2005).
[47] A. H. C. Neto, F. Guinea, N. M. R. Peres, K. S. Novoselov, and A. K. Geim, *The electronic properties of graphene,* Reviews of Modern Physics **81**, 109 (2009).
[48] K. I. Bolotin, K. J. Sikes, Z. Jiang, M. Klima, G. Fudenberg, J. Hone, P. Kim, and H. L. Stormer, *Ultrahigh electron mobility in suspended graphene,* Solid State Communications **146**, 351 (2008).
[49] J.-H. Chen, C. Jang, S. Xiao, M. Ishigami, and M. S. Fuhrer, *Intrinsic and extrinsic performance limits of graphene devices on SiO_2,* Nature Nanotechnology **3**, 206 (2008).
[50] A. A. Balandin, S. Ghosh, W. Bao, I. Calizo, D. Teweldebrhan, F. Miao, and C. N. Lau, *Superior thermal conductivity of single-layer graphene,* Nano Letters **8**, 902 (2008).
[51] C. Lee, X. Wei, J. W. Kysar, and J. Hone, *Measurement of the Elastic Properties and Intrinsic Strength of Monolayer Graphene,* Science **321**, 385 (2008).
[52] J. S. Bunch, S. S. Verbridge, J. S. Alden, A. M. Van Der Zande, J. M. Parpia, H. G. Craighead, and P. L. McEuen, *Impermeable atomic membranes from graphene sheets,* Nano Letters **8**, 2458 (2008).
[53] M. C. Lemme, T. J. Echtermeyer, M. Baus, and H. Kurz, *A graphene field-effect device,* IEEE Electron Device Letters **28**, 282 (2007).
[54] Z. Yan, G. Liu, J. M. Khan, and A. A. Balandin, *Graphene quilts for thermal management of high-power GaN transistors,* Nature Communications **3**, 827 (2012).
[55] J. Dauber, A. A. Sagade, M. Oellers, K. Watanabe, T. Taniguchi, D. Neumaier, and C. Stampfer, *Ultra-sensitive hall sensors based on graphene encapsulated in hexagonal boron nitride,* Applied Physics Letters **106**, 193501 (2015).
[56] C. Chen, S. Rosenblatt, K. I. Bolotin, W. Kalb, P. Kim, I. Kymissis, H. L. Stormer, T. F. Heinz, and J. Hone, *Performance of monolayer graphene nanomechanical resonators with electrical readout,* Nature Nanotechnology **4**, 861 (2009).

[57] C. S. Boland, U. Khan, G. Ryan, S. Barwich, R. Charifou, A. Harvey, C. Backes, Z. Li, M. S. Ferreira, M. E. Möbius, R. J. Young, and J. N. Coleman, *Sensitive electromechanical sensors using viscoelastic graphene-polymer nanocomposites,* Science **354**, 1257 (2016).

[58] A. D. Smith, F. Niklaus, A. Paussa, S. Vaziri, A. C. Fischer, M. Sterner, F. Forsberg, A. Delin, D. Esseni, P. Palestri, M. Östling, and M. C. Lemme, *Electromechanical piezoresistive sensing in suspended graphene membranes,* Nano Letters **13**, 3237 (2013).

[59] R. J. Dolleman, D. Davidovikj, S. J. Cartamil-Bueno, H. S. J. van der Zant, and P. G. Steeneken, *Graphene Squeeze-Film Pressure Sensors,* Nano Letters **16**, 568 (2016).

[60] R. R. Nair, H. A. Wu, P. N. Jayaram, I. V. Grigorieva, and A. K. Geim, *Unimpeded Permeation of Water Through Helium-Leak-Tight Graphene-Based Membranes,* Science **335**, 442 (2012).

[61] H. Alcalde, J. De La Fuente, B. Kamp, and A. Zurutuza, *Market uptake potential of graphene as a disruptive material,* Proceedings of the IEEE **101**, 1793 (2013).

[62] A. C. Ferrari, F. Bonaccorso, V. Falko, K. S. Novoselov, S. Roche, P. Bøggild, S. Borini, F. Koppens, V. Palermo, N. Pugno, J. A. Garrido, R. Sordan, A. Bianco, L. Ballerini, M. Prato, E. Lidorikis, J. Kivioja, C. Marinelli, T. Ryhänen, A. Morpurgo, J. N. Coleman, V. Nicolosi, L. Colombo, A. Fert, M. Garcia-Hernandez, A. Bachtold, G. F. Schneider, F. Guinea, C. Dekker, M. Barbone, C. Galiotis, A. Grigorenko, G. Konstantatos, A. Kis, M. Katsnelson, C. W. J. Beenakker, L. Vandersypen, A. Loiseau, V. Morandi, D. Neumaier, E. Treossi, V. Pellegrini, M. Polini, A. Tredicucci, G. M. Williams, B. H. Hong, J. H. Ahn, J. M. Kim, H. Zirath, B. J. van Wees, H. van der Zant, L. Occhipinti, A. Di Matteo, I. A. Kinloch, T. Seyller, E. Quesnel, X. Feng, K. Teo, N. Rupesinghe, P. Hakonen, S. R. T. Neil, Q. Tannock, T. Löfwander, and J. Kinaret, *Science and technology roadmap for graphene, related two-dimensional crystals, and hybrid systems,* Nanoscale **7**, 4598 (2014).

[63] A. Zurutuza and C. Marinelli, *Challenges and opportunities in graphene commercialization,* Nature Nanotechnology **9**, 730 (2014).

[64] X. Li, W. Cai, J. An, S. Kim, J. Nah, D. Yang, R. Piner, A. Velamakanni, I. Jung, E. Tutuc, S. K. Banerjee, L. Colombo, and R. S. Ruoff, *Large-area synthesis of high-quality and uniform graphene films on copper foils,* Science **324**, 1312 (2009).

[65] X. Li, L. Colombo, and R. S. Ruoff, *Synthesis of graphene films on copper foils by chemical vapor deposition,* Advanced Materials **28**, 6247 (2016).

[66] K. S. Kim, Y. Zhao, H. Jang, S. Y. Lee, J. M. Kim, K. S. Kim, J.-H. Ahn, P. Kim, J.-Y. Choi, and B. H. Hong, *Large-scale pattern growth of graphene films for stretchable transparent electrodes,* Nature **457**, 706 (2009).

[67] J. H. Lee, E. K. Lee, W. J. Joo, Y. Jang, B. S. Kim, J. Y. Lim, S. H. Choi, S. J. Ahn, J. R. Ahn, M. H. Park, C. W. Yang, B. L. Choi, S. W. Hwang, and D. Whang, *Wafer-Scale Growth of Single-Crystal Monolayer Graphene on Reusable Hydrogen-Terminated Germanium,* Science **344**, 286 (2014).

[68] R. Geick, C. Perry, and G. Rupprecht, *Normal Modes in Hexagonal Boron Nitride,* Physical Review **146**, 543 (1966).

[69] N. Alem, R. Erni, C. Kisielowski, M. D. Rossell, W. Gannett, and A. Zettl, *Atomically thin hexagonal boron nitride probed by ultrahigh-resolution transmission electron microscopy,* Physical Review B **80**, 1 (2009).

[70] G. Cassabois, P. Valvin, and B. Gil, *Hexagonal boron nitride is an indirect bandgap semiconductor,* Nature Photonics **10**, 262 (2016).

[71] C. R. Dean, A. F. Young, I. Meric, C. Lee, L. Wang, S. Sorgenfrei, K. Watanabe, T. Taniguchi, P. Kim, K. L. Shepard, and J. Hone, *Boron nitride substrates for high-quality graphene electronics,* Nature Nanotechnology **5**, 722 (2010).

[72] J. Li, S. Majety, R. Dahal, W. P. Zhao, J. Y. Lin, and H. X. Jiang, *Dielectric strength, optical absorption, and deep ultraviolet detectors of hexagonal boron nitride epilayers,* Applied Physics Letters **101**, 171112 (2012).

[73] A. Aldalbahi and P. Feng, *Development of 2-D Boron Nitride Nanosheets UV Photoconductive Detectors,* IEEE Transactions on Electron Devices **62**, 1885 (2015).

[74] Y. Kimura, T. Wakabayashi, K. Okada, T. Wada, and H. Nishikawa, *Boron nitride as a lubricant additive,* Wear **232**, 199 (1999).

[75] L. Song, L. Ci, H. Lu, P. B. Sorokin, C. Jin, J. Ni, A. G. Kvashnin, D. G. Kvashnin, J. Lou, B. I. Yakobson, and P. M. Ajayan, *Large scale growth and characterization of atomic hexagonal boron nitride layers,* Nano Letters **10**, 3209 (2010).

[76] R. V. Gorbachev, I. Riaz, R. R. Nair, R. Jalil, L. Britnell, B. D. Belle, E. W. Hill, K. S. Novoselov, K. Watanabe, T. Taniguchi, A. K. Geim, and P. Blake, *Hunting for Monolayer Boron Nitride: Optical and Raman Signatures,*

Small **7**, 465 (2011).

[77] D. Pacilé, J. C. Meyer, Ç. Ö. Girit, and A. Zettl, *The two-dimensional phase of boron nitride: Few-atomic-layer sheets and suspended membranes,* Applied Physics Letters **92**, 133107 (2008).

[78] Y. D. Kim, H. Kim, Y. Cho, J. H. Ryoo, C.-H. Park, P. Kim, Y. S. Kim, S. Lee, Y. Li, S.-N. Park, Y. S. Yoo, D. Yoon, V. E. Dorgan, E. Pop, T. F. Heinz, J. Hone, S.-H. Chun, H. Cheong, S. W. Lee, M.-H. Bae, and Y. D. Park, *Bright visible light emission from graphene,* Nature Nanotechnology **10**, 1 (2015).

[79] A. Nagashima, N. Tejima, Y. Gamou, T. Kawai, and C. Oshima, *Electronic dispersion relations of monolayer hexagonal boron nitride formed on the Ni (111) surface,* Physical Review B **51**, 4606 (1995).

[80] E. Rokuta, Y. Hasegawa, K. Suzuki, Y. Gamou, C. Oshima, and A. Nagashima, *Phonon Dispersion of an Epitaxial Monolayer Film of Hexagonal Boron Nitride on Ni(111),* Physical Review Letters **79**, 4609 (1997).

[81] K. K. Kim, A. Hsu, X. Jia, S. M. Kim, Y. Shi, M. Hofmann, D. Nezich, J. F. Rodriguez-Nieva, M. Dresselhaus, T. Palacios, and J. Kong, *Synthesis of monolayer hexagonal boron nitride on Cu foil using chemical vapor deposition,* Nano Letters **12**, 161 (2012).

[82] P. R. Kidambi, R. Blume, J. Kling, J. B. Wagner, C. Baehtz, R. S. Weatherup, R. Schloegl, B. C. Bayer, and S. Hofmann, *In Situ Observations during Chemical Vapor Deposition of Hexagonal Boron Nitride on Polycrystalline Copper,* Chemistry of Materials **26**, 6380 (2014).

[83] G. Lu, T. Wu, Q. Yuan, H. Wang, H. Wang, F. Ding, X. Xie, and M. Jiang, *Synthesis of large single-crystal hexagonal boron nitride grains on Cu-Ni alloy,* Nature Communications **6**, 6160 (2015).

[84] S. Caneva, R. S. Weatherup, B. C. Bayer, R. Blume, A. Cabrero-Vilatela, P. Braeuninger-Weimer, M. B. Martin, R. Wang, C. Baehtz, R. Schloegl, J. C. Meyer, and S. Hofmann, *Controlling Catalyst Bulk Reservoir Effects for Monolayer Hexagonal Boron Nitride CVD,* Nano Letters **16**, 1250 (2016).

[85] J. M. Martin, T. Le Mogne, C. Chassagnette, and M. N. Gardos, *Friction of Hexagonal Boron Nitride in Various Environments,* Tribology Transactions **35**, 462 (1992).

[86] A. Nagashima, N. Tejima, Y. Gamou, T. Kawai, M. Terai, M. Wakabayashi, and C. Oshima, *Electron spectroscopic studies of monolayer hexagonal boron nitride physisorbed on metal surfaces,* International Journal of Modern Physics B **10**, 3517 (1996).

[87] N. Ooi, A. Rairkar, L. Lindsley, and J. B. Adams, *Electronic structure and bonding in hexagonal boron nitride,* Journal of Physics: Condensed Matter **18**, 97 (2006).

[88] F. Pizzocchero, L. Gammelgaard, B. S. Jessen, J. M. Caridad, L. Wang, J. Hone, P. Bøggild, and T. J. Booth, *The hot pick-up technique for batch assembly of van der Waals heterostructures,* Nature Communications **7**, 11894 (2016).

[89] L. B. Boinovich, A. M. Emelyanenko, A. S. Pashinin, C. H. Lee, J. Drelich, and Y. K. Yap, *Origins of thermodynamically stable superhydrophobicity of boron nitride nanotubes coatings,* Langmuir **28**, 1206 (2012).

[90] A. I. Aria, P. R. Kidambi, R. S. Weatherup, L. Xiao, J. A. Williams, and S. Hofmann, *Time Evolution of the Wettability of Supported Graphene under Ambient Air Exposure,* Journal of Physical Chemistry C **120**, 2215 (2016).

[91] T. T. Tran, K. Bray, M. J. Ford, M. Toth, and I. Aharonovich, *Quantum Emission From Hexagonal Boron Nitride Monolayers,* Nature Nanotechnology **11**, 37 (2015).

[92] R. Bourrellier, S. Meuret, A. Tararan, O. Stéphan, M. Kociak, L. H. G. Tizei, and A. Zobelli, *Bright UV Single Photon Emission at Point Defects in h-BN,* Nano Letters **16**, 4317 (2016).

[93] K. A. N. Duerloo, M. T. Ong, and E. J. Reed, *Intrinsic piezoelectricity in two-dimensional materials,* Journal of Physical Chemistry Letters **3**, 2871 (2012).

[94] K. A. N. Duerloo and E. J. Reed, *Flexural electromechanical coupling: A nanoscale emergent property of boron nitride bilayers,* Nano Letters **13**, 1681 (2013).

[95] A. Castellanos-Gomez, *Why all the fuss about 2D semiconductors?* Nature Photonics **10**, 202 (2016).

[96] S. Hu, M. Lozada-Hidalgo, F. C. Wang, A. Mishchenko, F. Schedin, R. R. Nair, E. W. Hill, D. W. Boukhvalov, M. I. Katsnelson, R. A. W. Dryfe, I. V. Grigorieva, H. A. Wu, and A. K. Geim, *Proton transport through one-atom-thick crystals,* Nature **516**, 227 (2014).

[97] K. I. Bolotin, K. J. Sikes, J. Hone, H. L. Stormer, and P. Kim, *Temperature-Dependent Transport in Suspended Graphene,* Physical Review Letters **101**, 096802 (2008).

[98] X. Du, I. Skachko, E. Y. Andrei, and A. Barker, *Approaching ballistic transport in suspended graphene,* Nature Nanotechnology **3**, 491 (2008).

[99] C. Chen, S. Lee, V. V. Deshpande, G. H. Lee, M. Lekas, K. Shepard, and J. Hone, *Graphene mechanical oscilla-*

tors with tunable frequency, Nature Nanotechnology **8**, 923 (2013).

[100] S. Houri, S. J. Cartamil-Bueno, M. Poot, P. G. Steeneken, H. S. J. Van der Zant, and W. J. Venstra, *Direct and parametric synchronization of a graphene self-oscillator,* Applied Physics Letters **110**, 073103 (2017).

[101] X. Liu, J. W. Suk, N. G. Boddeti, L. Cantley, L. Wang, J. M. Gray, H. J. Hall, V. M. Bright, C. T. Rogers, M. L. Dunn, R. S. Ruoff, and J. S. Bunch, *Large arrays and properties of 3-terminal graphene nanoelectromechanical switches,* Advanced Materials **26**, 1571 (2014).

[102] J. C. Meyer, A. K. Geim, M. I. Katsnelson, K. S. Novoselov, T. J. Booth, and S. Roth, *The structure of suspended graphene sheets,* Nature **446**, 60 (2007).

[103] K. I. Bolotin, K. J. Sikes, Z. Jiang, M. Klima, G. Fudenberg, J. Hone, P. Kim, and H. L. Stormer, *Ultrahigh electron mobility in suspended graphene,* Solid State Communications **146**, 351 (2008).

[104] P. Rickhaus, P. Makk, M.-H. Liu, E. Tóvári, M. Weiss, R. Maurand, K. Richter, and C. Schönenberger, *Snake trajectories in ultraclean graphene p-n junctions,* Nature Communications **6**, 6470 (2015).

[105] A. M. V. D. Zande, R. A. Barton, J. S. Alden, C. S. Ruiz-Vargas, W. S. Whitney, P. H. Q. Pham, J. Park, J. M. Parpia, H. G. Craighead, and P. L. McEuen, *Large-Scale Arrays of Single-Layer Graphene Resonators,* Nano Letters **10**, 4869 (2010).

[106] J. W. Suk, A. Kitt, C. W. Magnuson, Y. Hao, S. Ahmed, J. An, A. K. Swan, B. B. Goldberg, and R. S. Ruoff, *Transfer of CVD-grown monolayer graphene onto arbitrary substrates,* ACS Nano **5**, 6916 (2011).

[107] G. López-Polín, J. Gómez-Herrero, and C. Gómez-Navarro, *Confining crack propagation in defective graphene,* Nano Letters **15**, 2050 (2015).

[108] J. S. Bunch, A. M. van der Zande, S. S. Verbridge, I. W. Frank, D. M. Tanenbaum, J. M. Parpia, H. G. Craighead, and P. L. McEuen, *Electromechanical resonators from graphene sheets,* Science **315**, 490 (2007).

[109] I. W. Frank, D. M. Tanenbaum, A. M. van der Zande, and P. L. McEuen, *Mechanical properties of suspended graphene sheets,* Journal of Vacuum Science & Technology B: Microelectronics and Nanometer Structures **25**, 2558 (2007).

[110] M. Poot and H. S. J. van der Zant, *Nanomechanical properties of few-layer graphene membranes,* Applied Physics Letters **92**, 063111 (2008).

[111] R. A. Barton, B. Ilic, A. M. van der Zande, W. S. Whitney, P. L. McEuen, J. M. Parpia, and H. G. Craighead, *High, size-dependent quality factor in an array of graphene mechanical resonators,* Nano Letters **11**, 1232 (2011).

[112] D. Metten, F. Federspiel, M. Romeo, and S. Berciaud, *All-Optical Blister Test of Suspended Graphene Using Micro-Raman Spectroscopy,* Physical Review Applied **2**, 1 (2014).

[113] Y. Shin, M. Lozada-Hidalgo, J. L. Sambricio, I. V. Grigorieva, A. K. Geim, and C. Casiraghi, *Raman spectroscopy of highly pressurized graphene membranes,* Applied Physics Letters **108**, 221907 (2016).

[114] G.-H. Lee, R. C. Cooper, S. J. An, S. Lee, A. M. van der Zande, N. Petrone, A. G. Hammerberg, C. Lee, B. Crawford, W. Oliver, J. W. Kysar, and J. Hone, *High-strength chemical-vapor-deposited graphene and grain boundaries,* Science **340**, 1073 (2013).

[115] Y. Hwangbo, C.-K. Lee, S.-M. Kim, J.-H. Kim, K.-S. Kim, B. Jang, H.-J. Lee, S.-K. Lee, S.-S. Kim, J.-H. Ahn, and S.-M. Lee, *Fracture characteristics of monolayer CVD-graphene,* Scientific Reports **4**, 4439 (2014).

[116] S. C. O'Hern, C. A. Stewart, M. S. H. Boutilier, J. C. Idrobo, S. Bhaviripudi, S. K. Das, J. Kong, T. Laoui, M. Atieh, and R. Karnik, *Selective molecular transport through intrinsic defects in a single layer of CVD graphene,* ACS Nano **6**, 10130 (2012).

[117] K. Celebi, J. Buchheim, R. M. Wyss, A. Droudian, P. Gasser, I. Shorubalko, J.-I. Kye, C. Lee, and H. G. Park, *Ultimate Permeation Across Atomically Thin Porous Graphene,* Science **344**, 289 (2014).

[118] V. P. Adiga, B. Ilic, R. A. Barton, I. Wilson-Rae, H. G. Craighead, and J. M. Parpia, *Modal dependence of dissipation in silicon nitride drum resonators,* Applied Physics Letters **99**, 253103 (2011).

[119] I. Wilson-Rae, R. A. Barton, S. S. Verbridge, D. R. Southworth, B. Ilic, H. G. Craighead, and J. M. Parpia, *High-Q Nanomechanics via Destructive Interference of Elastic Waves,* Physical Review Letters **106**, 047205 (2011).

[120] H. H. Perez Garza, E. W. Kievit, G. F. Schneider, and U. Staufer, *Controlled, reversible, and nondestructive generation of uniaxial extreme strains (>10%) in graphene,* Nano Letters **14**, 4107 (2014).

[121] S. P. Koenig, L. Wang, J. Pellegrino, and J. S. Bunch, *Selective molecular sieving through porous graphene,* Nature Nanotechnology **7**, 728 (2012).

[122] V. Singh, S. Sengupta, H. S. Solanki, R. Dhall, A. Allain, S. Dhara, P. Pant, and M. M. Deshmukh, *Probing thermal expansion of graphene and modal dispersion at low-temperature using graphene nanoelectromechanical systems resonators,* Nanotechnology **21**, 165204 (2010).

[123] M. K. Zalalutdinov, J. T. Robinson, C. E. Junkermeier, J. C. Culbertson, T. L. Reinecke, R. Stine, P. E. Sheehan, B. H. Houston, and E. S. Snow, *Engineering graphene mechanical systems,* Nano Letters **12**, 4212 (2012).

[124] Q. P. Unterreithmeier, T. Faust, and J. P. Kotthaus, *Damping of Nanomechanical Resonators,* Physical Review Letters **105**, 027205 (2010).

[125] A. Castellanos-Gomez, M. Buscema, R. Molenaar, V. Singh, L. Janssen, H. S. J. van der Zant, and G. A. Steele, *Deterministic transfer of two-dimensional materials by all-dry viscoelastic stamping,* 2D Materials **1**, 011002 (2014).

[126] A. Castellanos-Gomez, E. Navarro-Moratalla, G. Mokry, J. Quereda, E. Pinilla-Cienfuegos, N. Agraït, H. S. J. van der Zant, E. Coronado, G. A. Steele, and G. Rubio-Bollinger, *Fast and reliable identification of atomically thin layers of $TaSe_2$ crystals,* Nano Research **6**, 191 (2013).

[127] A. Castellanos-Gomez, R. van Leeuwen, M. Buscema, H. S. J. van der Zant, G. A. Steele, and W. J. Venstra, *Single-Layer MoS_2 Mechanical Resonators,* Advanced Materials **25**, 6719 (2013).

[128] Z. Yan, C. Jiang, T. R. Pope, C. F. Tsang, J. L. Stickney, P. Goli, J. Renteria, T. T. Salguero, and A. A. Balandin, *Phonon and thermal properties of exfoliated $TaSe_2$ thin films,* Journal of Applied Physics **114**, 204301 (2013).

[129] H. Hummel, R. Fackler, and P. Remmert, *Tantaloxide durch Gasphasenhydrolyse, Druckhydrolyse und Transportreaktion aus 2H-$TaSe_2$: Synthesen von TT-Ta_2O_5 und T-Ta_2O_5 und Kristallstruktur von T-Ta_2O_5,* Chemische Berichte **125**, 551 (1992).

[130] N. Terao, *Structure des oxides de tantale,* Japanese Journal of Applied Physics **6**, 21 (1967).

[131] R. Moser, *Single-crystal growth and polymorphy of Nb_2O_5 and Ta_2O_5,* Schweizerische Mineralogische und Petrographische Mitteilungen **45**, 38 (1965).

[132] P. S. Dobal, R. S. Katiyar, Y. Jiang, R. Guo, and A. S. Bhalla, *Raman scattering study of a phase transition in tantalum pentoxide,* Journal of Raman Spectroscopy **1065**, 1061 (2000).

[133] M. T. Lavik, T. M. Medved, and G. D. Moore, *Oxidation Characteristics of MoS_2 and Other Solid Lubricants,* ASLE Transactions **11**, 44 (1968).

[134] A. Castellanos-Gomez, M. Barkelid, A. M. Goossens, V. E. Calado, H. S. J. van der Zant, and G. A. Steele, *Laser-thinning of MoS_2: on demand generation of a single-layer semiconductor,* Nano Letters **12**, 3187 (2012).

[135] R. S. Devan, W.-D. Ho, C.-H. Chen, H.-W. Shiu, C.-H. Ho, C.-L. Cheng, S. Y. Wu, Y. Liou, and Y.-R. Ma, *High room-temperature photoluminescence of one-dimensional Ta_2O_5 nanorod arrays,* Nanotechnology **20**, 445708 (2009).

[136] R. S. Devan, C.-L. Lin, S.-Y. Gao, C.-L. Cheng, Y. Liou, and Y.-R. Ma, *Enhancement of green-light photoluminescence of Ta_2O_5 nanoblock stacks,* Physical Chemistry Chemical Physics **13**, 13441 (2011).

[137] T. Wah, *Vibration of circular plates,* the Journal of the Acoustical Society of America **34**, 275 (1962).

[138] J. Kang, S. Tongay, J. Zhou, J. Li, and J. Wu, *Band offsets and heterostructures of two-dimensional semiconductors,* Applied Physics Letters **102**, 012111 (2013).

[139] M. Barmatz, *Elastic measurements in one and two-dimensional compounds,* Ultrasonics Symposium Proceedings , 1 (1974).

[140] M. Barmatz, L. R. Testardi, and F. J. D. Salvo, *Elasticity measurements in the layered dichalcogenides $TaSe_2$ and $NbSe_2$,* Physical Review B **12**, 4367 (1975).

[141] C. W. Chu, L. R. Testardi, F. J. D. Salvo, and D. E. Moncton, *Pressure effects on the charge-density-wave phases in 2H-$TaSe_2$,* Physical Review B **14**, 464 (1976).

[142] J. L. Feldman, C. L. Vold, E. F. Skelton, S. C. Yu, and I. L. Spain, *X-ray diffraction studies and thermal and elastic properties of 2H-$TaSe_2$,* Physical Review B **18**, 5820 (1978).

[143] N. A. Abdullaev, *Elastic properties of layered crystals,* Physics of the Solid State **48**, 663 (2006).

[144] S. N. Dub and V. V. Starikov, *Elasticity module and hardness of niobium and tantalum anode oxide films,* Functional Materials **14**, 7 (2007).

[145] C.-L. Tien, C.-C. Lee, K.-P. Chuang, and C.-C. Jaing, *Simultaneous determination of the thermal expansion coefficient and the elastic modulus of Ta_2O_5 thin film using phase shifting interferometry,* Journal of Modern Optics **47**, 1681 (2000).

[146] S. Schmid, K. D. Jensen, K. H. Nielsen, and A. Boisen, *Damping mechanisms in high-Q micro and nanomechanical string resonators,* Physical Review B **84**, 165307 (2011).

[147] P.-L. Yu, T. P. Purdy, and C. A. Regal, *Control of Material Damping in High-Q Membrane Microresonators,* Physical Review Letters **108**, 083603 (2012).

[148] V. P. Adiga, B. Ilic, R. A. Barton, I. Wilson-Rae, H. G. Craighead, and J. M. Parpia, *Approaching intrinsic per-*

formance in ultra-thin silicon nitride drum resonators, Journal of Applied Physics **112**, 064323 (2012).

[149] A. R. Kermany, G. Brawley, N. Mishra, E. Sheridan, W. P. Bowen, and F. Iacopi, *Microresonators with Q-factors over a million from highly stressed epitaxial silicon carbide on silicon,* Applied Physics Letters **104**, 081901 (2014).

[150] S. Lee, V. P. Adiga, R. A. Barton, A. M. van der Zande, G.-H. Lee, B. R. Ilic, A. Gondarenko, J. M. Parpia, H. G. Craighead, and J. Hone, *Graphene metallization of high-stress silicon nitride resonators for electrical integration,* Nano Letters **13**, 4275 (2013).

[151] J. Lee, Z. Wang, K. He, J. Shan, and P. X.-L. Feng, *High frequency MoS_2 nanomechanical resonators,* ACS Nano **7**, 6086 (2013).

[152] E. Coronado, A. Forment-Aliaga, E. Navarro-Moratalla, E. Pinilla-Cienfuegos, and A. Castellanos-Gomez, *Nanofabrication of TaS_2 conducting layers nanopatterned with Ta_2O_5 insulating regions via AFM,* Journal of Materials Chemistry C **1**, 7692 (2013).

[153] S. J. Cartamil-Bueno, P. G. Steeneken, A. Centeno, A. Zurutuza, H. S. J. van der Zant, and S. Houri, *Colorimetry Technique for Scalable Characterization of Suspended Graphene,* Nano Letters **16**, 6792 (2016).

[154] S. J. Cartamil-Bueno, A. Centeno, A. Zurutuza, P. G. Steeneken, H. S. J. van der Zant, and S. Houri, *Very large scale characterization of graphene mechanical devices using a colorimetry technique,* Nanoscale **9**, 7559 (2017).

[155] R. a. Barton, I. R. Storch, V. P. Adiga, R. Sakakibara, B. R. Cipriany, B. Ilic, S. P. Wang, P. Ong, P. L. McEuen, J. M. Parpia, and H. G. Craighead, *Photothermal self-oscillation and laser cooling of graphene optomechanical systems,* Nano Letters **12**, 4681 (2012).

[156] S. Wagner, T. Dieing, A. D. Smith, M. Östling, S. Kataria, and M. C. Lemme, *Noninvasive Scanning Raman Spectroscopy and Tomography for Graphene Membrane Characterization,* Nano Letters **17**, 1504 (2017).

[157] A. Castellanos-gomez, V. Singh, H. S. J. V. D. Zant, and G. a. Steele, *Mechanics of freely-suspended ultrathin layered materials,* Annalen der Physik **527**, 27 (2015).

[158] S. J. Cartamil-Bueno, M. Cavalieri, R. Wang, S. Houri, S. Hofmann, and H. S. J. van der Zant, *Mechanical characterization and cleaning of CVD single-layer h-BN resonators,* npj 2D Materials and Applications **1**, 16 (2017).

[159] ASTM, *ASTM C1161-13 Standard Test Method for Flexural Strength of Advanced Ceramics at Ambient Temperature,* (2013).

[160] D. Lloyd, X. Liu, N. Boddeti, L. Cantley, R. Long, M. L. Dunn, and J. S. Bunch, *Adhesion, stiffness, and instability in atomically thin MoS_2 bubbles,* Nano Letters **17**, 5329 (2017).

[161] I. Jo, M. T. Pettes, J. Kim, K. Watanabe, T. Taniguchi, Z. Yao, and L. Shi, *Thermal conductivity and phonon transport in suspended few-layer hexagonal boron nitride,* Nano Letters **13**, 550 (2013).

[162] H. Zhou, J. Zhu, Z. Liu, Z. Yan, X. Fan, J. Lin, G. Wang, Q. Yan, T. Yu, P. M. Ajayan, and J. M. Tour, *High thermal conductivity of suspended few-layer hexagonal boron nitride sheets,* Nano Research **7**, 1232 (2014).

[163] X. Q. Zheng, J. Lee, and P. X. L. Feng, *Hexagonal boron nitride (h-BN) nanomechanical resonators with temperature-dependent multimode operations,* 2015 Transducers-2015 18th International Conference on Solid-State Sensors, Actuators and Microsystems (TRANSDUCERS) **2**, 1393 (2015).

[164] S. J. Cartamil-Bueno, P. G. Steeneken, F. D. Tichelaar, E. Navarro-Moratalla, W. J. Venstra, R. van Leeuwen, E. Coronado, H. S. J. van der Zant, G. A. Steele, and A. Castellanos-Gomez, *High-quality-factor tantalum oxide nanomechanical resonators by laser oxidation of $TaSe_2$,* Nano Research **8**, 2842 (2015).

[165] S. Caneva, R. S. Weatherup, B. Bayer, B. Brennan, S. J. Spencer, K. Mingard, A. Cabrero-Vilatela, C. Baehtz, A. J. Pollard, and S. Hofmann, *Nucleation Control for Large, Single Crystalline Domains of Monolayer Hexagonal Boron Nitride via Si-Doped Fe Catalysts,* Nano Letters **15**, 1867 (2015).

[166] Q. Cai, D. Scullion, A. Falin, K. Watanabe, T. Taniguchi, Y. Chen, E. J. G. Santos, and L. Li, *Raman Signature and Phonon Dispersion of Atomically Thin Boron Nitride,* Nanoscale **9**, 3059 (2017).

[167] L. Boldrin, F. Scarpa, R. Chowdhury, and S. Adhikari, *Effective mechanical properties of hexagonal boron nitride nanosheets,* Nanotechnology **22**, 505702 (2011).

[168] Z. Lu and M. L. Dunn, *Van der Waals adhesion of graphene membranes,* Journal of Applied Physics **107**, 044301 (2010).

[169] S. M. Kim, A. Hsu, M. H. Park, S. H. Chae, S. J. Yun, J. S. Lee, D.-H. Cho, W. Fang, C. Lee, T. Palacios, M. Dresselhaus, K. K. Kim, Y. H. Lee, and J. Kong, *Synthesis of large-area multilayer hexagonal boron nitride for high material performance,* Nature Communications **6**, 8662 (2015).

[170] R. J. T. Nicholl, H. J. Conley, N. V. Lavrik, I. Vlassiouk, Y. S. Puzyrev, V. P. Sreenivas, S. T. Pantelides, and K. I. Bolotin, *The effect of intrinsic crumpling on the mechanics of free-standing graphene,* Nature Communications **6**, 8789 (2015).

[171] W. Paszkowicz, J. Pelka, M. Knapp, T. Szyszko, and S. Podsiadlo, *Lattice parameters and anisotropic thermal expansion of hexagonal boron nitride in the 10-297.5 K temperature range,* Applied Physics A: Materials Science & Processing **75**, 431 (2002).

[172] D. Yoon, Y. Son, and H. Cheong, *Negative Thermal Expansion Coefficient of Graphene Measured by Raman Spectroscopy,* Nano Letters **11**, 3227 (2011).

[173] N. Morell, A. Reserbat-Plantey, I. Tsioutsios, K. G. Schädler, F. Dubin, F. H. L. Koppens, and A. Bachtold, *High Quality Factor Mechanical Resonators Based on WSe_2 Monolayers,* Nano Letters **16**, 5102 (2016).

[174] Z. Budrikis and S. Zapperi, *Temperature-Dependent Adhesion of Graphene Suspended on a Trench,* Nano Letters **16**, 387 (2016).

[175] A. G. F. Garcia, M. Neumann, F. Amet, J. R. Williams, K. Watanabe, T. Taniguchi, and D. Goldhaber-Gordon, *Effective cleaning of hexagonal boron nitride for graphene devices,* Nano Letters **12**, 4449 (2012).

[176] S. W. King, R. J. Nemanich, and R. F. Davis, *Cleaning of pyrolytic hexagonal boron nitride surfaces,* Surface and Interface Analysis **47**, 798 (2015).

[177] P. Blake, E. W. Hill, A. H. Castro Neto, K. S. Novoselov, D. Jiang, R. Yang, T. J. Booth, and A. K. Geim, *Making graphene visible,* Applied Physics Letters **91**, 063124 (2007).

[178] H. Arjmandi-Tash, A. Allain, Z. V. Han, and V. Bouchiat, *Large scale integration of cvd-graphene based nems with narrow distribution of resonance parameters,* 2D Materials **4**, 025023 (2017).

[179] N. G. Boddeti, S. P. Koenig, R. Long, J. Xiao, J. S. Bunch, and M. L. Dunn, *Mechanics of Adhered, Pressurized Graphene Blisters,* Journal of Applied Mechanics **80**, 40909 (2013).

[180] X. Liu, N. G. Boddeti, M. R. Szpunar, L. Wang, M. a. Rodriguez, R. Long, J. Xiao, M. L. Dunn, and J. S. Bunch, *Observation of pull-in instability in graphene membranes under interfacial forces,* Nano Letters **13**, 2309 (2013).

[181] D. H. Yen and T. Lee, *On the non-linear vibrations of a circular membrane,* International Journal of Non-Linear Mechanics **10**, 47 (1975).

[182] M. Saif, B. E. Alaca, and H. Sehitoglu, *Analytical modeling of electrostatic membrane actuator for micro pumps,* Journal of Microelectromechanical Systems **8**, 335 (1999).

[183] S. P. Koenig, N. G. Boddeti, M. L. Dunn, and J. S. Bunch, *Ultrastrong adhesion of graphene membranes,* Nature Nanotechnology **6**, 543 (2011).

[184] T. Jiang and Y. Zhu, *Measuring graphene adhesion using atomic force microscopy with a microsphere tip,* Nanoscale **7**, 10760 (2015).

[185] D. Akinwande, C. J. Brennan, J. S. Bunch, P. Egberts, J. R. Felts, H. Gao, R. Huang, J.-s. Kim, T. Li, Y. Li, K. M. Liechti, N. Lu, H. S. Park, E. J. Reed, P. Wang, B. I. Yakobson, T. Zhang, Y.-W. Zhang, Y. Zhou, and Y. Zhu, *A Review on Mechanics and Mechanical Properties of 2D Materials - Graphene and Beyond,* Extreme Mechanics Letters **13**, 1 (2016).

[186] X. Gao, X. Yu, B. Li, S. Fan, and C. Li, *Measuring Graphene Adhesion on Silicon Substrate by Single and Dual Nanoparticle-Loaded Blister,* Advanced Materials Interfaces **4**, 1601023 (2017).

[187] E. Paek and G. S. Hwang, *A computational analysis of graphene adhesion on amorphous silica,* Journal of Applied Physics **113**, 164901 (2013).

[188] S. Kumar, D. Parks, and K. Kamrin, *Mechanistic Origin of the Ultrastrong Adhesion between Graphene and a-SiO_2: Beyond van der Waals,* ACS Nano **10**, 6552 (2016).

[189] H. Jessop, *On cornu's method of determining the elastic constants of glass,* Philosophical Magazine Series 6 **42**, 551 (1921).

[190] A. Reserbat-Plantey, L. Marty, O. Arcizet, N. Bendiab, and V. Bouchiat, *A local optical probe for measuring motion and stress in a nanoelectromechanical system,* Nature Nanotechnology **7**, 151 (2012).

[191] E. Ochoa-Martínez, M. Gabás, L. Barrutia, A. Pesquera, A. Centeno, S. Palanco, A. Zurutuza, and C. Algora, *Determination of a refractive index and an extinction coefficient of standard production of CVD-graphene,* Nanoscale **7**, 1491 (2015).

[192] T. Georgiou, L. Britnell, P. Blake, R. V. Gorbachev, A. Gholinia, A. K. Geim, C. Casiraghi, and K. S. Novoselov, *Graphene bubbles with controllable curvature,* Applied Physics Letters **99**, 2011 (2011).

[193] D. Renshaw, G. Wang, P. B. Denyer, and M. Lu, *CMOS video cameras,* Euro ASIC '91 (1991).

[194] W. C. Young and R. G. Budynas, *Roark's Formulas for Stress and Strain,* Vol. 7th Edition, McGraw-Hill (2002).

[195] A. International, *Standard Test Method for Determining Gas Permeability Characteristics of Plastic Film and Sheeting,* ASTM International **Designation D1434-82**, 1 (2015).

[196] M. AbdelGhany, F. Mahvash, M. Mukhopadhyay, A. Favron, R. Martel, M. Siaj, and T. Szkopek, *Suspended graphene variable capacitor,* 2D Materials **3**, 041005 (2016).

[197] H. Rokni and W. Lu, *Effect of graphene layers on static pull-in behavior of bilayer graphene/substrate electrostatic microactuators,* Journal of Microelectromechanical Systems **22**, 553 (2013).

[198] M. AbdelGhany, E. Ledwosinska, and T. Szkopek, *Theory of the suspended graphene varactor,* Applied Physics Letters **101**, 153102 (2012).

[199] Z. Li, L. Zhao, Z. Ye, H. Wang, Y. Zhao, and Z. Jiang, *Resonant frequency analysis on an electrostatically actuated microplate under uniform hydrostatic pressure,* Journal of Physics D: Applied Physics **46**, 195108 (2013).

[200] Z. Sun, A. Martinez, and F. Wang, *Optical modulators with 2D layered materials,* Nature Photonics **10**, 227 (2016).

[201] F. Bonaccorso, Z. Sun, T. Hasan, and A. Ferrari, *Graphene photonics and optoelectronics,* Nature Photonics **4**, 611 (2010).

[202] E. K. Chan, T. Chang, T.-C. Fung, J. Hong, C. Kim, J. Ma, Y. Pan, S.-G. Wang, and B. Wen, *Continuous color reflective display fabricated in integrated MEMS-and-TFT-on-glass process,* Journal of Microelectromechanical Systems **26**, 143 (2017).

[203] A. Reserbat-Plantey, K. G. Schädler, L. Gaudreau, G. Navickaite, J. Güttinger, D. Chang, C. Toninelli, A. Bachtold, and F. H. Koppens, *Electromechanical control of nitrogen-vacancy defect emission using graphene nems,* Nature Communications **7**, 10218.

[204] J. Davis, Y.-H. Hsieh, and H.-C. Lee, *Humans perceive flicker artifacts at 500 Hz,* Scientific Reports **5**, 7861 (2015).

[205] S. Westland, C. Ripamonti, and V. Cheung, *Computational colour science using MATLAB,* John Wiley & Sons (2012).

[206] L. Wang, L. W. Drahushuk, L. Cantley, S. P. Koenig, X. Liu, J. Pellegrino, M. S. Strano, and J. S. Bunch, *Molecular valves for controlling gas phase transport made from discrete ångström-sized pores in graphene,* Nature Nanotechnology **10**, 785 (2015).

[207] B. B. Mandelbrot, *Fractals,* Wiley Online Library (1977).

[208] B. B. Mandelbrot and R. Pignoni, *The fractal geometry of nature,* WH freeman New York (1983).

[209] B. Burlando, *The fractal geometry of evolution,* Journal of Theoretical Biology **163**, 161 (1993).

[210] G. B. West, J. H. Brown, and B. J. Enquist, *The fourth dimension of life: fractal geometry and allometric scaling of organisms,* Science **284**, 1677 (1999).

[211] T. F. Nonnenmacher, G. A. Losa, and E. R. Weibel, *Fractals in biology and medicine,* Birkhäuser (2013).

[212] D. Garcia-Sanchez, A. M. van der Zande, A. S. Paulo, B. Lassagne, P. L. McEuen, and A. Bachtold, *Imaging mechanical vibrations in suspended graphene sheets,* Nano Letters **8**, 1399 (2008).

[213] W. Bao, F. Miao, Z. Chen, H. Zhang, W. Jang, C. Dames, and C. N. Lau, *Controlled ripple texturing of suspended graphene and ultrathin graphite membranes,* Nature Nanotechnology **4**, 562 (2009).

[214] J. Güttinger, A. Noury, P. Weber, A. M. Eriksson, C. Lagoin, J. Moser, C. Eichler, A. Wallraff, A. Isacsson, and A. Bachtold, *Energy-dependent path of dissipation in nanomechanical resonators,* Nature Nanotechnology **12**, 631 (2017).

[215] J. Earls, *The character of inca and andean agriculture,* Departamento de Ciencias Sociales, Pontificia Universidad Catolica del Peru (1998).

[216] K. R. Wright, R. M. Wright, Z. Valencia, and G. F. McEwan, *Moray: Inca engineering mystery,* American Society of Civil Engineers (ASCE) (2010).

[217] *https://breakthroughinitiatives.org/Concept/3,* (2016).

[218] R. Landel, W. Layman, E. Marsh, R. Ploszaj, and W. Rowe, *Solar sailing-the concept made realistic,* 16th Aerospace Sciences Meeting (1978).

[219] T. C. Tsu, *Interplanetary travel by solar sail,* Ars Journal **29**, 422 (1959).

[220] L. Johnson, M. Whorton, A. Heaton, R. Pinson, G. Laue, and C. Adams, *Nanosail-d: A solar sail demonstration mission,* Acta Astronautica **68**, 571 (2011).

[221] Y. Tsuda, O. Mori, R. Funase, H. Sawada, T. Yamamoto, T. Saiki, T. Endo, and J. Kawaguchi, *Flight status of IKAROS deep space solar sail demonstrator,* Acta Astronautica **69**, 833 (2011).

[222] *space.skyrocket.de,* (2017).

[223] J. M. Fernandez, L. Visagie, M. Schenk, O. R. Stohlman, G. S. Aglietti, V. J. Lappas, and S. Erb, *Design and development of a gossamer sail system for deorbiting in low earth orbit,* Acta Astronautica **103**, 204 (2014).

[224] T. Hoang, A. Lazarian, B. Burkhart, and A. Loeb, *The interaction of relativistic spacecrafts with the interstellar medium,* The Astrophysical Journal **837**, 5 (2017).

[225] R. R. Nair, P. Blake, A. N. Grigorenko, K. S. Novoselov, T. J. Booth, T. Stauber, N. M. R. Peres, and A. K. Geim, *Fine structure constant defines visual transparency of graphene,* Science **320**, 1308 (2008).

[226] T. Zhang, H. Chang, Y. Wu, P. Xiao, N. Yi, Y. Lu, Y. Ma, Y. Huang, K. Zhao, X.-Q. Yan, Z.-B. Liu, J.-G. Tian, and Y. Chen, *Macroscopic and direct light propulsion of bulk graphene material,* Nature Photonics **9**, 471 (2015).

[227] K. F. Mak, C. H. Lui, J. Shan, and T. F. Heinz, *Observation of an electric-field-induced band gap in bilayer graphene by infrared spectroscopy,* Physical Review Letters **102**, 256405 (2009).

CURRICULUM VITÆ

Santiago José CARTAMIL BUENO

15-10-1986 Born in Melilla, Spain.

EDUCATION

1999–2004 High School (with honors)
I.E.S. Generalife (Granada, Spain)

2004–2010 'Licenciatura' degree in Physics (B.Sc. + M.Sc.)
Universidad de Granada (Granada, Spain). ERASMUS exchange at Niels Bohr Institute (Københavns Universitet) (2007–2008)

2009–2013 'Ingeniero' degree in Electronics (B.Eng. + M.Eng.)
Universidad de Granada (Granada, Spain). Education Abroad Program exchange at University of California, San Diego (2009–2010)
Thesis: Simulations on hydrogenated-edge armchair graphene nanoribbons: I-V characteristics under uniaxial strain
Promotor: Prof. dr. S. Rodríguez-Bolívar

2011–2012 M.Sc. in Nanotechnology and Materials Science
Universitat Autònoma de Barcelona (Barcelona, Spain)
Thesis: Graphene resonators with high quality factor using a substrate independent transfer technique
Promotor: Prof. dr. A. Bachtold

2013 Research internship
Adolphe Merkle Institute (Fribourg, Switzerland)

2013–2017 Ph.D. in Applied Physics. Graphene Flagship mobility grant for research visit at Boston University (2017)
Delft University of Technology (Delft, The Netherlands)
Thesis: Freestanding 2D Materials and Their Applications: From Lab to Fab
Promotors: Prof. dr. P. G. Steeneken & Prof. dr. ir. H. S. J. van der Zant

AWARDS

2004	Entrance with honors to Universidad de Granada (Spain)
2007	ERASMUS scholarship at Niels Bohr Institute from Københavns Universitet (Denmark)
2009	Education Abroad Program exchange at University of California, San Diego (USA)
2011	"la Caixa" Foundation scholarship for postgraduate studies at Universitat Autònoma de Barcelona (Spain)
2016	Proposal winner for European Space Agency's (ESA) Drop Your Thesis! Programme 2017 (Graphene-based spacecraft sail for light-induced propulsion)
2017	Graphene Flagship Mobility grantee for stay at Boston University (USA)

LIST OF PUBLICATIONS

12. **S.J. Cartamil-Bueno**, A. Centeno, S. Houri, A. Zurutuza, and P.G. Steeneken. *Laser-induced tensioning of CVD double-layer graphene drumhead resonators* (tentative), in preparation (2018).

11. **S.J. Cartamil-Bueno**, D. Davidovikj, A. Centeno, A. Zurutuza, H.S.J. van der Zant, P.G. Steeneken, S. Houri. *Graphene Interferometry MOdulation Display (GIMOD) mechanical pixels studied with a stroboscopic technique* (tentative), in preparation (2018).

10. R.J. Dolleman, S. Houri, D. Davidovikj, **S.J. Cartamil-Bueno**, Y.M. Blanter, H.S.J. van der Zant, and P.G. Steeneken. *Optomechanics for thermal characterization of suspended graphene*, Physical Review B **96**, 165421 (2017).

9. D. Davidovikj, F. Alijani, **S.J. Cartamil-Bueno**, H.S.J. van der Zant, M. Amabili, and P.G. Steeneken. *Nonlinear dynamic characterization of two-dimensional materials*, Nature Communications **8**, 1253 (2017).

8. **S.J. Cartamil-Bueno**, M. Cavalieri, R. Hwang, S. Houri, S. Hofmann, and H.S.J. van der Zant. *Mechanical characterization and cleaning of CVD single-layer h-BN resonators*, npj 2D Materials and Applications **1**, 16 (2017).

7. **S.J. Cartamil-Bueno**, A. Centeno, A. Zurutuza, P.G. Steeneken, H.S.J. van der Zant, and S. Houri. *Very large scale characterization of graphene mechanical devices using a colorimetry technique*, Nanoscale **9**, 7559 (2017).

6. S. Houri, **S.J. Cartamil-Bueno**, M. Poot, P.G. Steeneken, H.S.J. van der Zant, and W.J. Venstra. *Direct and parametric synchronization of a graphene self-oscillator*, Applied Physics Letters **110**, 073103 (2017).

5. R.J. Dolleman, **S.J. Cartamil-Bueno**, H.S.J. van der Zant, and P.G. Steeneken. *Graphene gas osmometers*, 2D Materials **4**, 011002 (2016).

4. **S.J. Cartamil-Bueno**, P.G. Steeneken, A. Centeno, A. Zurutuza, H.S.J. van der Zant, and S. Houri. *Colorimetry technique for scalable characterization of suspended graphene*, Nano Letters **16**, 6792 (2016).

   D. Davidovikj, J.J. Slim, **S.J. Cartamil-Bueno**, H.S.J. van der Zant, P.G. Steeneken, and W.J. Venstra. *Visualizing the Motion of Graphene Nanodrums*, Nano Letters **16**, 2768 (2016).

3. R.J. Dolleman, D. Davidovikj, **S.J. Cartamil-Bueno**, H.S.J. van der Zant, P.G. and Steeneken. *Graphene squeeze-film pressure sensors*, Nano Letters **16**, 568 (2016).

2. **S.J. Cartamil-Bueno**, P.G. Steeneken, F.D. Tichelaar, E. Navarro-Moratalla, W.J. Venstra, R. van Leeuwen, E. Coronado, H.S.J. van der Zant, G.A. Steele, A. Castellanos-Gomez. *High-quality-factor tantalum oxide nanomechanical resonators by laser oxidation of $TaSe_2$*, Nano Research **8**, 2842 (2015).

1. **S.J. Cartamil-Bueno** and S. Rodríguez-Bolívar. *IV characteristics of in-plane and out-of-plane strained edge-hydrogenated armchair graphene nanoribbons*, Journal of Applied Physics **117**, 244504 (2015).